Quasi-static motion of a liquid droplet on a deformable substrate

Chung-Hao Wang

December, 2023

School of Mathematics

A thesis submitted for the degree of
Doctor of Philosophy

Abstract

We investigate the dynamics of a three-dimensional droplet sitting on a time-dependent solid substrate. The study focuses on droplet motion caused by slow deformations of the substrate, where inertial effects are negligible, and the shape of the droplet at each time instant is governed by the balance of the gravity and capillary forces. Four models of the contact line dynamics are considered in the present study.

A quasi-static approximation is employed to analyse this dynamic problem. Our approach to solving the quasi-static problem involves using asymptotic methods by considering a small perturbation to the elevation of the solid substrate. Initially, the solid substrate is flat and horizontal, and the droplet is axisymmetric and at rest. The first-order correction of the droplet shape, induced by slow motions of the substrate, depends on the specific contact line model applied.

In the first model, the contact line remains fixed during the dynamic process. Apart from determining the droplet shape, the current local contact angle needs to be calculated. By contrast, in the second model, the contact line is free to move, and the current local contact angle along the moving contact line is assumed to be equal to the equilibrium contact angle. The first-order corrections of both the position of the contact line and the droplet shape are determined simultaneously.

The third model combines the previous two models. Depending on the current local contact angle, the different parts of the contact line have different characteristics, termed pinned and unpinned regions. Lastly, the fourth model of contact line motion is known as the Cox-Voinov model, in which the contact line is always moving in the direction of its normal.

Contents

List of Figures

Acknowledgements

First of all, I would like to express my deepest appreciation to my supervisor, Professor Alexander Korobkin, for his exceptional guidance and invaluable advice during my Ph.D. studies. Without your support, I would not have successfully completed this research. Beyond providing professional supervision, you consistently offered encouragement and assistance whenever I encountered difficulties. I am proud to have had the opportunity to learn from you over the years.

I am extremely grateful to Dr. Davide Proment and Dr. Madeleine Moore for serving on my thesis committee. I also extend my thanks to the University of East Anglia for providing an amazing academic environment. I particularly appreciate the practical suggestions provided by Professor Emilian Parau, Dr. Alberto Alberello, and Daniel Netherwood, who have greatly contributed to my professional development. I am very thankful to all my friends in the PGR office for their encouragement and support during the stressful graduate study, especially Connor, Alice, Dan, Anna, and Tommy. Additionally, I would like to acknowledge the support of Dr. Mark Cooker and Dr. Islam Foniqi, whose assistance has enriched my experience in the UK.

I wish to express my sincere gratitude to my mother, father, sister, and brother for their unconditional support and accompaniment during my graduate studies. In addition, I extend my appreciation to all research funding institutions that have provided financial support, directly or indirectly, for my graduate studies.

Thank you all for your guidance, assistance, and support in shaping the person I am today.

1

Introduction

1.1 Background

As a liquid is deposited on a solid surface, two general scenarios exist. In the first situation, the liquid spreads entirely over the surface, as observed when silicone oil is placed on a horizontal surface (Tanner, 1979). In contrast, in the second case, a drop forms a spherical cap for a small volume instead of spreading out. This behaviour, such as a water droplet on a silicon wafer, is referred to as the sessile drop.

The contact angle, θ_c, of the sessile drop is defined as an angle between the tangent planes to the air/liquid and liquid/solid interfaces at the contact line. Considering the surface of the solid substrate to be flat, rigid, perfectly smooth, and chemically homogeneous, a unique angle is formed for this specific vapour, liquid, and solid system at equilibrium, depicted in Figure 1.1.1. This angle is called the static or **equilibrium contact angle**, denoted as θ_e. Young (1805) considered the mechanical force balance on the three-phase line to determine the equilibrium contact angle,

$$\gamma \cos\theta_e = \gamma_{SG} - \gamma_{SL}. \tag{1.1.1}$$

Here γ, γ_{SG}, and γ_{SL} represent the surface tension at the liquid/gas, solid/gas, and solid/liquid interfaces, respectively. The contact angle can be used to quantify the wettability of a solid surface by a liquid. A substrate is called hydrophilic if the contact angle is less than 90°; otherwise, it is called hydrophobic.

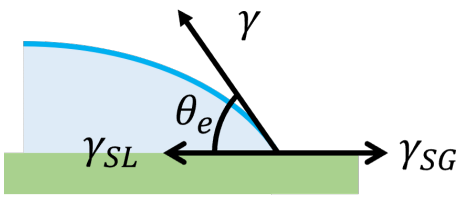

Figure 1.1.1: A droplet on a flat surface at equilibrium.

The dynamics of sessile drops play a crucial role in various industrial processes and attract scientific interest. As a testament to its importance, the number of publications on droplets has increased tenfold in the last 50 years (Brutin and Starov, 2018). These droplets find applications in a wide range of areas, including drop manipulation in microfluidics (Daniel et al., 2005), inkjet printing (Wijshoff, 2018), mixing of fluids (Whitehill et al., 2012), spray painting (Zabihi and Eslamian, 2015), surface treatment and many others.

There are various methods to induce motion in drops on a solid surface. Technologies for transporting drops include establishing wettability gradients (Daniel et al., 2004) or thermodynamic gradients (Mettu and Chaudhury, 2008). The successful demonstration of drop motion has been achieved on ratchet topological structures (Buguin et al., 2002) or textured surfaces (Duncombe et al., 2012). Brunet et al. (2007) employed an experimental approach to investigate the dynamic behaviour of a droplet placed on a vibrating inclined plate. Their research revealed a climbing phenomenon instead of sliding down due to gravity, which occurs when the vibration acceleration surpasses a certain threshold.

Tsai et al. (2015) explored the dynamic behaviours of a sessile drop on a vibrating elastic plate, where the vibration amplitude was different in different parts of the plate. The study involved a comparison between theoretical shapes and frequencies of the resonant mode with those observed in experiments, providing insights into different regimes of droplet oscillations. The circular patterns of the elastic plate oscillations, called Chladni figures, were visualised using small solid particles. The resulting nodal lines in the plate, corresponding to the external forcing frequency, were accurately predicted by the theoretical model. A droplet placed at a nodal line oscillated due to the pitch motion of the plate at this line but not due to the plate vertical vibration, which is negligible in experiments at the nodal line. In contrast, a droplet located away from the nodal lines displayed distinct behaviour, leading to potential depinning of the contact line due to the plate deflection.

Our objective is to investigate the motion of a sessile drop induced by time-dependent deformations of a solid substrate. Given slow deformations of the substrate, the quasi-static approximation is employed to analyse the dynamic behaviour of the droplet. To benefit the modelling of this problem, we conduct a literature review on (1) the droplet shape on a flat solid surface, (2) the droplet on an inclined plane, and (3) the dynamic contact line models.

The research on the droplet shape on a flat solid surface is typically associated with static behaviour. In this situation, the contact angle along the contact line remains constant, and the shape of the droplet can be reasonably regarded as axisymmetric. In contrast, investigations of the droplet on an incline, where the contact angles on the uphill and downhill sides differ, represent a shift from static

to dynamic behaviour. To gain a better understanding of drop motion caused by the deformation of the solid plate, it is necessary to have models of the contact line that relate the speed of the contact line to the variable contact angle. Section 1.3 offers an overview of the content within each chapter of this thesis.

1.2 Literature review

1.2.1 Droplet shape on a flat surface

Generally, when a droplet is placed on a flat solid surface, the contact angle is regarded as the equilibrium contact angle, see equation (1.1.1). Many mathematical models exist to determine the droplet shape on the flat solid surface. The simplest one is to adopt the shape of a spherical cap (Polyanin and Manzhirov, 2006). Once the height of the apex and the width of the base are known, determining the shape of the droplet is straightforward. This model is applicable when the droplet size is small enough that the influence of gravity can be neglected. Extrand (2006) investigated the relationship between wettability and contact area by considering a small droplet. The result can be applied to two-phase flow in small channels like fuel cells.

The second model, the most famous one, is based on the **Young-Laplace equation** (Young, 1805) (Laplace, 1806). This equation relates the pressure jump across the interface to its principal radii of curvature,

$$\Delta p = \gamma \left(\frac{1}{R_1} + \frac{1}{R_2} \right), \tag{1.2.1}$$

where Δp is the pressure difference, γ is the surface tension coefficient, and R_1 and R_2 are principal curvature radii. There is no analytical solution for the Young-Laplace equation. The earliest significant progress in this field was made by Bashforth and Adams (1883). They generated tables of the sessile drop shapes for various surface tensions using numerical iteration methods without the aid of modern computers. Fordham (1948) extended their work and calculated the tables for the pendant drop. Hartland and Hartley (1976) first utilised a computer program to solve the Young-Laplace equation numerically, employing a fourth-order Runge-Kutta method.

O'Brien and van den Brule (1991) employed the perturbation method by considering the small droplet to find the shape of an axisymmetric sessile drop. This solution enables the easy estimation of the contact angle through the maximum radius and height of the droplet. Allen (2003) simplified the Young-Laplace equation by considering the small slope of the droplet shape. The resulting approximated solution eliminates the need for numerical integration and is valid for any size but a small contact angle.

The solid surface is considered smooth and homogeneous in Young's model (1.1.1), so the contact angle models need to be adjusted when accounting for surface roughness and heterogeneity. Wenzel (1936) used the roughness factor, which is the ratio of the actual surface area to the projected planar surface area, to illustrate how the contact angle changes when it comes into contact with a rough or textured solid surface. In contrast, Cassie and Baxter (1944) introduced the idea that air can become trapped at the contact area between the droplet and the surface, which characterises wetting and non-wetting states. This model is particularly relevant when dealing with heterogeneous substrates.

Apart from calculating the Young-Laplace equation to determine the droplet shape, another common approach is applying the energy minimisation method by considering the gravitational and surface energies in an Euler-Lagrange framework. The shapes of droplets on rough and flat (Chen et al., 2005) or the heterogeneous and flat (Brandon et al., 1997) surfaces were investigated using numerical simulations, which minimises the free energy of the system by the software Surface Evolver. Bormashenko (2009) explored various contact angle models for a droplet positioned on a curved solid surface through variational analysis. The findings reveal that the classic contact angle models, Young's, Wenzel's and Cassie's models, are still applied to curved surfaces. Ye and Mizutani (2023) employed the same analysis but focused on structured surfaces, specifically those featuring concentric and parallel V-shaped grooves.

1.2.2 Droplet shape on an inclined plate

Consider a sessile droplet initially placed on a flat horizontal solid plate. Then this solid plate is inclined slowly. The droplet may stay at rest or slide down. The front case has been depicted in Figure 1.2.1. The tilted angle of the plate is denoted by α. The contact angle at the uphill and the downhill have different values.

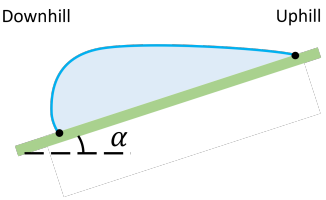

Figure 1.2.1: A droplet stays on an incline with the tilted angle α.

Berejnov and Thorne (2007) employed an experimental approach to investigate the influence of the tilted angle on the phenomena of staying and sliding on a solid surface. Their study identified three distinct thresholds of the tilted angle corresponding to transitional events of the unpinning contact line. Initially, as the substrate is tilted at a small inclined angle, the contact line

remains pinned in its original circular configuration. Beyond the first critical tilt angle, the portion of the contact line on the downhill becomes locally unstable, leading to a displacement and establishing a new equilibrium configuration, referred to as the advancing behaviour. A similar incident occurs beyond a second, larger critical tilted angle but on the uphill side, resulting in the receding behaviour. However, beyond a third critical angle of inclination, the whole contact line is unstable, and the droplet slides continuously. A similar experimental observation was mentioned by Chou et al. (2012), but in their case, the advancing and receding transitions might coincide simultaneously.

As a droplet is on the inclined plate, the contact angle on the downhill side reaches its maximum value before part of the contact line slips, known as the **advancing contact angle**, θ_a. Conversely, the contact line starts to recede, where the contact angle at this point is the **receding contact angle**, θ_r. From the experimental observation, the static contact angle can be of any value between the advancing and receding contact angles, depending on how the droplet is initially placed. The difference between these two contact angles, $\theta_a - \theta_r$, is termed the **contact angle hysteresis** (Butt et al., 2022).

For a sessile drop on a tilted plate, a retention force at the three-phase line is required to balance gravity. This retention force of the pinning droplet on an inclined plate was formulated by Macdougall and Ockrent (1942),

$$F = k\gamma w(\cos\theta_r - \cos\theta_a). \tag{1.2.2}$$

Here, k is an empirical constant dependent on the shape of the contact line, γ is the surface tension at the liquid/gas interface, and $2w$ is the width of the elliptical contact line. Note that for the circular contact line, w can be replaced by the radius of the contact line (Extrand and Kumagai, 1995). de la Madrid et al. (2019) pointed out that the constant k depends on not only the geometry of the contact line but also the types of the droplet, like the sessile drop or pendant drop. If gravity cannot overcome this retention force, the droplet should stay on the inclined plate, and the contact angle along the contact line falls into the interval $[\theta_r, \theta_a]$.

Many studies employ numerical simulations to determine the droplet shape on an inclined plate by minimising the free energy in the system. However, no shape of a droplet on the inclined plate can achieve equilibrium in terms of the system's potential energy since it decreases when the droplet shifts down on the surface. Santos and White (2011) proposed a model where the contact line is stationary for contact angles within the range of the advancing and the receding angles, and moves in order to prevent angles outside this range. The variational problem was solved using the Surface Evolver software. Following a similar approach, Prabhala et al. (2013) developed a routine in Surface Evolver

to explore contact angle hysteresis, focusing specifically on the retention force on the contact line. Building upon this, Janardan and Panchagnula (2014) utilised Surface Evolver to simulate the nonsymmetrical droplet shape on the inclined plate and investigated the effect of the tilted angle. The simulation result is in agreement with the experimental findings. Apart from the contact line hysteresis, Musterd et al. (2014) also incorporated the effect from the initial shape into the contact line model, which agrees with the experimental results from Ruiz-Cabello et al. (2011).

In numerous theoretical investigations related to droplets on inclined surfaces, a common approach involves determining the droplet shape by balancing the pressure terms, utilising Young's Laplace equation with an extra forcing term. De Coninck et al. (2017) employed the asymptotic method by considering a small tilted angle ($\alpha \ll 1$) with a stationary circular configuration of the contact line. They compared the asymptotic solution of the first-order correction to the numerical simulation from Surface Evolver, achieving good agreement for small Bond numbers. However, the circular contact line assumption contradicted the experimental observation (Berejnov and Thorne, 2007). To approximate the droplet shape with an elliptical contact line, ElSherbini and Jacobi (2004) employed two circles sharing a common tangent at the maximum height. Ravazzoli et al. (2019) analysed the droplet shape using the shallow water approximation, expressing the analytical series solution of the droplet shape in terms of a combination of modified Bessel functions of the first kind and trigonometric functions. The obtained theoretical results were consistent with experimental observations.

1.2.3 Dynamic contact line

Traditionally, the flow model is computed using the Navier-Stokes equation with a no-slip condition. However, when it comes to modelling the moving contact line, challenges related to stress singularities emerge. To address these challenges, several models have been proposed to describe the conditions near the contact line (Bonn et al., 2009).

Based on the experimental observation, relationships between the local contact angle θ_c and the velocity of the contact line, U, are used to model the contact line dynamics. In a simplified model, the local contact angle depends on the magnitude of U and its direction. Such a model may explain the hysteresis effect as well, as sketched in Figure 1.2.2. The upper point on the solid line there, where $U = 0$, is the advancing contact angle, while the bottom one is the receding contact angle, and a jump between these two points represents hysteresis. When $U > 0$, the droplet advances, while $U < 0$ indicates the

droplet is receding. This phenomenon can be described by a set of inequalities,

$$\begin{cases} U > 0, & \theta_c > \theta_a, \\ U = 0, & \theta_a > \theta_c > \theta_r, \\ U < 0, & \theta_c < \theta_r. \end{cases} \tag{1.2.3}$$

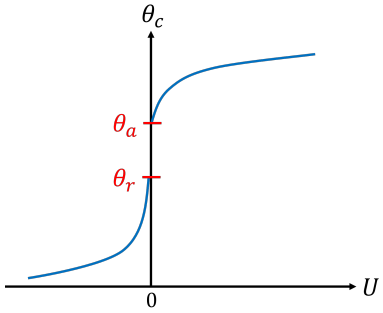

Figure 1.2.2: A sketch of the relationship between the local contact angle θ_c and velocity of the contact line U.

There are two main physical approaches to modelling the dynamics of the contact line, as Figure 1.2.3 shows. The first one, known as the hydrodynamic theory, focuses on dissipation caused by viscous flow near the moving contact line. In this hydrodynamic model, three relevant length scales are introduced: macroscopic, mesoscopic, and microscopic. The local contact angle is related to the macroscopic scale, while the bending of the liquid-gas interface due to viscosity within a mesoscopic region contributes to changes in the local contact angle. The microscopic contact angle, denoted as θ_m, is assumed to be governed by intermolecular forces and retains its static value. Various models have been proposed to establish relationships between dynamic contact angle θ_c and the dimensionless velocity called the capillary number,

$$Ca = \mu U/\gamma \left(\frac{\text{viscous drag force}}{\text{surface tension}} \right), \tag{1.2.4}$$

where μ is the dynamic viscosity of the liquid, γ is the surface tension at the air-liquid interface, and U is the velocity of the contact line. These models typically rely on several key assumptions: (1) the solid surface is assumed to be perfectly smooth, (2) inertial effects are considered negligible, (3) the capillary number is small.

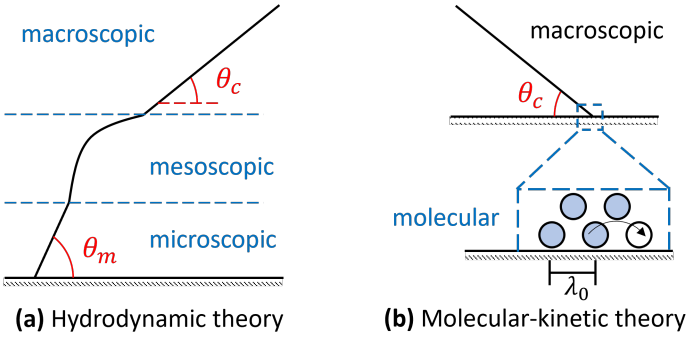

Figure 1.2.3: Schematic figures of the contact line models: (a) hydrodynamic theory (b) molecular-kinetic theory.

By employing lubrication theory (Hamrock et al., 2004), the flow near the contact line at the leading order is governed by a delicate balance between viscous and capillary forces. The seminal work by Voinov (1976) provided insights into the behaviour of the solution. Cox (1986) applied the method of matched asymptotic expansions to reproduce the Voinov relation,

$$\theta_c^3 = \theta_m^3 + 9Ca\ln(L_M/L_m), \qquad \theta_m = \theta_e, \tag{1.2.5}$$

where L_m is a microscopic length scale, and L_M is the distance to the wall where the model is applied. Equation (1.2.5) is commonly referred to as the **Cox-Voinov equation**. Blake (2006) pointed out that the logarithmic term in equation (1.2.5) suggests that the dynamic contact angle θ_c depends on macroscopic-scale geometry. However, this term is often regarded as an adjustable parameter in practice. The estimates place the value of this logarithmic term on the order of 10. Nevertheless, experimental results for non-wetting liquids have shown various values (Petrov et al., 2003). These larger values are typically considered physically unrealistic, as they would seemingly necessitate sub-molecular microscopic length scales, but the hydrodynamic model is mostly satisfactory in a small contact line velocity regime ($Ca \ll 1$).

The second approach to the contact line dynamic is often called the molecular-kinetic theory. It focuses on the vicinity of the moving contact line, where fluid particles (molecules) may attach to or detach from the solid surface. In this model, the microscopic contact angle depends on velocity and is identical to the experimentally observed angle. Thus, there are two length scales: the molecular scale, where dissipation occurs, and the macroscopic scale.

In contrast to the hydrodynamic model, molecular-kinetic theory neglects viscous dissipation and incorporates solid-surface characteristics. Two key parameters come into play: the molecular oscillation frequency, denoted as K_0, and the average distance of each activated jump, λ_0. Within the

molecular-kinetic theory, the motion of the contact line is determined by the statistical dynamics of the molecules within a three-phase line. The driving force for the contact line to move is given by $\gamma(\cos\theta_e - \cos\theta_c)$. The resulting equation for the wetting line velocity is described by

$$U = 2K_0\lambda \sinh\left(\frac{\gamma\lambda_0^2}{2k_BT}(\cos\theta_e - \cos\theta_c)\right), \tag{1.2.6}$$

where k_B is the Boltzmann constant and T is the absolute temperature.

1.3 Thesis outline

The aim of this thesis is to investigate the dynamics of a three-dimensional droplet placed on a time-dependent solid substrate. The solid surface is assumed to be smooth and homogeneous. The flow inside the droplet is considered inviscid, incompressible and irrotational. The droplet volume is assumed to be constant since we do not consider the secondary droplet generated or the droplet evaporation and condensation effect. The shape of the droplet and the contact line are unknown in advance, so essentially, we are working on a free boundary value problem. We explore four distinct models of contact line dynamics in this study.

In this thesis, we employ the quasi-static approximation to analyse this dynamic problem, wherein the flow inside the droplet is neglected in the leading order (see section 2.5, where this approximation is justified), and the droplet shape at each instant is balanced by gravity and capillary forces. The governing equation is the Young-Laplace equation (Young, 1805). Our approach to solving this problem employs asymptotic methods by considering a small perturbation to the elevation of the solid substrate. We consider slow deformations of the solid substrate starting from its flat horizontal position at the initial instant. Before the substrate starts deforming, the droplet is at rest and is of an axisymmetric shape. The first correction to the initial droplet shape caused by the slow motion of the substrate depends on which contact line model is applied.

In chapter 2, section 2.1 provides the mathematical formulation of our problem. To facilitate a better understanding, fundamental quantities are defined, which are later used to describe the dynamics of the droplet. Section 2.2 introduces the contact angle in the three-dimensional space, and section 2.3 deals with the normal velocity of the contact line. The axisymmetric initial droplet shape is calculated in section 2.4. In this problem, the radius of the contact line is unknown in advance and should be determined together with the droplet shape. The contact angle for the initial shape is equal to the equilibrium contact angle. The initial axisymmetric shape of the droplet and

the radius of its contact line provide the initial conditions for all contact line models under consideration. In section 2.5, we obtain the conditions under which the quasi-static approximation is valid.

In chapter 3, we study the pinned contact line, where the contact line does not move with respect to the moving substrate. In this model, the position of the contact line is provided from the initial condition, which is simplified to a boundary value problem. The free surface of the droplet and the current local contact angle along the contact line are determined in the first-order correction.

Unlike the pinned contact line model, the contact line is allowed to move in chapter 4. For this unpinned model, we assume the current local contact angle at each point along the contact line is equal to the equilibrium contact angle. The contact line could be different from its initial circular shape. To handle this issue, we introduce the stretched coordinates to incorporate the contact line into our formulation. In this model, we are solving a free boundary value problem as both the droplet shape and the position of the contact line should be determined.

In chapter 5, we consider the part of the contact line to be free to move, but the rest is pinned. In other words, the contact line is split into pinned and unpinned regions. Within the pinned region, the current local contact angle falls into the interval of the advancing and receding contact angles, and this part of the contact line is stationary. The contact line in the unpinned region moves forward or backward in its normal direction, but we assume that the current local contact angle is equal to either the advancing or receding contact angle. The interval of the unpinned region is unknown in advance, making this problem to be a free mixed boundary value problem. To determine this interval of the unpinned part, we apply condition that the contact line is continuous and smooth at any time instant.

Chapter 6 employs the Cox-Voinov equation (Cox, 1986; Voinov, 1976) as the contact line model. The contact line is always in motion with its normal local velocity related to the local contact angle. In contrast to other models, in this model, the displacement of the contact line at each time instant is directly determined by its normal velocity, providing the evolution of the contact line. In the present model, the problem is addressed in two steps at each time instant. The first step is to determine the droplet shape and the contact angle at the current time instant, with a given position of the contact line, while the second step is to find the new position of the contact line at the next time instant. The entire problem is solved through a forward iteration process.

2

Mathematical formulation of the problem

Our objective is to investigate the dynamics of a droplet on a solid, time-dependent substrate. This chapter is organized as follows: section 2.1 provides a general description of the problem considered throughout this thesis and outlines the specific problem scenarios we address; sections 2.2 and 2.3 define fundamental quantities of the three-dimensional contact angle and the normal velocity of the contact line, respectively, which are later used to describe the dynamics of the droplet; in section 2.4, we calculate the axisymmetric shape of droplets on the flat surface and the radius of the contact line, serving as the initial conditions for all problems; section 2.5 explains the validity of the quasi-static approximation and the assumptions and conditions under which it holds.

2.1 Formulation of the problem and models of the contact line motion

The dynamics of a three-dimensional droplet placed on a solid time-varying substrate is investigated. The shape of the substrate is described by the equation $z = z_p(x, y, t)$ in the Cartesian coordinates (x, y, z), where the vertical z-axis is in the direction opposite to gravity, t is time, and the function $z_p(x, y, t)$ is given. The shape of the free surface of the droplet, $z = \eta(x, y, t)$, where $(x, y) \in S(t)$, is unknown in advance and should be determined together with the position of the contact line, $\Gamma(t)$. We restrict ourselves to a hydrophilic droplet, where the function $\eta(x, y, t)$ is single-valued. Here, $S(t)$ is the droplet projection onto the xy-plane, and the contact line $\Gamma(t)$ is a three-dimensional intersection line between the free surface of the droplet and the surface of the substrate. The projection of the contact line onto the xy-plane is the boundary of $S(t)$, denoted as $\partial S(t)$.

The effects of the liquid evaporation and condensation are assumed to be

negligible, so the volume of the droplet remains constant over time,

$$V_0 = \iint_{S(t)} [\eta(x, y, t) - z_p(x, y, t)] dx dy. \tag{2.1.1}$$

The domain of the droplet $\Omega(t)$ is described by

$$\Omega(t) = \{x, y, z \quad | \quad z_p(x, y, t) < z < \eta(x, y, t), \quad (x, y) \in S(t)\}. \tag{2.1.2}$$

We assume that the flow inside the droplet is inviscid, incompressible and irrotational. Here, we utilise the dimensionless parameter Reynolds number (Re) to demonstrate the assumption of inviscid flow, defined as the ratio of inertial forces to viscous forces within a fluid. The Reynolds number is given by the equation

$$\mathrm{Re} = \frac{\rho u L_d}{\mu}, \tag{2.1.3}$$

where ρ is the liquid density, u is the flow speed, and L_d is the characteristic length of the droplet, and μ is the dynamic viscosity of the fluid. For water as the working fluid, assuming $L_d = 5\,\mathrm{mm}$ and $u = 20\,\mathrm{mm\,s^{-1}}$, (following the results from Tsai et al. (2015)), the resulting Reynolds number is approximately 100, which implies that the viscous forces are much smaller than the inertial ones and can be neglected in the leading order. Please note that since we are considering a large droplet, gravity cannot be neglected in our study. Hence, the flow is described by the velocity potential $\phi(x, y, z, t)$, which satisfies Laplace's equation in the flow region,

$$\nabla^2 \phi = 0 \qquad ((x, y, z) \in \Omega(t)). \tag{2.1.4}$$

At the boundaries of the droplet, liquid particles can move only along the boundaries, but cannot leave the boundaries. This corresponds to the following kinematic boundary conditions at the free surface and substrate:

$$\frac{\partial \phi}{\partial z} = \frac{\partial \phi}{\partial x}\frac{\partial \eta}{\partial x} + \frac{\partial \phi}{\partial y}\frac{\partial \eta}{\partial y} + \frac{\partial \eta}{\partial t} \qquad (z = \eta(x, y, t), \quad (x, y) \in S(t)), \tag{2.1.5}$$

$$\frac{\partial \phi}{\partial z} = \frac{\partial \phi}{\partial x}\frac{\partial z_p}{\partial x} + \frac{\partial \phi}{\partial y}\frac{\partial z_p}{\partial y} + \frac{\partial z_p}{\partial t} \qquad (z = z_p(x, y, t), \quad (x, y) \in S(t)). \tag{2.1.6}$$

At the free surface of the droplet, we also have the following dynamic boundary condition,

$$p(x, y, z, t) = p_a + \gamma \kappa(x, y, t) \qquad (z = \eta(x, y, t), \quad (x, y) \in S(t)). \tag{2.1.7}$$

Here p_a is the atmospheric pressure outside the droplet, which is assumed constant, γ is the surface tension coefficient at the air/liquid interface, and

$\kappa(x, y, t)$ is the curvature of the free surface of the droplet. The curvature $\kappa(x, y, t)$ of the free surface is given by the divergence of the unit normal vector, $\mathbf{n_d} = \nabla(z - \eta(x, y, t))/|\nabla(z - \eta(x, y, t))|$, see details in Pressley (2010),

$$\kappa(x, y, t) = \nabla \cdot \left(\frac{\nabla(z - \eta(x, y, t))}{|\nabla(z - \eta(x, y, t))|} \right). \tag{2.1.8}$$

In the flow region, the hydrodynamic pressure, $p(x, y, z, t)$, is given by Bernoulli's equation,

$$p(x, y, z, t) = -\rho \left(\frac{\partial \phi}{\partial t} + \frac{1}{2}|\nabla \phi|^2 + gz \right) + f(t), \tag{2.1.9}$$

where g is the gravitational acceleration, and $f(t)$ is an unknown function of time that is to be determined. At the contact line,

$$\eta(x, y, t) = z_p(x, y, t) \qquad ((x, y) \in \partial S(t)). \tag{2.1.10}$$

The free surface of the droplet and the flow inside the droplet should be determined together with the position of the contact line $\Gamma(t)$. To solve this problem, one more condition is required, which depends on which contact line model is considered. In this thesis, four models of the contact line dynamics are investigated. Within each of these models, the surface of the substrate is allowed to move only in the z-direction. This simplification of the substrate motion does not affect equations (2.1.1)–(2.1.10), but only the dynamics of the contact line $\Gamma(t)$.

In the first model of the pinned contact line, we assume that the contact line does not move with respect to the substrate, which is that the projection $S(t)$ of the droplet onto the xy-plane does not change in time, $S(t) = S(0)$. In this model, the contact angle between the free surface and the substrate at the contact line, $\theta_c(x, y, t)$, where $(x, y) \in \partial S(0)$, should be determined as part of the solution. The definition of the contact angle in a three-dimensional problem will be given in section 2.2.

In the second model, the contact line $\Gamma(t)$ moves along the substrate in such a way that the contact angle at each point of the moving contact line is equal to the so-called equilibrium contact angle θ_e. The equation $\theta_c(x, y, t) = \theta_e$ governs the position of the contact line at each time instant. The value θ_e is assumed to be known. It is a characteristic of the liquid, the air above it, and the properties of the substrate surface.

In the third model, so-called advancing θ_a and receding θ_r contact angles are introduced, where $\theta_r < \theta_e < \theta_a$, see Gennes et al. (2004). They are given constants. We consider the situation where initially the droplet is axisymmetric, the substrate is flat, and the radius of the wetted part of the substrate, R_0, is such that the contact angle along $\Gamma(0)$ is equal to θ_e. Then deformations of

the substrate start at $t = 0$. The contact angle becomes a function of time, $\theta_c(x, y, t)$, but the contact line remains to be pinned if the inequalities, $\theta_r < \theta_c(x, y, t) < \theta_a$, are satisfied. If, at a certain part of the contact line $\Gamma(0)$, the contact angle $\theta_c(x, y, t)$ approaches either θ_a or θ_r, this part of the contact line is displaced such that $\theta_c(x, y, t)$ stays in the interval $[\theta_r, \theta_a]$. This model combines the first and second models in the way that $\theta_c = \theta_a$ or $\theta_c = \theta_r$ in moving parts of the contact line and $\theta_r < \theta_c < \theta_a$ along stationary parts of the contact line. The moving intervals of the contact line are unknown in advance and should be determined using the condition that the contact line and the tangent vector to it are continuous along $\Gamma(t)$ at each time instant.

The fourth model of the contact line motion is known as the Cox-Voinov model (Cox, 1986; Voinov, 1976). In this model, the contact line is always in motion with its normal velocity along the substrate surface being proportional to $\theta_c^3(x, y, t) - \theta_e^3$. The displacement of the contact line at each time instant is determined by computing the normal velocity of this line, which is not used in the third model, where the contact line displacement is determined directly. The normal velocity of the contact line will be defined in section 2.3.

In all four models, we need to know the contact angle $\theta_c(x, y, t)$ for given functions $z_p(x, y, t)$ and $\eta(x, y, t)$, and a given position of the contact line. Equations (2.1.1)–(2.1.10) together with a model of the contact line motion require initial conditions. The initial conditions are the same for any model. We assume that initially, $t = 0$, the substrate is flat, $z_p(x, y, 0) = 0$, the liquid in the droplet is at rest, the free surface of the droplet is axisymmetric, $z = \bar{\eta}_0(r)$, $r = \sqrt{x^2 + y^2}$, and the radius R_0 of the contact line $\Gamma(0)$ is such that the contact angle θ_c is equal to the equilibrium contact angle θ_e at any point of the contact line. $\bar{\eta}_0(r)$ and R_0 for given V_0, ρ, g and γ are calculated and investigated in section 2.4.

2.2 Equation for the contact angle

The contact angle, in general, is not constant and may vary along the moving contact line and in time. We denote the current local contact angle by $\theta_c(x, y, t)$ where $(x, y) \in \partial S(t)$. Calculations of $\theta_c(x, y, t)$ for given $\eta(x, y, t)$ and $z_p(x, y, t)$ are complicated in the three-dimensional space, so we explain these calculations for the two-dimensional case first. The unit tangent vectors of the droplet $\mathbf{T_d}$ and the solid surface $\mathbf{T_s}$ in the two-dimensional case are defined by

$$\mathbf{T_d} = \frac{\hat{\mathbf{i}} + \eta_x \hat{\mathbf{k}}}{\sqrt{1 + \eta_x^2}}, \qquad \mathbf{T_s} = \frac{\hat{\mathbf{i}} + z_{px} \hat{\mathbf{k}}}{\sqrt{1 + z_{p,x}^2}}, \tag{2.2.1}$$

where $\hat{\mathbf{i}}$, $\hat{\mathbf{k}}$ are the unit vectors in the directions x, z, respectively. The unit normal outer vectors to the surface of the droplet, $\mathbf{n_d}$, and to the solid surface, $\mathbf{n_s}$, in the two-dimensional case are

$$\mathbf{n_d} = \frac{-\eta_x \hat{\mathbf{i}} + \hat{\mathbf{k}}}{\sqrt{1+\eta_x^2}}, \qquad \mathbf{n_s} = \frac{-z_{px} \hat{\mathbf{i}} + \hat{\mathbf{k}}}{\sqrt{1+z_{px}^2}}. \tag{2.2.2}$$

In the two-dimensional setting, as depicted in Figure 2.2.1, the local current contact angle $\theta_c(x,t)$ is defined as the angle between the two tangent vectors, which is equal to the angle between the normal outer vectors $\mathbf{n_d}$ and $\mathbf{n_s}$,

$$\cos\theta_c(x,t) = \mathbf{T_s} \cdot \mathbf{T_d} = \mathbf{n_s} \cdot \mathbf{n_d} = \frac{1+\eta_x z_{px}}{\sqrt{(1+z_{px}^2)(1+\eta_x^2)}} \qquad (x \in \partial S(t)). \tag{2.2.3}$$

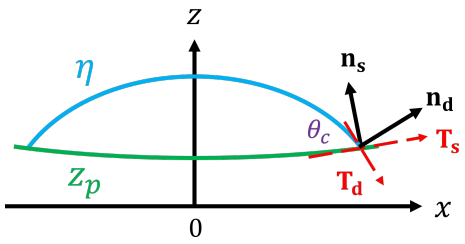

Figure 2.2.1: A sketch of the free surface of the droplet, $z = \eta(x,t)$, the solid surface, $z = z_p(x,t)$, the tangential vectors $\mathbf{T_d}$ and $\mathbf{T_s}$, and the normal vectors $\mathbf{n_d}$ and $\mathbf{n_s}$ in the two-dimensional case.

In the three-dimensional case, the current local contact angle $\theta_c(x,y,t)$ is defined as the angle between the free surface of the droplet and the surface of the substrate in the plane, which is perpendicular to the tangential vector to the three-dimensional contact line. The tangential vector to the contact line $\Gamma(t)$,

$$\mathbf{T_3} = \frac{q_1 \hat{\mathbf{i}} + q_2 \hat{\mathbf{j}} + q_3 \hat{\mathbf{k}}}{\sqrt{q_1^2+q_2^2+q_3^2}},$$

where $\hat{\mathbf{j}}$ is the unit vector in the y-direction, is orthogonal to both outer unit vectors to the droplet surface $\mathbf{n_d}$, and to the solid surface, $\mathbf{n_s}$, which are given by

$$\mathbf{n_d} = \frac{-\eta_x \hat{\mathbf{i}} - \eta_y \hat{\mathbf{j}} + \hat{\mathbf{k}}}{\sqrt{1+(\nabla_2 \eta)^2}}, \qquad \mathbf{n_s} = \frac{-z_{px} \hat{\mathbf{i}} - z_{py} \hat{\mathbf{j}} + \hat{\mathbf{k}}}{\sqrt{1+(\nabla_2 z_p)^2}}, \tag{2.2.4}$$

where ∇_2 is the two-dimensional gradient operator. Therefore, the plane P, see Figure 2.2.2, perpendicular to $\mathbf{T_3}$, is made of the normal vectors (2.2.4), and the

current local contact angle $\theta_c(x, y, t)$ can be calculated using the scalar product,

$$\cos\theta_c(x,y,t) = \mathbf{n_d} \cdot \mathbf{n_s} = \frac{\eta_x z_{px} + \eta_y z_{py} + 1}{\sqrt{1+(\nabla_2\eta)^2}\sqrt{1+(\nabla_2 z_p)^2}} \qquad ((x,y) \in \partial S(t)). \tag{2.2.5}$$

The tangential vector $\mathbf{T_3}$ can be obtained using the cross (vector) product,

$$\mathbf{T_3} = \mathbf{n_s} \times \mathbf{n_d} = \frac{q_1\hat{\mathbf{i}} + q_2\hat{\mathbf{j}} + q_3\hat{\mathbf{k}}}{\sqrt{q_1^2+q_2^2+q_3^2}} \qquad ((x,y) \in \partial S(t)), \tag{2.2.6}$$

where

$$q_1 = \eta_y - z_{py}, \qquad q_2 = z_{px} - \eta_x, \qquad q_3 = \eta_y z_{px} - \eta_x z_{py}.$$

The tangential vector $\mathbf{T_3}$ is positively oriented, which means that the flow domain $\Omega(t)$ is on the left when we are moving along the contact line in the direction of the vector $\mathbf{T_3}$.

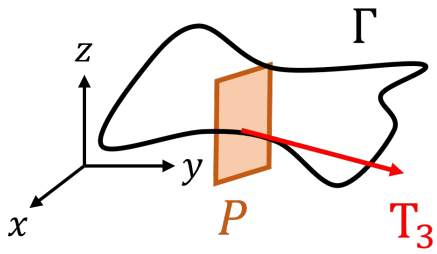

Figure 2.2.2: The plane P and the tangential vector $\mathbf{T_3}$ to the contact line.

2.3 Normal velocity of the contact line

In this study, we restrict ourselves to problems where the projection of the contact line, $\partial S(t)$, is about circular with a small perturbation such that this contact line can be described by equation $r = r_c(\varphi, t)$ in the polar coordinates, where $\varphi \in (-\pi, \pi)$ is the polar angle. The function $r_c(\varphi, t)$ should be determined if the contact line is not pinned. To define the velocity of the contact line in three-dimensional space, we first explain how the contact line moves along the surface of the substrate. The three-dimensional contact line $\Gamma(t)$ moves in the $\mathbf{n_3}$ direction, where the unit vector $\mathbf{n_3}$ is normal to $\Gamma(t)$ and tangential to the solid surface $z_p(x, y, t)$,

$$\mathbf{n_3} = \mathbf{T_3} \times \mathbf{n_s} = \frac{q_4\hat{\mathbf{i}} + q_5\hat{\mathbf{j}} + q_6\hat{\mathbf{k}}}{\sqrt{q_4^2+q_5^2+q_6^2}} \qquad ((x,y) \in \partial S(t)). \tag{2.3.1}$$

Here $\mathbf{T_3}$ is the unit tangential vector to the three-dimensional contact line $\Gamma(t)$ given by equation (2.2.6) and $\mathbf{n_s}$ is the unit normal vector to the solid surface,

see equation (2.2.4). The elements of equation (2.3.1) are

$$\begin{aligned} q_4 =& \eta_y z_{px} z_{py} - \eta_x z_{py}^2 + z_{px} - \eta_x, \\ q_5 =& \eta_x z_{px} z_{py} - \eta_y z_{px}^2 + z_{py} - \eta_y, \\ q_6 =& z_{px}^2 + z_{py}^2 - \eta_x z_{px} - \eta_y z_{py}. \end{aligned}$$

The contact line $\Gamma(t)$ can be described by using the only unknown function $r_c(\varphi, t)$ introduced above,

$$\Gamma(t) = \begin{cases} x = r_c(\varphi, t)\cos\varphi, \\ y = r_c(\varphi, t)\sin\varphi, \\ z = z_p(r_c(\varphi, t)\cos\varphi, r_c(\varphi, t)\sin\varphi, t). \end{cases} \tag{2.3.2}$$

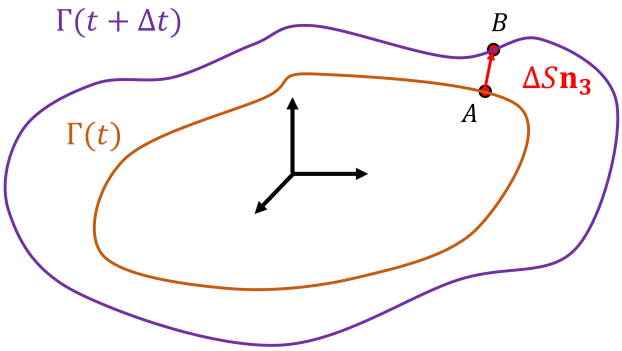

Figure 2.3.1: Scheme of the moving contact line along the substrate.

In Figure 2.3.1, the brown line depicts the position of the current contact line, while the purple line represents the position of the contact line at the subsequent time instant, $t + \Delta t$. The red arrow illustrates the displacement of the contact line in the normal direction $\mathbf{n_3}$ to $\Gamma(t)$, which is

$$\Delta S\mathbf{n_3} = \mathbf{X}(\varphi + \Delta\varphi, t + \Delta t) - \mathbf{X}(\varphi, t), \tag{2.3.3}$$

where ΔS represents the magnitude of the displacement, $\mathbf{X}(\varphi, t)$ is the position vector,

$$\mathbf{X}(\varphi, t) = r_c(\varphi, t)\cos\varphi\hat{\mathbf{i}} + r_c(\varphi, t)\sin\varphi\hat{\mathbf{j}} + z_p(r_c(\varphi, t)\cos\varphi, r_c(\varphi, t)\sin\varphi, t)\hat{\mathbf{k}},$$

of point A, and $\mathbf{X}(\varphi + \Delta\varphi, t + \Delta t)$ is the position vector of the point B, which is the intersection of $\mathbf{n_3}(\varphi, t)$ and $\Gamma(t + \Delta t)$. Note that the $\mathbf{n_3}$ direction may not follow the radial direction, so we need to consider a small change in the polar angle $\Delta\varphi$ for small Δt. Performing a Taylor expansion on equation (2.3.3), we

obtain

$$\mathbf{X}_\varphi(\varphi,t)\Delta\varphi + \mathbf{X}_t(\varphi,t)\Delta t = \Delta S \mathbf{n_3}, \tag{2.3.4}$$

where $\mathbf{X}_t = \dfrac{\partial \mathbf{X}}{\partial t}$, $\mathbf{X}_\varphi = \dfrac{\partial \mathbf{X}}{\partial \varphi}$ are the derivatives of the position vector:

$$\begin{aligned}
\mathbf{X}_t(\varphi,t) =& \left(\frac{\partial r_c}{\partial t}\cos\varphi\right)\hat{\mathbf{i}} + \left(\frac{\partial r_c}{\partial t}\sin\varphi\right)\hat{\mathbf{j}} \\
&+ \left(z_{px}\frac{\partial r_c}{\partial t}\cos\varphi + z_{py}\frac{\partial r_c}{\partial t}\sin\varphi + \frac{\partial z_p}{\partial t}\right)\hat{\mathbf{k}}, \\
\mathbf{X}_\varphi(\varphi,t) =& \left(\frac{\partial r_c}{\partial \varphi}\cos\varphi - r_c\sin\varphi\right)\hat{\mathbf{i}} + \left(\frac{\partial r_c}{\partial \varphi}\sin\varphi + r_c\cos\varphi\right)\hat{\mathbf{j}} \\
&+ \left(z_{px}\left[\frac{\partial r_c}{\partial \varphi}\cos\varphi - r_c\sin\varphi\right] + z_{py}\left[\frac{\partial r_c}{\partial \varphi}\sin\varphi + r_c\cos\varphi\right]\right)\hat{\mathbf{k}}.
\end{aligned}$$

Taking the product of equation (2.3.4) with the tangential vector $\mathbf{T_3}$, we have

$$\Delta\varphi = -\frac{\mathbf{X}_t(\varphi,t)\cdot\mathbf{T_3}}{\mathbf{X}_\varphi(\varphi,t)\cdot\mathbf{T_3}}\Delta t. \tag{2.3.5}$$

The vector $\mathbf{X}_\varphi$ equals zero if and only if both equations $\frac{\partial r_c}{\partial \varphi}\cos\varphi - r_c\sin\varphi = 0$ and $\frac{\partial r_c}{\partial \varphi}\sin\varphi + r_c\cos\varphi = 0$ must be satisfied. The former equation gives $r_c = \sec(\varphi)$, and the latter yields $r_c = \csc(\varphi)$. Therefore, for non-zero function $r_c(\varphi,t)$, we have nonzero $\mathbf{X}_\varphi$. Note that both vectors $\mathbf{X}_\varphi$ and $\mathbf{T_3}$ are tangent to the contact line $\Gamma(t)$. Therefore, the scalar product in the denominator of (2.3.5) is equal to $|\mathbf{X}_\varphi|\cdot|\mathbf{T_3}|$ and cannot be equal to zero.

Taking the product of equation (2.3.4) with $\mathbf{n_3}$ and using equation (2.3.5), we obtain

$$\begin{aligned}
\Delta S =& \mathbf{X}_\varphi(\varphi,t)\cdot\mathbf{n_3}\left(-\frac{\mathbf{X}_t(\varphi,t)\cdot\mathbf{T_3}}{\mathbf{X}_\varphi(\varphi,t)\cdot\mathbf{T_3}}\Delta t\right) + \mathbf{X}_t(\varphi,t)\cdot\mathbf{n_3}\Delta t, \\
=& \mathbf{X}_t(\varphi,t)\cdot\left(\mathbf{n_3} - \frac{\mathbf{X}_\varphi(\varphi,t)\cdot\mathbf{n_3}}{\mathbf{X}_\varphi(\varphi,t)\cdot\mathbf{T_3}}\mathbf{T_3}\right)\Delta t.
\end{aligned} \tag{2.3.6}$$

Hence, the velocity of the contact line moving in the normal $\mathbf{n_3}$ direction is defined by

$$V_n = \lim_{\Delta t\to 0}\frac{\Delta S}{\Delta t} = \mathbf{X}_t(\varphi,t)\cdot\left(\mathbf{n_3} - \frac{\mathbf{X}_\varphi(\varphi,t)\cdot\mathbf{n_3}}{\mathbf{X}_\varphi(\varphi,t)\cdot\mathbf{T_3}}\mathbf{T_3}\right). \tag{2.3.7}$$

It is convenient to write all vectors in equation (2.3.7) in the cylindrical coordinates (r,φ,z). In these coordinates, the droplet surface and solid surface are described by the equations $z = \bar{\eta}(r,\varphi,t)$ and $z = \bar{z}_p(r,\varphi,t)$ accordingly, where

$$\begin{aligned}
\eta(r\cos\varphi, r\sin\varphi, t) =& \bar{\eta}(r,\varphi,t), \\
z_p(r\cos\varphi, r\sin\varphi, t) =& \bar{z}_p(r,\varphi,t).
\end{aligned}$$

Then, the unit tangential vector to the contact line (2.2.6) becomes

$$\mathbf{T_3} = \frac{\bar{q}_1\hat{\mathbf{e}}_\mathbf{r} + \bar{q}_2\hat{\mathbf{e}}_\varphi + \bar{q}_3\hat{\mathbf{k}}}{\sqrt{\bar{q}_1^2 + \bar{q}_2^2 + \bar{q}_3^2}} \qquad (r = r_c(\varphi, t)), \tag{2.3.8}$$

where $\hat{\mathbf{e}}_\mathbf{r}$, $\hat{\mathbf{e}}_\varphi$ represent the unit vectors in the radial and azimuthal direction in the cylindrical coordinates, and

$$\bar{q}_1 = \frac{\bar{\eta}_\varphi - \bar{z}_{p\varphi}}{r}, \qquad \bar{q}_2 = \bar{z}_{pr} - \bar{\eta}_r, \qquad \bar{q}_3 = \frac{\bar{z}_{pr}\bar{\eta}_\varphi - \bar{\eta}_r\bar{z}_{p\varphi}}{r}.$$

The unit normal vector (2.3.1) is now represented by

$$\mathbf{n_3} = \frac{\bar{q}_4\hat{\mathbf{e}}_\mathbf{r} + \bar{q}_5\hat{\mathbf{e}}_\varphi + \bar{q}_6\hat{\mathbf{k}}}{\sqrt{\bar{q}_4^2 + \bar{q}_5^2 + \bar{q}_6^2}} \qquad (r = r_c(\varphi, t)), \tag{2.3.9}$$

where

$$\begin{aligned}
\bar{q}_4 =& \bar{z}_{pr} - \bar{\eta}_r + \frac{\bar{z}_{pr}\bar{\eta}_\varphi\bar{z}_{p\varphi} - \bar{\eta}_r\bar{z}_{p\varphi}^2}{r^2},\\
\bar{q}_5 =& \frac{\bar{\eta}_r\bar{z}_{pr}\bar{z}_{p\varphi} - \bar{z}_{pr}^2\bar{\eta}_\varphi + \bar{z}_{p\varphi} - \bar{\eta}_\varphi}{r},\\
\bar{q}_6 =& \bar{z}_{pr}^2 - \bar{\eta}_r\bar{z}_{pr} + \frac{\bar{z}_{p\varphi}^2 - \bar{\eta}_\varphi\bar{z}_{p\varphi}}{r^2}.
\end{aligned}$$

The derivatives of the position vector in the cylindrical coordinates can be written in the form,

$$\begin{aligned}
\mathbf{X}_t(\varphi, t) =& \frac{\partial r_c}{\partial t}\hat{\mathbf{e}}_\mathbf{r} + 0\hat{\mathbf{e}}_\varphi + \left(\bar{z}_{pr}\frac{\partial r_c}{\partial t} + \bar{z}_{pt}\right)\hat{\mathbf{k}},\\
\mathbf{X}_\varphi(\varphi, t) =& \frac{\partial r_c}{\partial \varphi}\hat{\mathbf{e}}_\mathbf{r} + r_c\hat{\mathbf{e}}_\varphi + \left(\bar{z}_{pr}\frac{\partial r_c}{\partial \varphi} + \bar{z}_{p\varphi}\right)\hat{\mathbf{k}}.
\end{aligned} \tag{2.3.10}$$

Substituting equations (2.3.8)–(2.3.10) into (2.3.7), we obtain the normal velocity of the contact line in terms of $r_c(\varphi, t)$ and its first derivatives.

2.4 Initial shape of droplet

Initial droplet shape, $\eta(x, y, 0)$, and the initial position of the contact line are required as initial conditions in the problem of the droplet dynamics on a time-varying substrate. We assume that initially, the substrate is flat and horizontal, and the droplet is axisymmetric, with the contact line being a circle of radius R_0. In this static problem, the volume of the droplet is known, and the contact angle $\theta_c(\varphi, 0)$ at any point of the contact line is equal to the equilibrium contact angle θ_e.

In this section, we begin by formulating this static problem in the Cartesian coordinates and then converting it into dimensionless cylindrical coordinates to

benefit our analysis. There is no exact analytical solution for this problem, so we use a numerical approach for moderate droplet volumes and asymptotic analysis for large droplets. These methods yield results that show good agreement.

2.4.1 Formulation of the static axisymmetric problem

Let the static free surface of the droplet and the solid surface be described by the equations $z = \eta(x, y)$ and $z = z_p(x, y)$, respectively. The projection of the droplet onto the $z = 0$ plane is $S(0)$, and the boundary of this projection is $\partial S(0)$, see section 2.1. For a flat horizontal substrate, $z_p(x, y) = 0$, the volume of the droplet, V_0, is given by

$$V_0 = \iint_{S(0)} \eta(x, y) dxdy. \tag{2.4.1}$$

In the static problem, the shape of the droplet is determined only by the dynamic boundary condition (2.1.7) where the pressure is the hydrostatic pressure, see equation (2.1.9). In other words, the equilibrium state is achieved when the pressure on the free surface of the droplet is balanced by the hydrostatic pressure and the capillary pressure, resulting in the governing equation, which is known as the Young-Laplace equation (Young, 1805),

$$-\gamma \nabla_2 \cdot \left(\frac{\nabla_2 \eta(x, y)}{\sqrt{1 + (\nabla_2 \eta)^2}} \right) = \rho g (B - \eta(x, y)) \qquad ((x, y) \in S(0)), \tag{2.4.2}$$

where γ is the surface tension coefficient at the air/liquid interface, ρ is the density of the fluid, g is the gravitational constant, and B is an unknown constant to be determined. This constant can be related to the volume of the droplet, the wetted area of the substrate, and the equilibrium contact angle θ_e. To find this relation, we integrate the governing equation (2.4.2) over the region $S(0)$ and use equation (2.4.1). This gives

$$-\gamma \iint_{S(0)} \nabla_2 \cdot \left(\frac{\nabla_2 \eta(x, y)}{\sqrt{1 + (\nabla_2 \eta)^2}} \right) dxdy = \rho g \left(B|S| - V_0 \right), \tag{2.4.3}$$

where $|S| = \iint_S dxdy$ is the area of the wetted part of the substrate. Utilising the divergence theorem, the left-hand side of equation (2.4.3) is expressed as

$$-\gamma \iint_{S(0)} \nabla_2 \cdot \left(\frac{\nabla_2 \eta(x, y)}{\sqrt{1 + (\nabla_2 \eta)^2}} \right) dxdy = -\gamma \int_{\partial S(0)} \frac{\nabla_2 \eta(x, y) \cdot \mathbf{n_2}}{\sqrt{1 + (\nabla_2 \eta)^2}} ds,$$

where ds is a infinitesimal element of the two-dimensional contact line $\partial S(0)$, and $\mathbf{n_2}$ is the outward unit normal vector at $\partial S(0)$ for the flat substrate. Equation

(2.4.3) therefore becomes

$$-\gamma \int_{\partial S(0)} \frac{\nabla_2 \eta(x,y) \cdot \mathbf{n_2}}{\sqrt{1+(\nabla_2 \eta)^2}} ds = \rho g \left(B|S| - V_0 \right), \tag{2.4.4}$$

The condition (2.4.4) is a relation between the two-dimensional contact line $\partial S(0)$, the droplet shape $\eta(x,y)$, the droplet volume V_0 and the constant B.

The problem under consideration is a free boundary-value problem. Not only the free surface of the droplet, $z = \eta(x,y)$, needs to be determined, but the contact line, $\partial S(0)$ as well. Therefore, we need to determine both the shape of the droplet and the region in which it is defined. Equation (2.4.2) is a second-order, nonlinear partial differential equation. In the case of a flat solid surface, the height of the droplet at the contact line is zero, which leads to the following boundary condition,

$$\eta(x,y) = 0 \qquad ((x,y) \in \partial S(0)). \tag{2.4.5}$$

Once equation (2.4.2) with the boundary condition (2.4.5) and the condition (2.4.4) has been solved for a given $\partial S(0)$, the contact angle $\theta_c(x,y,0)$ is then calculated by equation (2.2.5),

$$\cos\theta_c(x,y,0) = \frac{1}{\sqrt{1+(\nabla_2 \eta)^2}} \qquad ((x,y) \in \partial S(0)). \tag{2.4.6}$$

This equation provides $\tan\theta_c(x,y,0) = \pm|\nabla_2 \eta|$, where the positive sign is for θ_c in the range $0 < \theta_c < \pi/2$ (hydrophilic surface), and minus for $\pi/2 < \theta_c < \pi$ (hydrophobic surface). We search for a solution such that

$$\theta_c(x,y,0) = \theta_e \qquad ((x,y) \in \partial S(0)). \tag{2.4.7}$$

The latter condition serves to determine the contact line $\partial S(0)$.

We assume that the resulting contact line is a circle and the shape of the droplet is axisymmetric. It is convenient to formulate the axisymmetric problem in the polar coordinates. In the polar coordinates, the shape of the droplet depends only on the radial coordinate r, which is described by $z = \bar{\eta}(r)$, where $x = r\cos\varphi$, $y = r\sin\varphi$, $-\pi < \varphi < \pi$, and $r < R_0$. Then the curvature can be expressed as (Peters, 2001),

$$\kappa = -\left(\frac{\bar{\eta}_{rr}}{(1+\bar{\eta}_r^2)^{3/2}} + \frac{\bar{\eta}_r}{r(1+\bar{\eta}_r^2)^{1/2}} \right).$$

Hence, in the cylindrical coordinates, the governing equation (2.4.2) reads

$$-\gamma \left(\frac{\bar{\eta}_{rr}}{(1+\bar{\eta}_r^2)^{3/2}} + \frac{\bar{\eta}_r}{r(1+\bar{\eta}_r^2)^{1/2}} \right) = \rho g (B - \bar{\eta}(r)) \qquad (r < R_0), \tag{2.4.8}$$

where R_0 is the radius of the contact line. Note that the constant R_0 should be determined together with the solution of the equation (2.4.8) subject to the boundary conditions,

$$\bar{\eta}(R_0) = 0, \tag{2.4.9}$$

and

$$\bar{\eta}_r(0) = 0. \tag{2.4.10}$$

The condition (2.4.10) comes from the condition that the axisymmetric surface of the droplet is smooth with finite and continuous curvature. The condition (2.4.7) that the contact angle along the contact line is equal to the equilibrium contact angle θ_e and equation (2.4.6) provide the second condition at the contact line,

$$\bar{\eta}_r(R_0) = -\tan\theta_e. \tag{2.4.11}$$

The normal unit vector $\mathbf{n_2} = \hat{\mathbf{e}}_\mathbf{r}$ in the polar coordinates. The left-hand side of (2.4.4) can now be expressed as

$$\begin{aligned} -\gamma \int_{\partial S} \frac{\nabla_2 \eta(x,y) \cdot \mathbf{n_2}}{\sqrt{1+(\nabla_2 \eta)^2}} ds &= -\gamma \int_0^{2\pi} \frac{\bar{\eta}_r(R_0)}{\sqrt{1+(\bar{\eta}_r(R_0))^2}} R_0 d\varphi, \\ &= 2\pi\gamma R_0 \sin\theta_e. \end{aligned} \tag{2.4.12}$$

In the axisymmetric case, the projection of the contact area is given by $|S| = \pi R_0^2$. Equations (2.4.4) and (2.4.12) provide

$$B = \frac{2\gamma \sin\theta_e}{\rho g R_0} + \frac{V_0}{\pi R_0^2}. \tag{2.4.13}$$

In equation (2.4.13), V_0, γ, g and θ_e are given but the radius R_0 of the contact line is still undetermined.

The axisymmetric problem given by equations (2.4.8)–(2.4.13) will be considered in dimensionless variables. Employing dimensionless variables facilitates the analysis, interpretation, and generalization of equations and results. It also enables us to gain a deeper understanding of the underlying physics and enables more efficient problem-solving. The variables are scaled by R_0 in the radial direction and by B in the vertical direction. A tilde symbol denotes the dimensionless variables,

$$r = R_0 \tilde{r}, \qquad z = B\tilde{z}, \qquad \bar{\eta} = B\tilde{\eta}(\tilde{r}). \tag{2.4.14}$$

Note that R_0 is still unknown and B is related to R_0 by equation (2.4.13). Here $\tilde{r}$ represents the dimensionless radius, and the dimensionless droplet surface is

described by $\tilde{z} = \tilde{\eta}(\tilde{r})$. The derivatives of the droplet shape are transformed as

$$\bar{\eta}_r(r) = \frac{d\bar{\eta}}{dr} = \frac{B}{R_0}\frac{d\tilde{\eta}}{d\tilde{r}} = \frac{B}{R_0}\tilde{\eta}_{\tilde{r}}(\tilde{r}), \qquad \bar{\eta}_{rr}(r) = \frac{B}{R_0^2}\tilde{\eta}_{\tilde{r}\tilde{r}}(\tilde{r}).$$

Substituting the above transformations of the variables and their derivatives into equation (2.4.8) and dividing both sides by $\rho g B$, we arrive at the governing equation in the dimensionless cylindrical coordinates,

$$-\frac{1}{Bo}\left(\frac{\tilde{\eta}_{\tilde{r}\tilde{r}}}{(1+\varepsilon_0^2\tilde{\eta}_{\tilde{r}}^2)^{3/2}} + \frac{\tilde{\eta}_{\tilde{r}}}{\tilde{r}(1+\varepsilon_0^2\tilde{\eta}_{\tilde{r}}^2)^{1/2}}\right) = 1 - \tilde{\eta}(\tilde{r}) \qquad (\tilde{r} \le 1). \tag{2.4.15}$$

This is a second-order non-linear ordinary differential equation with a singular coefficient at $\tilde{r} = 0$. There are two unknown parameters, $Bo = \rho g R_0^2/\gamma$, which is the Bond number, and $\varepsilon_0 = B/R_0$, which is the aspect ratio of the droplet. The boundary conditions in the dimensionless cylindrical coordinate are given by

$$\tilde{\eta}(1) = 0, \tag{2.4.16}$$

$$\tilde{\eta}_{\tilde{r}}(1) = -\frac{\tan\theta_e}{\varepsilon_0}, \tag{2.4.17}$$

$$\tilde{\eta}_{\tilde{r}}(0) = 0. \tag{2.4.18}$$

Equation (2.4.13) divided by R_0 provides

$$\varepsilon_0 = \frac{V_0}{\pi R_0^3} + \frac{2\sin\theta_e}{Bo}. \tag{2.4.19}$$

Thus, we derived the ordinary differential equation (2.4.15) which should be solved subject to the boundary conditions (2.4.16)–(2.4.18), where ε_0 is related to the Bond number Bo and the dimensionless volume, $V_0/(\pi R_0^3)$, of the droplet by equation (2.4.19).

2.4.2 Solution

The problem (2.4.15)–(2.4.19) is solved using a numerical approach and the asymptotic analysis. This is a free boundary value problem since the contact radius is unknown in advance. Consequently, the associated parameters, the Bond number Bo and aspect ratio ε_0, which are involved in the governing equation, are also unknown. Moreover, the boundary condition (2.4.17) includes the parameter ε_0. Taking into account the complexity of the problem, we solve it numerically.

Numerical solution

Using the MATLAB function bvp4c.m, we can efficiently solve the boundary value problem (2.4.15), (2.4.17), (2.4.18) numerically for given Bo, ε_0, θ_e. bvp4c

is a finite difference code that employs a collocation technique to address a system of first-order ordinary differential equations while satisfying specified boundary conditions. This collocation technique creates a mesh of points, dividing the integration interval into smaller subintervals. The solver then generates a numerical solution by addressing a global system of algebraic equations. These equations emerge from both the boundary conditions and the collocation conditions applied to each subinterval. Within each subinterval, the solution is approximated using a cubic spline. These splines are determined by ensuring the continuity of the solution and its first derivative across the entire interval, satisfying the boundary conditions, and ensuring that the ordinary differential equations are satisfied at the midpoint and endpoints of each subinterval.

This collocation approach provides a C^1-continuous numerical solution, and it has been demonstrated to be fourth-order accurate uniformly throughout the integration interval (Kierzenka and Shampine, 2001). These conditions often lead to a nonlinear system of algebraic equations used to determine the spline coefficients. This system is solved using Newton's method.

The bvp4c solver is designed to handle systems of first-order ordinary differential equations,

$$y^{'}(x) = f(x, y), \qquad I_a < x < I_b, \tag{2.4.20}$$

where I_a and I_b are the start and end points of the integration interval. To apply this solver to our second-order ordinary differential equation, we need to transform our problem into a system of first-order ordinary differential equations. Setting $y_1 = \tilde{\eta}$ and $y_2 = \tilde{\eta}_{\tilde{r}}$, equation (2.4.15) can be rewritten as a system of first-order ordinary differential equations,

$$\begin{cases} y_1^{'} = y_2, \\ y_2^{'} = Bo(y_1 - 1)(1 + \varepsilon_0^2 y_2^2)^{3/2} - \dfrac{y_2}{\tilde{r}}(1 + \varepsilon_0^2 y_2^2). \end{cases} \tag{2.4.21}$$

The system is solved subject to the boundary conditions

$$\begin{cases} y_2(0) = 0, \\ y_2(1) = -\dfrac{1}{\varepsilon_0}\tan\theta_e. \end{cases} \tag{2.4.22}$$

The solver finds the numerical solution with an iterative approach. The iterations are naturally controlled by the residual error, which is defined as

$$e(x) = |s^{'}(x) - f(x, s(x))|. \tag{2.4.23}$$

Here, $s(x)$ represents the numerical solution achieved through spline

discretisations. If $e(x)$ does not meet the desired tolerance, which is taken as 10^{-4} in the present study, the bvp4c solver adapts the mesh. This adaptation process involves increasing the number of subintervals or adjusting their positions within the interval. As a result, a new numerical solution $s(x)$ is computed, and its corresponding error $e(x)$ is calculated. Calculations stop when the error (2.4.23) is below the specified tolerance.

The numerical process starts by specifying the involved physical parameters: the gravitational acceleration g, surface tension coefficient of the fluid γ, and density of the fluid ρ. Next, we assign the droplet volume V_0 and the equilibrium contact angle θ_e. After that, we estimate the contact radius R_0 using the geometrical properties of a hemispherical shape without accounting for gravitational effects. Once we have the estimated value of R_0, we calculate Bo and ε_0. Then, we solve the boundary value problem (2.4.15), (2.4.17), (2.4.18) numerically and compare the calculated value of $\tilde{\eta}(1)$ with zero as it is stated in equation (2.4.16). If $|\tilde{\eta}(1)|$ exceeds the error tolerance, we change the contact radius and repeat the calculations with updated R_0.
The algorithm for solving the problem is as follows:

1. Set the values of the physical parameters ρ, g, γ.
2. Set the equilibrium contact angle θ_e and the droplet volume V_0.
3. Select a contact radius R_0, then calculate the Bond number Bo and ε_0 using equation (2.4.19).
4. Solve the governing equation (2.4.15) numerically, employing the boundary conditions (2.4.17) and (2.4.18).
5. Check whether the solution satisfies the boundary condition (2.4.16). If it does not, update R_0 accordingly and repeat steps 3 and 4 until a satisfactory solution is obtained.

Following this algorithm, we can effectively solve the problem and find an accurate solution. We first examine the cases with $V_0 = 0.1\,\mathrm{mL}$ and the equilibrium contact angle θ_e ranging from 20° to 80°. Other parameters for water are $g = 9.8\,\mathrm{m\,s^{-2}}$, $\gamma = 72\,\mathrm{mN\,m^{-2}}$, $\rho = 999\,\mathrm{kg\,m^{-3}}$. Unless stated otherwise, we will use these same parameters throughout this thesis. The shape of the free surface of the droplet is shown in Figure 2.4.1. Different equilibrium contact angles correspond to different values of the Bond number, which are shown in the figure. The dimensionless variables are such that the radius of the droplet and its vertical scale are equal to one. The higher contact angles correspond to the lower Bond number and larger aspect ratio. The same shapes are presented in Figure 2.4.2 in the dimensional variables. The droplet shape approaches a spherical one as the contact angle increases. On the other hand, when the equilibrium contact angle

is small, the droplet shape becomes flatter and more spread out. Note that the shapes in Figure 2.4.2 are very different but they are very close one to another in the dimensionless variables, see Figure 2.4.1.

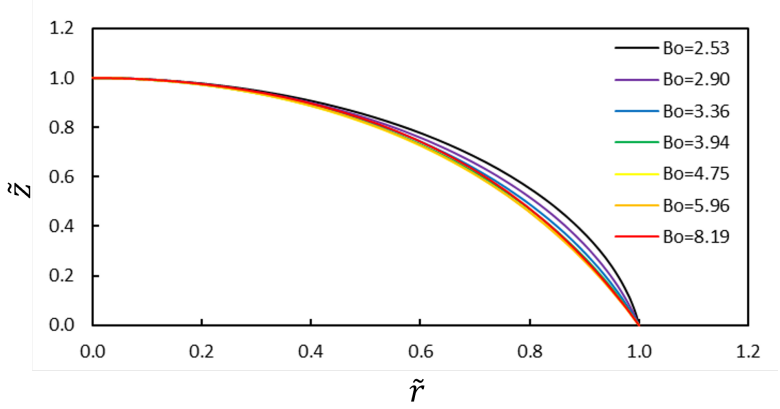

Figure 2.4.1: Different droplet shapes correspond to various Bond numbers, each associated with different values of the equilibrium contact angle θ_e.

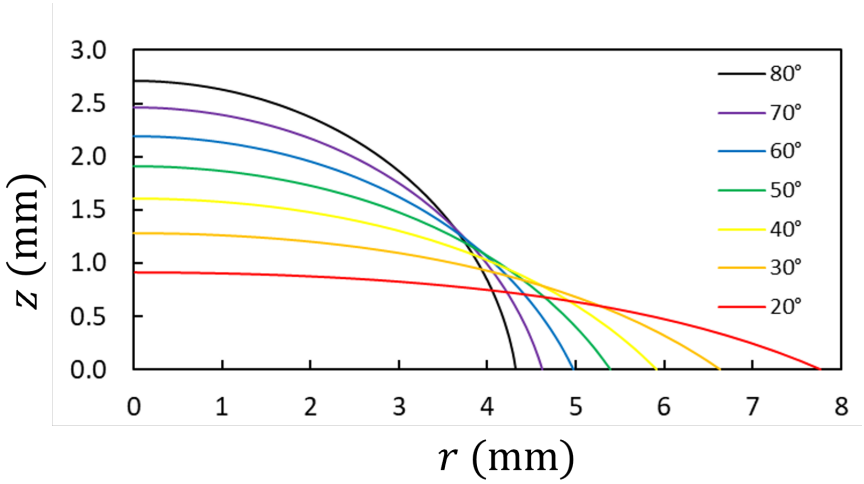

Figure 2.4.2: Droplet shapes in dimensional units for different values of the equilibrium contact angle θ_e.

We now discuss the effect of droplet volume while maintaining the same contact angle $\theta_e = 70°$, as depicted in Figure 2.4.3, where larger volumes correspond to larger Bond numbers. The results were then converted into figures with the dimensional parameters. Figure 2.4.4 depicts the droplet shape for volumes ranging from 0.1 mL to 1 mL, while Figure 2.4.5 shows the droplet shapes from 1 mL to 10 mL. For small droplet volumes, we observe a consistent increase in both the thickness and radius of the droplet as the volume increases. However, for larger volumes, although the radius R_0 continues to increase, the maximum thickness of the droplet remains relatively constant. Notably, the maximum height of the droplet at the largest volume is less than that of the

smaller volume. Further increase of the droplet volume leads to numerical problems.

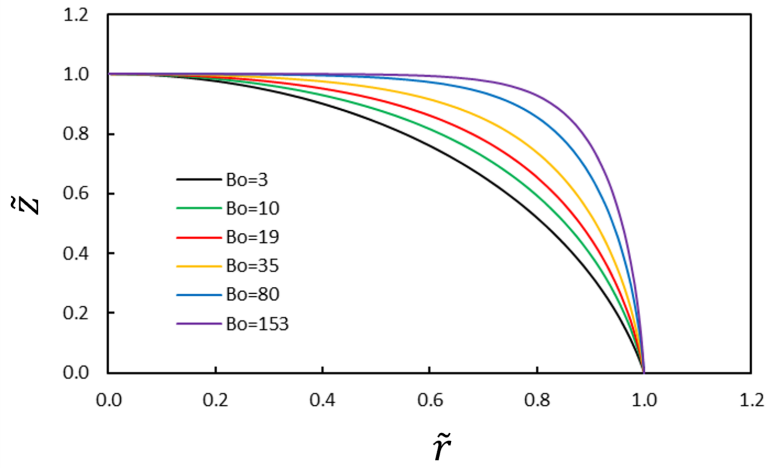

Figure 2.4.3: Droplet shapes correspond to various Bond numbers, each associated with different values of the droplet volume V_0.

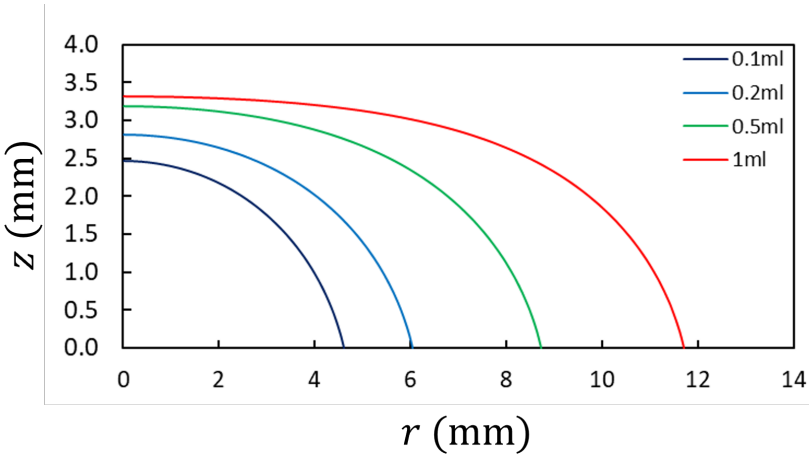

Figure 2.4.4: Droplet shapes for the volumes V_0 from 0.1 mL to 1 mL.

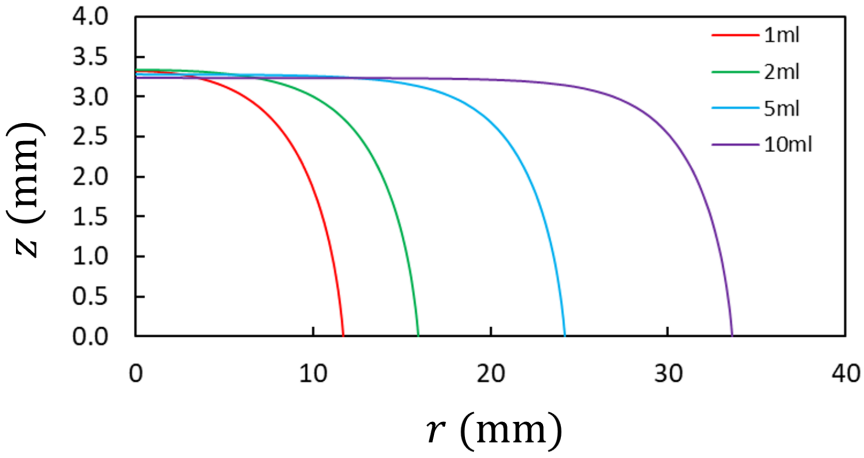

Figure 2.4.5: Droplet shapes for larger volumes from 1 mL to 10 mL.

The numerical results show that the thickness of the droplet becomes constant far from the contact line for large volumes of the droplet. This gives us an idea that the static shape of a large droplet can be described using methods of asymptotic analysis.

Asymptotic solution

Figure 2.4.5 suggests that for large volume V_0, we can subdivide the droplet into the main and inner regions, as Figure 2.4.6 shows. In the main region, the height of the drop is constant, which means the liquid surface is approximately flat, and its curvature is almost zero. Compared to the main region, the inner region is small. This section follows the approaches by Gennes et al. (2004).

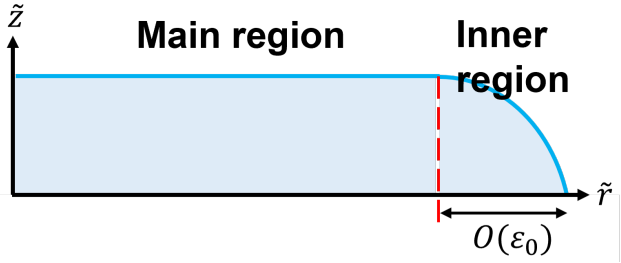

Figure 2.4.6: Main and inner regions in a sessile drop for large volumes

In the inner region near the contact line, the surface tension and gravity balance each other determining locally the droplet shape in the leading order as $\varepsilon_0 \to 0$. We introduce the inner variables:

$$\tilde{r} = 1 + \varepsilon_0 \lambda \qquad (\lambda < 0), \tag{2.4.24}$$

$$\tilde{\eta}(\tilde{r}) = \tilde{\eta}(1 + \varepsilon_0 \lambda) = h(\lambda, \varepsilon_0), \tag{2.4.25}$$

where $h(\lambda, \varepsilon_0)$ is the thickness of the droplet in the inner region. The derivatives of the droplet shape with respect to λ are

$$h_\lambda(\lambda) = \varepsilon_0 \tilde{\eta}_{\tilde{r}}(\tilde{r}), \qquad h_{\lambda\lambda}(\lambda) = \varepsilon_0^2 \tilde{\eta}_{\tilde{r}\tilde{r}}(\tilde{r}).$$

For small aspect ratio, $\varepsilon_0 \ll 1$, the Bond number can be expressed as

$$Bo = \left(\frac{R_0}{l_c}\right)^2 = \frac{1}{\varepsilon_0^2}\left(\frac{B}{l_c}\right)^2, \tag{2.4.26}$$

where $l_c = \sqrt{\dfrac{\gamma}{\rho g}}$ is the capillary length and $\dfrac{B}{l_c} = O(1)$ as $\varepsilon_0 \to 0$. Substituting the above relations into equation (2.4.15), we obtain

$$-\left(\frac{l_c}{B}\right)^2 \left(\frac{h_{\lambda\lambda}}{(1+h_\lambda^2)^{3/2}} + \frac{\varepsilon_0 h_\lambda}{(1+\varepsilon_0\lambda)(1+h_\lambda^2)^{1/2}}\right) = 1 - h(\lambda). \tag{2.4.27}$$

In the leading order as $\varepsilon_0 \to 0$, equation (2.4.27) gives

$$-\left(\frac{l_c}{B}\right)^2 \frac{h_{\lambda\lambda}}{(1+h_\lambda^2)^{3/2}} = 1 - h(\lambda). \tag{2.4.28}$$

Equation (2.4.28) is solved subject to the boundary conditions

$$\begin{aligned} h(0) &= 0, \\ h_\lambda(0) &= -\tan\theta_e, \end{aligned} \tag{2.4.29}$$

which follow from equation (2.4.16) and (2.4.17). In addition, the inner solution should match the leading order solution in the main region far from the contact line, where the curvature is constant, as illustrated in Figure 2.4.7. Thus, we have two matching conditions for equation (2.4.27), which is represented by

$$\begin{aligned} h(\lambda) &\to 1 \qquad (\lambda \to -\infty), \\ h_\lambda(\lambda) &\to 0 \qquad (\lambda \to -\infty). \end{aligned} \tag{2.4.30}$$

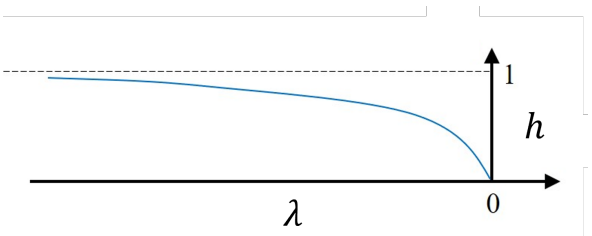

Figure 2.4.7: A schematic diagram for the boundary conditions in the inner region and the matching conditions to the main region.

Multiplying equation (2.4.28) by h_λ, and integrating both sides with respect

to λ, we obtain

$$\left(\frac{l_c}{B}\right)^2 \frac{1}{\sqrt{1+h_\lambda^2}} = h - \frac{1}{2}h^2 + C, \tag{2.4.31}$$

where C is an integration constant. By applying the boundary conditions (2.4.29) and the matching conditions (2.4.30), we arrive at two equations for B and C:

$$C = \left(\frac{l_c}{B}\right)^2 \cos\theta_e \qquad (\lambda = 0),$$
$$C = \left(\frac{l_c}{B}\right)^2 - \frac{1}{2} \qquad (\lambda \to -\infty),$$

which give

$$C = \frac{1}{2}\frac{\cos\theta_e}{1-\cos\theta_e}, \tag{2.4.32}$$
$$\frac{l_c}{B} = \frac{1}{\sqrt{2}}\frac{1}{\sqrt{1-\cos\theta_e}} = \frac{1}{2\sin(\theta_e/2)}. \tag{2.4.33}$$

Equation (2.4.33) yields that the thickness of the large droplet far from the contact line is approximately equal to

$$B = 2l_c \sin(\theta_e/2), \tag{2.4.34}$$

which is independent of the droplet volume, as we observed in Figure 2.4.4 and 2.4.5. Comparison of the thickness of the droplet given by equation (2.4.34) with the numerical results, as depicted in Figure 2.4.8. In this example, we set the parameter $\theta_e = 70°$. As the droplet volume increases, the numerical solutions approach the asymptotic solution.

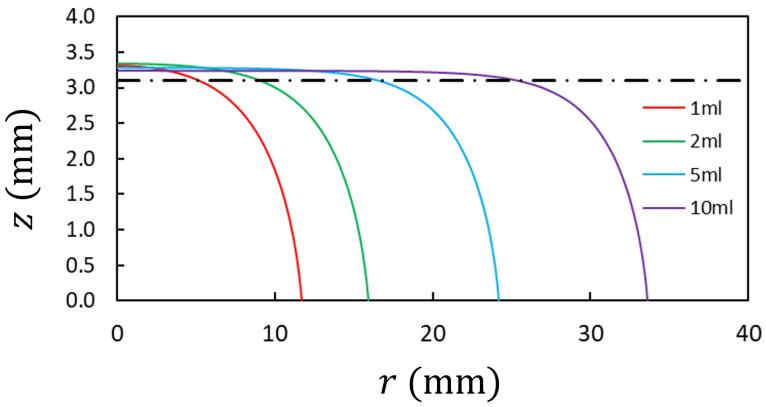

Figure 2.4.8: Thickness of the droplet for the large volumes. The asymptotic value (2.4.34) is shown by the dashed-dotted line.

Assuming that the part of the droplet near its periphery with non-flat free

upper boundary is small, we can estimate the radius of the droplet using the asymptotic leading-order solution as

$$\pi R_0^2 B \approx V_0, \tag{2.4.35}$$

where B is given by equation (2.4.34). Figure 2.4.9 shows the radius the the droplet calculated from numerical solution and approximated radius using (2.4.35). As expected, the approximated radius is slightly smaller than the numerical one. The relative error, depicted by the red line in Figure 2.4.9, decreases with the volume of the droplet.

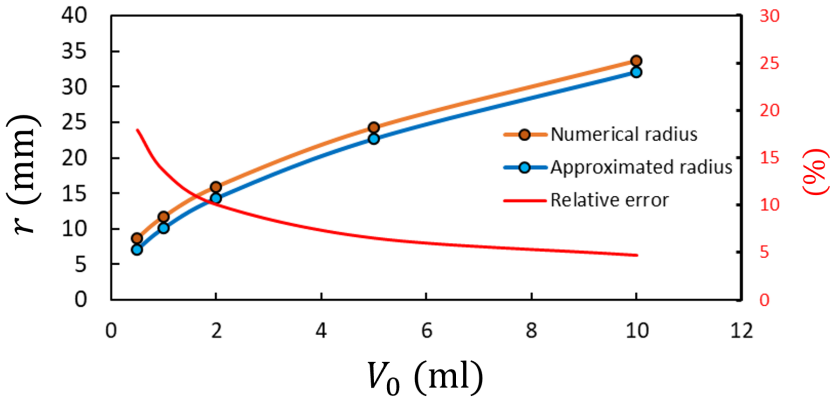

Figure 2.4.9: Comparison of the droplet radius with numerical and asymptotic values.

To find the shape of the droplet near the contact line, we introduce a new unknown function $\theta(\lambda)$, which is related to $h(\lambda)$ by

$$h_\lambda = -\tan(\theta). \tag{2.4.36}$$

Here, θ changes from θ_e at the contact line to zero in the far field. Then equation (2.4.31) can be transformed as

$$\left(\frac{l_c}{B}\right)^2 \cos(\theta) = -\frac{(1-h)^2}{2} + \left(\frac{l_c}{B}\right)^2. \tag{2.4.37}$$

Note that $C + \dfrac{1}{2} = \dfrac{1}{2}\dfrac{1}{1-\cos\theta_e} = \left(\dfrac{l_c}{B}\right)^2$, see equation (2.4.32). Solving equation (2.4.37) with respect to $h(\theta)$, we get the thickness of the droplet as a function of θ,

$$1 - h(\theta) = \sqrt{\frac{1-\cos(\theta)}{1-\cos\theta_e}}. \tag{2.4.38}$$

Next, we need to find a relation between λ and θ to obtain the shape of the droplet in the parametric form $h = h(\theta)$ and $\lambda = \lambda(\theta)$. Using the relation of

(2.4.36), we find

$$\begin{aligned} \frac{dh}{d\lambda} &= -\tan(\theta), \\ \frac{dh}{d\theta}\frac{d\theta}{d\lambda} &= -\tan(\theta), \\ \frac{d\lambda}{d\theta} &= \frac{1}{-\tan(\theta)}\frac{dh}{d\theta}, \end{aligned} \tag{2.4.39}$$

Substituting equation (2.4.38) into the above equation, we then get

$$\begin{aligned} \frac{d\lambda}{d\theta} &= \frac{1}{\tan(\theta)}\frac{d(1-h)}{d\theta}, \\ \frac{d\lambda}{d\theta} &= \frac{1}{\tan(\theta)}\frac{1}{\sqrt{1-\cos\theta_e}}\frac{1}{2}\frac{\sin(\theta)}{\sqrt{1-\cos(\theta)}}, \\ d\lambda &= \frac{1}{2\sqrt{1-\cos\theta_e}}\frac{\cos(\theta)}{\sqrt{1-\cos(\theta)}}d\theta, \end{aligned} \tag{2.4.40}$$

where

$$\begin{aligned} \sqrt{2}\sqrt{1-\cos\theta_e} &= 2\sin(\theta_e/2), \\ \frac{\cos(\theta)}{\sqrt{1-\cos(\theta)}} &= \frac{1}{\sqrt{2}}\frac{1}{\sin(\theta/2)} - \sqrt{2}\sin(\theta/2). \end{aligned}$$

So equation (2.4.40) becomes

$$d\lambda = \frac{1}{2\sin(\theta_e/2)}\left(\frac{1}{\sin(\theta/2)} - 2\sin(\theta/2)\right)d(\theta/2),$$

and then using the Table of Integral (Abramowitz et al., 1988),

$$\begin{aligned} d\lambda &= \frac{1}{2\sin(\theta_e/2)}d\left(-\frac{1}{2}\ln\left(\frac{1+\cos(\theta/2)}{1-\cos(\theta/2)}\right) + 2\cos(\theta/2)\right), \\ d\lambda &= \frac{1}{2\sin(\theta_e/2)}d\left(\ln|\tan(\theta/4)| + 2\cos(\theta/2)\right). \end{aligned}$$

The latter equation is integrated,

$$\lambda = \frac{\ln|\tan(\theta/4)| + 2\cos(\theta/2) + C_1}{2\sin(\theta_e/2)}, \tag{2.4.41}$$

where the constant C_1 is determined by the condition $\lambda = 0$ at $\theta = \theta_e$. Then

$$C_1 = -\ln|\tan(\theta_e/4)| - 2\cos(\theta_e/2).$$

Finally, we obtain λ as a function of θ,

$$\lambda = \frac{1}{2\sin(\theta_e/2)}\left(\ln\left|\frac{\tan(\theta/4)}{\tan(\theta_e/4)}\right| + 2\cos(\theta/2) - 2\cos(\theta_e/2)\right). \tag{2.4.42}$$

The shape of the droplet close to the contact line is governed by equations (2.4.38) and (2.4.42). However, we need to convert the parameter on the horizontal axis when comparing the numerical results with the asymptotic solution. To achieve this, we use the relation $\lambda = (1 - \tilde{r})/\varepsilon_0$ to transform the dimensionless radial coordinate to the inner variable λ. The comparison of the numerical and asymptotic solutions is shown in Figure 2.4.10. Here, we set the parameter $\theta_e = 70°$. This figure illustrates that as the droplet volume increases, the numerical results gradually approach the asymptotic line. The asymptotic solution effectively captures the droplet shape when its volume exceeds 1 mL. It is worth noting that the endpoints of the curves differ because they correspond to the inverse values of ε_0 for each droplet volume.

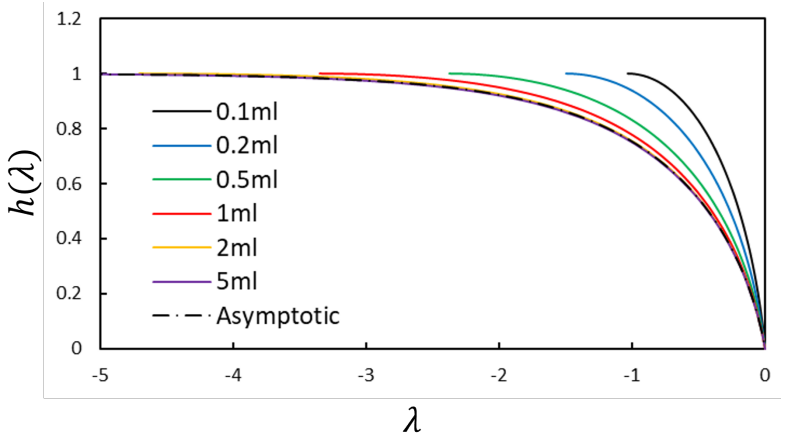

Figure 2.4.10: Comparison of the numerical and asymptotic results in terms of λ.

2.5 Conditions of quasi-static approximation

The time-dependent problem (2.1.1)–(2.1.9) with the certain conditions on the contact line $\Gamma(t)$, which are specific for each model of the contact line motion, should be solved using the initial conditions obtained in section 2.4. This three-dimensional problem is complicated because we should determine the flow inside the droplet caused by deformations of the substrate, the free surface of the droplet, and the position of the contact line. The present study is limited to the problems with small and slow deformations of the substrate. The deformations are so slow that the shape of the free surface and the position of the contact line are governed by the gravity and surface tension at each time instant. This approximation is known as the quasi-static approximation. Then, the flow inside the droplet can be obtained by solving the hydrodynamic part of the problem in the known domain and with certain boundary conditions. The solution within the quasi-static approximation can be considered as the leading order solution with respect to suitable small parameters, which quantifies the

assumption of slow deformations of the substrate.

The quasi-static approximation is justified if the hydrodynamic pressure (2.1.9) on the main part of the free surface can be approximated as the hydrostatic one. Then the dynamic boundary condition (2.1.7) leads to the equation (2.4.2), where now $\eta(x, y, t)$, $B(t)$, and $S(t)$ are the functions of the parameter t. The time t is treated as a parameter here because there are no time derivatives of the unknown function within the quasi-static approximation.

To find the conditions of validity of the quasi-static approximation, we take the radius R_0 of the initial position of the contact line as the length scale and introduce the scale of the deformations of the substrate, Z_{sc}, and the timescale, t_{sc}, of the substrate deformation. The dimensionless variables are denoted by tilde and are introduced as

$$z_p(x, y, t) = Z_{sc}\tilde{z}_p(\tilde{x}, \tilde{y}, \tilde{t}), \quad x = R_0\tilde{x}, \quad y = R_0\tilde{y}, \quad t = t_{sc}\tilde{t}, \quad z = R_0\tilde{z}, \tag{2.5.1}$$

$$\phi(x, y, t) = \left(\frac{Z_{sc}R_0}{t_{sc}}\right)\tilde{\phi}(\tilde{x}, \tilde{y}, \tilde{z}, \tilde{t}), \tag{2.5.2}$$

$$\eta(x, y, t) = B(0)\tilde{\eta}_0(\tilde{r}) + Z_{sc}\tilde{\eta}(\tilde{x}, \tilde{y}, \tilde{t}). \tag{2.5.3}$$

The scaling (2.5.3) implies that the perturbed shape of the droplet is close to the initial shape, $B(0)\tilde{\eta}_0(\tilde{r})$, with the scale of the free surface perturbation being that of the substrate deformation. The scale of the velocity potential follows from the boundary condition (2.1.6) on the substrate surfaces because the flow inside the droplet is forced through this condition. Condition (2.1.6) in the dimensionless variables reads

$$\frac{\partial\tilde{\phi}}{\partial\tilde{z}} = \frac{Z_{sc}}{R_0}\left(\frac{\partial\tilde{\phi}}{\partial\tilde{x}}\frac{\partial\tilde{z}_p}{\partial\tilde{x}} + \frac{\partial\tilde{\phi}}{\partial\tilde{y}}\frac{\partial\tilde{z}_p}{\partial\tilde{y}}\right) + \frac{\partial\tilde{z}_p}{\partial\tilde{t}} \qquad \left(\tilde{z} = \frac{Z_{sc}}{R_0}\tilde{z}_p(\tilde{x}, \tilde{y}, \tilde{t}), \quad (\tilde{x}, \tilde{y}) \in \tilde{S}(\tilde{t})\right). \tag{2.5.4}$$

The assumption of small deformations of the substrate implies that the ratio Z_{sc}/R_0 is small. Then, in the leading order, the condition (2.5.4) can be linearised and imposed on $\tilde{z} = 0$.

The kinematic condition on the free surface of the droplet (2.1.5) together with (2.5.1)-(2.5.3) gives

$$\begin{gathered}\frac{\partial\tilde{\phi}}{\partial\tilde{z}} = \varepsilon_0\tilde{\eta}_0'(\tilde{r})\frac{1}{\tilde{r}}\left(\frac{\partial\tilde{\phi}}{\partial\tilde{x}}\tilde{x} + \frac{\partial\tilde{\phi}}{\partial\tilde{y}}\tilde{y}\right) + \frac{Z_{sc}}{R_0}\left(\frac{\partial\tilde{\phi}}{\partial\tilde{x}}\frac{\partial\tilde{\eta}}{\partial\tilde{x}} + \frac{\partial\tilde{\phi}}{\partial\tilde{y}}\frac{\partial\tilde{\eta}}{\partial\tilde{y}}\right) + \frac{\partial\tilde{\eta}}{\partial\tilde{t}} \\ \left(\tilde{z} = \varepsilon_0\tilde{\eta}_0(\tilde{r}) + \frac{Z_{sc}}{R_0}\tilde{\eta}(\tilde{x}, \tilde{y}, \tilde{t}), \quad (\tilde{x}, \tilde{y}) \in \tilde{S}(\tilde{t})\right).\end{gathered} \tag{2.5.5}$$

Here $\tilde{\eta}_0'(\tilde{r})/\tilde{r}$ is not singular because of the condition (2.4.18). The condition (2.5.5) can be linearised as $Z_{sc}/R_0 \to 0$ similar as it was discussed for the

condition (2.5.4) on the surface of the substrate. Note that ε_0 is assumed to be of order $O(1)$ in our analysis.

On the free surface of the droplet, $\tilde{z} = \varepsilon_0\tilde{\eta}_0(\tilde{r}) + (Z_{sc}/R_0)\tilde{\eta}(\tilde{x},\tilde{y},\tilde{t})$, the hydrostatic component of the pressure (2.1.9) is of the order

$$\rho g\eta(x,y,t) = O(\rho g R_0), \tag{2.5.6}$$

and the dynamic component is of the order

$$-\rho\left(\frac{\partial\phi}{\partial t} + \frac{1}{2}|\nabla\phi|^2\right) = -\frac{\rho Z_{sc}R_0}{t_{sc}^2}\left(\frac{\partial\tilde{\phi}}{\partial\tilde{t}} + \frac{1}{2}\frac{Z_{sc}}{R_0}|\tilde{\nabla}\tilde{\phi}|^2\right) = O\left(\frac{\rho Z_{sc}R_0}{t_{sc}^2}\right). \tag{2.5.7}$$

The dynamic pressure component (2.5.7) is much smaller than the hydrostatic component (2.5.6) if

$$t_{sc} \gg \sqrt{Z_{sc}/g}. \tag{2.5.8}$$

In this case, the dynamic boundary condition (2.1.7) leads to equation (2.4.2), where now the droplet shape function $\eta(x,y,t)$, the function $B(t)$ and the region $S(t)$ depend on the parameter t.

As an example of scales, we consider a droplet of volume 10 mL. We have $R_0 \approx 35$ mm for this droplet, see Figure 2.4.5. Let the scale Z_{sc} of the substrate deformation be 2 mm, then $Z_{sc}/R_0 < 0.057$ and the condition (2.5.8) with $g = 9.8\,\mathrm{m\,s^{-2}}$ provides $t_{sc} \gg 0.014$ s. For the time scale $t_{sc} = 1$ s, which satisfies inequality (2.5.8), the characteristic speed of the substrate deformations is of order of $2\,\mathrm{mm\,s^{-1}}$ and the substrate acceleration, $Z_{sc}/t_{sc}^2 = 2\times10^{-3}\,\mathrm{m\,s^{-2}}$, which is much smaller than the gravitational acceleration g.

Once equation (2.4.2) with the corresponding conditions at the contact line, which depend on the model of the contact line motion, has been solved, the flow inside the droplet is calculated by solving the Neumann problem (2.5.3)–(2.5.5), where $z_p(x,y,t)$, $\eta(x,y,t)$ and $S(t)$ are known from the solution of the quasi-static problem. Next, the dynamic component of the hydrodynamic pressure (2.1.9) can be evaluated and the problem can be formulated for the dynamic correction to the shape of the moving droplet. This latter problem is similar to the quasi-static problem with the equation (2.4.2), but now this equation will contain a forcing term which comes from the dynamic pressure component. This perturbation procedure can be continued and, potentially we can obtain higher-order solutions with respect to the small parameter $Z_{sc}/(gt_{sc}^2)$.

3

Pinned contact line model

We consider a three-dimensional droplet of a given volume resting on a solid substrate, the shape of which varies slowly in time. Initially, the solid surface is assumed to be flat and horizontal, while the droplet shape axisymmetric. The time-dependent shape of the droplet is to be determined employing the quasi-static approximation, see section 2.5, within the pinned contact line model. The shape of the substrate is given at each time instant. In this model, the contact line is not allowed to move with respect to the substrate surface. We consider the contact line to be pinned and assume no hydrophobic behaviours. The projection of the droplet onto the xy-plane does not change in time. The contact angle formed between the free surface and the substrate along the contact line should be determined as part of the solution.

This chapter begins by outlining the formulation of the problem in Cartesian coordinates. To facilitate analysis, we reformulate the problem in dimensionless cylindrical coordinates. Note that the shape of the droplet is three-dimensional for three-dimensional deformations of the substrate. However, the projection of the three-dimensional contact line onto the xy-plane is still circular as for the initial axisymmetric shape of the droplet at any time instant.

The quasi-static problem formulated in the cylindrical coordinates is solved using the asymptotic method, assuming deformations of the substrate are small compared with the vertical dimension of the droplet. Using the perturbation method, the leading order three-dimensional correction of the droplet shape is determined. We obtain that the first-order correction of the free surface of the droplet is described by a Dirichlet boundary value problem for a second-order partial differential equation with variable coefficients in a circle. The boundary value problem is reduced through Fourier decomposition to an infinite number of ordinary differential equations for the functions of the radial coordinate in the Fourier series. Note that time plays a role of a parameter in the quasi-static approximation. The second-order ordinary differential equations with variable coefficients for the functions of the radial coordinate in the Fourier series are solved independently, subject to certain boundary conditions at the contact line. Coefficients in the ordinary differential equations are singular, which makes a direct numerical solution of these equations problematic. To avoid

these difficulties, the boundary value problem for the ordinary differential equations is solved using the Frobenius method close to the centre of the droplet, where the coefficients are singular and numerically close to the contact line. Then, the series and numerical solutions are matched at the patching point. Numerical examples of the three-dimensional droplet shape are shown for a substrate which is slowly inclined but stays flat.

3.1 Formulation of the quasi-static problem for pinned contact line.

For given deformation of the substrate, $z = z_p(x, y, t)$, the shape of the droplet is governed by the equation

$$-\gamma\nabla_2 \cdot \left(\frac{\nabla_2 \eta}{\sqrt{1 + (\nabla_2 \eta)^2}} \right) = \rho g[B(t) - \eta(x, y, t)] \qquad ((x, y) \in S(0)), \tag{3.1.1}$$

see equation (2.4.2), subject to the boundary condition,

$$\eta(x, y, t) = z_p(x, y, t) \qquad ((x, y) \in \partial S(0)). \tag{3.1.2}$$

The projection of the contact line, $\partial S(0)$, onto the xy-plane does not vary in time within the model of the pinned contact line. We are looking for a smooth solution to the problem (3.1.1)–(3.1.2) with finite curvature, which is with finite second-order derivatives η_{xx}, η_{yy}, and η_{xy}.

The initial axisymmetric shape, $z = \bar{\eta}_0(r)$, of the droplet with given volume V_0 was obtained in section 2.4.2 by numerical methods together with the radius of the contact line R_0 and the vertical scale of the droplet $B(0)$. This shape was obtained for the flat and horizontal substrate, $z_p(x, y, 0) = 0$. Therefore, we have

$$\partial S(0) = \{x, y \mid x^2 + y^2 = R_0^2\}, \tag{3.1.3}$$

within the model with a pinned contact line.

The droplet shape for any substrate shape should be defined in the circle $x^2 + y^2 < R_0^2$. Therefore, it is convenient to reformulate the problem (3.1.1)–(3.1.2) in the cylindrical coordinates (r, φ, z), where $x = r\cos\varphi$, $y = r\sin\varphi$. We introduce

$$\begin{aligned} z_p(x, y, t) =& z_p(r\cos\varphi, r\sin\varphi, t) = \bar{z}_p(r, \varphi, t), \\ \eta(x, y, t) =& \eta(r\cos\varphi, r\sin\varphi, t) = \bar{\eta}(r, \varphi, t), \end{aligned} \tag{3.1.4}$$

and reformulate the problem (3.1.1)–(3.1.2) with respect to the function $\bar{\eta}(r, \varphi, t)$. While most terms in the governing equation undergo a

straightforward transformation, our focus will be on the term $\nabla_2 \cdot \left(\dfrac{\nabla_2 \eta}{\sqrt{1+(\nabla_2 \eta)^2}} \right)$. We notice that this term can be expressed as $\nabla_2 \cdot (\phi \mathbf{v})$, where $\phi = \left(1+(\nabla_2 \eta)^2\right)^{-1/2}$ and $\mathbf{v} = \nabla \eta$. By applying the vector identity, we obtain

$$\begin{aligned} \nabla_2 \cdot (\phi \mathbf{v}) &= \phi \nabla_2 \cdot \mathbf{v} + \mathbf{v} \cdot \nabla_2 \phi, \\ &= \phi \nabla_2^2 \eta(x,y) + \nabla_2 \eta(x,y) \cdot \nabla_2 \phi. \end{aligned} \tag{3.1.5}$$

The transformations for each term are listed below:

$$\begin{aligned} \nabla_2 \eta =& \bar{\eta}_r \hat{\mathbf{e}}_\mathbf{r} + \frac{1}{r} \bar{\eta}_\varphi \hat{\mathbf{e}}_\varphi, \\ \phi =& \left(1 + \bar{\eta}_r^2 + \frac{1}{r^2} \bar{\eta}_\varphi^2\right)^{-1/2}, \\ \nabla_2 \phi =& -\phi^3 \left(\bar{\eta}_r \bar{\eta}_{rr} - \frac{1}{r^3} \bar{\eta}_\varphi^2 + \frac{1}{r^2} \bar{\eta}_\varphi \bar{\eta}_{r\varphi} \right) \hat{\mathbf{e}}_\mathbf{r} - \phi^3 \left(\frac{1}{r} \bar{\eta}_r \bar{\eta}_{r\varphi} + \frac{1}{r^3} \bar{\eta}_\varphi \bar{\eta}_{\varphi\varphi} \right) \hat{\mathbf{e}}_\varphi, \\ \nabla_2^2 \eta =& \bar{\eta}_{rr} + \frac{1}{r} \bar{\eta}_r + \frac{1}{r^2} \bar{\eta}_{\varphi\varphi}, \end{aligned}$$

where the unit vector $\hat{\mathbf{e}}_\mathbf{r}$ points in the direction of increasing r with φ fixed, and the unit vector $\hat{\mathbf{e}}_\varphi$ points in the direction of increasing φ with r fixed. Then,

$$\begin{aligned} \nabla_2 \cdot (\phi \mathbf{v}) =& \phi \nabla_2^2 \eta(x,y) + \nabla_2 \eta(x,y) \cdot \nabla_2 \phi, \\ =& \phi^3 \left(\bar{\eta}_{rr} + \frac{1}{r} \bar{\eta}_r + \frac{1}{r^2} \bar{\eta}_{\varphi\varphi} \right) \left(1 + \bar{\eta}_r^2 + \frac{1}{r^2} \bar{\eta}_\varphi^2 \right) \\ & - \phi^3 \left(\bar{\eta}_r \bar{\eta}_{rr} - \frac{1}{r^3} \bar{\eta}_\varphi^2 + \frac{1}{r^2} \bar{\eta}_\varphi \bar{\eta}_{r\varphi} \right) \bar{\eta}_r - \phi^3 \left(\frac{1}{r} \bar{\eta}_r \bar{\eta}_{r\varphi} + \frac{1}{r^3} \bar{\eta}_\varphi \bar{\eta}_{\varphi\varphi} \right) \frac{1}{r} \bar{\eta}_\varphi, \\ =& \phi^3 \left(\bar{\eta}_{rr} + \frac{\bar{\eta}_r}{r} + \frac{\bar{\eta}_{\varphi\varphi}}{r^2} + \frac{\bar{\eta}_r^3}{r} + \frac{\bar{\eta}_r^2 \bar{\eta}_{\varphi\varphi} + \bar{\eta}_\varphi^2 \bar{\eta}_{rr} - 2\bar{\eta}_\varphi \bar{\eta}_r \bar{\eta}_{r\varphi}}{r^2} + \frac{2\bar{\eta}_\varphi^2 \bar{\eta}_r}{r^3} \right). \end{aligned} \tag{3.1.6}$$

Hence, the governing equation (3.1.1) in the polar coordinates reads

$$\begin{aligned} -\gamma \left(1 + \bar{\eta}_r^2 + \frac{\bar{\eta}_\varphi^2}{r^2}\right)^{-\frac{3}{2}} & \left(\bar{\eta}_{rr} + \frac{\bar{\eta}_r}{r} + \frac{\bar{\eta}_{\varphi\varphi}}{r^2} + \frac{\bar{\eta}_r^3}{r} + \frac{\bar{\eta}_r^2 \bar{\eta}_{\varphi\varphi} + \bar{\eta}_\varphi^2 \bar{\eta}_{rr}}{r^2} + \frac{2\bar{\eta}_\varphi^2 \bar{\eta}_r}{r^3} - \frac{2\bar{\eta}_\varphi \bar{\eta}_r \bar{\eta}_{r\varphi}}{r^2} \right) \\ & = \rho g [B(t) - \bar{\eta}(r,\varphi,t)] \qquad (r < R_0). \end{aligned} \tag{3.1.7}$$

The boundary condition on the contact line (3.1.2) becomes

$$\bar{\eta}(r,\varphi,t) = \bar{z}_p(r,\varphi,t) \qquad (r = R_0, \quad -\pi < \varphi < \pi). \tag{3.1.8}$$

The equation (2.2.5) for the contact angle $\theta_c(\varphi,t)$ at the contact line $r = R_0$

takes form in the polar coordinates,

$$\cos\theta_c(\varphi,t)=\frac{1+\bar{\eta}_r\bar{z}_{pr}+\frac{1}{r^2}\bar{\eta}_\varphi\bar{z}_{p\varphi}}{\sqrt{1+\bar{\eta}_r^2+\frac{1}{r^2}\bar{\eta}_\varphi^2}\sqrt{1+\bar{z}_{pr}^2+\frac{1}{r^2}\bar{z}_{p\varphi}^2}}\qquad(r=R_0,\quad -\pi<\varphi<\pi). \tag{3.1.9}$$

The condition (2.1.1) of the constant volume of the droplet reads in the polar coordinates,

$$V_0=\int_{-\pi}^{\pi}\left(\int_0^{R_0}[\bar{\eta}(r,\varphi,t)-\bar{z}_p(r,\varphi,t)]rdr\right)d\varphi, \tag{3.1.10}$$

so equation (2.4.4) takes the form

$$\begin{aligned}-\gamma\int_{-\pi}^{\pi}&\frac{\nabla_2\bar{\eta}(R_0)\cdot\mathbf{n_2}}{\sqrt{1+(\nabla_2\bar{\eta}(R_0))^2}}R_0d\varphi\\&=\rho g\left(B(t)\int_{-\pi}^{\pi}\int_0^{R_0}rdrd\varphi-V_0-\int_{-\pi}^{\pi}\int_0^{R_0}\bar{z}_p(r,\varphi,t)rdrd\varphi\right),\end{aligned} \tag{3.1.11}$$

where $\mathbf{n_2}$ is the outward normal vector to the projection of the contact line $\partial S(0)$ in the plane $z=0$.

The radius R_0 of the initial axisymmetric shape of the droplet is taken as the scale of the radial coordinate, and the unknown function $B(t)$ is taken as the scale of the free surface elevation. Additionally, we define Z_{sc} as the maximum displacement of the solid substrate in the domain $S(0)$ during the time of the process. Dimensionless variables are denoted by a tilde,

$$\begin{aligned}r&=R_0\tilde{r},\\ \bar{\eta}(r,\varphi,t)&=B(t)\tilde{\eta}(\tilde{r},\varphi,t),\\ \bar{z}_p(r,\varphi,t)&=Z_{sc}\tilde{z}_p(\tilde{r},\varphi,t).\end{aligned} \tag{3.1.12}$$

Substituting (3.1.12) into the governing equation (3.1.7) and multiplying both sides by $-R_0^2/\gamma$, we get

$$\frac{a_2+\varepsilon^2a_3}{(1+\varepsilon^2a_1)^{3/2}}=Bo[\tilde{\eta}(\tilde{r},\varphi,t)-1]\qquad(\tilde{r}<1,\quad -\pi<\varphi<\pi), \tag{3.1.13}$$

where $Bo=\rho gR_0^2/\gamma$ is the Bond number, $\varepsilon=B(t)/R_0$ is the aspect ratio, and

$$\begin{aligned}a_1=&\tilde{\eta}_{\tilde{r}}^2+\frac{1}{\tilde{r}^2}\tilde{\eta}_\varphi^2,\\ a_2=&\tilde{\eta}_{\tilde{r}\tilde{r}}+\frac{1}{\tilde{r}}\tilde{\eta}_{\tilde{r}}+\frac{1}{\tilde{r}^2}\tilde{\eta}_{\varphi\varphi},\\ a_3=&\frac{1}{\tilde{r}}\tilde{\eta}_{\tilde{r}}^3+\frac{1}{\tilde{r}^2}\tilde{\eta}_{\tilde{r}}^2\tilde{\eta}_{\varphi\varphi}+\frac{1}{\tilde{r}^2}\tilde{\eta}_\varphi^2\tilde{\eta}_{\tilde{r}\tilde{r}}+\frac{2}{\tilde{r}^3}\tilde{\eta}_\varphi^2\tilde{\eta}_{\tilde{r}}-\frac{2}{\tilde{r}^2}\tilde{\eta}_\varphi\tilde{\eta}_{\tilde{r}}\tilde{\eta}_{\tilde{r}\varphi}.\end{aligned} \tag{3.1.14}$$

The boundary condition on the contact line (3.1.8) gives

$$\tilde{\eta}(1,\varphi,t) = \delta\tilde{z}_p(1,\varphi,t), \tag{3.1.15}$$

where $\delta = Z_{sc}/B(t)$. The contact angle $\theta_c(\varphi,t)$ in the dimensionless polar coordinates is written as

$$\cos\theta_c = \frac{1+\varepsilon\varepsilon_z\left(\tilde{\eta}_{\tilde{r}}\tilde{z}_{p\tilde{r}} + \frac{1}{\tilde{r}^2}\tilde{\eta}_\varphi\tilde{z}_{p\varphi}\right)}{\sqrt{1+\varepsilon^2\left(\tilde{\eta}_{\tilde{r}}^2 + \frac{\tilde{\eta}_\varphi^2}{\tilde{r}^2}\right)}\sqrt{1+\varepsilon_z^2\left(\tilde{z}_{p\tilde{r}}^2 + \frac{\tilde{z}_{p\varphi}^2}{\tilde{r}^2}\right)}} \qquad (\tilde{r}=1, \quad -\pi<\varphi<\pi), \tag{3.1.16}$$

where $\varepsilon_z = \delta\varepsilon$. The condition (3.1.11) in dimensionless variables reads

$$-\frac{1}{Bo}\int_{-\pi}^{\pi}\frac{\varepsilon\tilde{\eta}_{\tilde{r}}(1)}{\sqrt{1+\varepsilon^2\left[\tilde{\eta}_{\tilde{r}}^2(1) + \frac{\tilde{\eta}_\varphi^2(1)}{\tilde{r}^2}\right]}}d\varphi = \varepsilon\left(\pi - \delta\int_{-\pi}^{\pi}\int_0^1 \tilde{z}_p(\tilde{r},\varphi)\tilde{r}d\tilde{r}d\varphi\right) - \frac{V_0}{R_0^3}. \tag{3.1.17}$$

3.2 Asymptotic solution

An approximate solution of the problem (3.1.13), (3.1.15), (3.1.17) is sought in the case where $\varepsilon(t) = O(1)$ and $\delta \ll 1$ in the form,

$$\begin{aligned} \tilde{\eta}(\tilde{r},\varphi,t) &= \tilde{\eta}_0(\tilde{r}) + \delta F_1(\tilde{r},\varphi) + O(\delta^2), \\ \varepsilon &= \varepsilon_0 + \delta\varepsilon_1 + O(\delta^2), \\ \theta_c(\varphi) &= \theta_e + \delta V(\varphi) + O(\delta^2), \end{aligned} \tag{3.2.1}$$

where $\varepsilon_0 = B(0)/R_0$ was calculated numerically in section 2.4.2 see formula (2.4.19). The scales of the functions a_1 and a_2 like $[\tilde{r}]^{-2}$, while the scales of a_3 behave as $[\tilde{r}]^{-3}$. Hence, as $\tilde{r}\to 0$, the asymptotic expansions break. To address this issue, the boundary condition of $\tilde{\eta}_{\tilde{r}} = 0$ shall be satisfied such that $a_3 \sim 0$ as $\tilde{r}\to 0$. Please note that we are considering a small perturbation on the contact line, focusing on the puddle droplet, which has a large volume and contact radius. As the quasi-static approximation is applied in the present study, the parameter t will not be shown in the following equations. Then the asymptotic expansion of the right-hand side of (3.1.13) is $Bo(\tilde{\eta}_0 - 1) + \delta BoF_1 + O(\delta^2)$. The expansions of $(1+\varepsilon^2 a_1)^{-3/2}$ is expressed as

$$(1+\varepsilon^2 a_1)^{-3/2} = \left(1+\varepsilon_0^2\tilde{\eta}_{0,\tilde{r}}^2\right)^{-3/2} - 3\delta\frac{\varepsilon_0^2\tilde{\eta}_{0,\tilde{r}}F_{1,\tilde{r}} + \varepsilon_0\varepsilon_1\tilde{\eta}_{0,\tilde{r}}^2}{(1+\varepsilon_0^2\tilde{\eta}_{0,\tilde{r}}^2)^{5/2}} + O(\delta^2). \tag{3.2.2}$$

The expansions of a_2 and $\varepsilon^2 a_3$ are given by

$$\begin{aligned} a_2 =& \tilde{\eta}_{0,\tilde{r}\tilde{r}} + \frac{\tilde{\eta}_{0,\tilde{r}}}{\tilde{r}} + \delta\left(F_{1,\tilde{r}\tilde{r}} + \frac{F_{1,\tilde{r}}}{\tilde{r}} + \frac{F_{1,\varphi\varphi}}{\tilde{r}^2}\right) + O(\delta^2), \\ \varepsilon^2 a_3 =& \frac{1}{\tilde{r}}\varepsilon_0^2\tilde{\eta}_{0,\tilde{r}}^3 + \delta\varepsilon_0^2\tilde{\eta}_{0,\tilde{r}}^2\left(3\frac{F_{1,\tilde{r}}}{\tilde{r}} + \frac{F_{1,\varphi\varphi}}{\tilde{r}^2}\right) + \frac{2\varepsilon_0\varepsilon_1}{\tilde{r}}\tilde{\eta}_{0,\tilde{r}}^3 + O(\delta^2), \end{aligned}$$

so we have

$$\begin{aligned} a_2+\varepsilon^2 a_3 =& \tilde{\eta}_{0,\tilde{r}\tilde{r}} + \frac{1}{\tilde{r}}\tilde{\eta}_{0,\tilde{r}} + \frac{1}{\tilde{r}}\varepsilon_0^2\tilde{\eta}_{0,\tilde{r}}^3 \\ &+ \delta\left(F_{1,\tilde{r}\tilde{r}} + (1+3\varepsilon_0^2\tilde{\eta}_{0,\tilde{r}}^2)\frac{F_{1,\tilde{r}}}{\tilde{r}} + (1+\varepsilon_0^2\tilde{\eta}_{0,\tilde{r}}^2)\frac{F_{1,\varphi\varphi}}{\tilde{r}^2} + \frac{2\varepsilon_0\tilde{\eta}_{0,\tilde{r}}^3}{\tilde{r}}\varepsilon_1\right) + O(\delta^2). \end{aligned} \tag{3.2.3}$$

Therefore, the governing equation (3.1.13) in the leading order as $\delta \to 0$ provides

$$(1+\varepsilon_0^2\tilde{\eta}_{0,\tilde{r}}^2)^{-3/2}\left(\tilde{\eta}_{0,\tilde{r}\tilde{r}} + (1+\varepsilon_0^2\tilde{\eta}_{0,\tilde{r}}^2)\frac{\tilde{\eta}_{0,\tilde{r}}}{\tilde{r}}\right) = Bo(\tilde{\eta}_0 - 1) \qquad (\tilde{r}<1). \tag{3.2.4}$$

This equation, together with the boundary conditions $\eta_0(1,\varphi,0) = 0$, see (3.1.15), $\theta_c(\varphi,0) = \theta_e$, see (3.1.16), and the condition of the constant volume of the droplet, see (3.1.17), describes the initial axisymmetric shape of the droplet for flat horizontal substrate, $\delta = 0$. This problem was solved numerically in section 2.4.

Substituting asymptotic expansions (3.2.2) and (3.2.3) as $\delta \to 0$, see above, into equation (3.1.13) and collecting terms of order $O(\delta)$, we obtain the following equation for the first-order correction of the droplet shape,

$$\begin{aligned} &(1+\varepsilon_0^2\tilde{\eta}_{0,\tilde{r}}^2)^{-3/2}\left(F_{1,\tilde{r}\tilde{r}} + (1+3\varepsilon_0^2\tilde{\eta}_{0,\tilde{r}}^2)\frac{F_{1,\tilde{r}}}{\tilde{r}} + (1+\varepsilon_0^2\tilde{\eta}_{0,\tilde{r}}^2)\frac{F_{1,\varphi\varphi}}{\tilde{r}^2} + \frac{2\varepsilon_0\tilde{\eta}_{0,\tilde{r}}^3}{\tilde{r}}\varepsilon_1\right) \\ &\quad - 3\frac{\varepsilon_0^2\tilde{\eta}_{0,\tilde{r}}F_{1,\tilde{r}} + \varepsilon_0\varepsilon_1\tilde{\eta}_{0,\tilde{r}}^2}{(1+\varepsilon_0^2\tilde{\eta}_{0,\tilde{r}}^2)^{5/2}}\left(\tilde{\eta}_{0,\tilde{r}\tilde{r}} + (1+\varepsilon_0^2\tilde{\eta}_{0,\tilde{r}}^2)\frac{\tilde{\eta}_{0,\tilde{r}}}{\tilde{r}}\right) = BoF_1 \qquad (\tilde{r}<1). \end{aligned}$$

Using equation (3.2.4), the above equation is rearranged as

$$H_1(\tilde{r})F_{1,\tilde{r}\tilde{r}} + H_2(\tilde{r})\frac{F_{1,\tilde{r}}}{\tilde{r}} + H_3(\tilde{r})\frac{F_{1,\varphi\varphi}}{\tilde{r}^2} + H_4(\tilde{r})\varepsilon_1 = BoF_1 \qquad (\tilde{r}<1), \tag{3.2.5}$$

where

$$
\begin{aligned}
H_1(\tilde{r}) &= \left(1+\varepsilon_0^2\tilde{\eta}_{0,\tilde{r}}^2\right)^{-3/2},\\
H_2(\tilde{r}) &= \frac{1+3\varepsilon_0^2\tilde{\eta}_{0,\tilde{r}}^2}{(1+\varepsilon_0^2\tilde{\eta}_{0,\tilde{r}}^2)^{3/2}} - 3\varepsilon_0^2\tilde{\eta}_{0,\tilde{r}}\frac{Bo(\tilde{\eta}_0-1)}{1+\varepsilon_0^2\tilde{\eta}_{0,\tilde{r}}^2}\tilde{r},\\
H_3(\tilde{r}) &= \frac{1}{\sqrt{1+\varepsilon_0^2\tilde{\eta}_{0,\tilde{r}}^2}},\\
H_4(\tilde{r}) &= \frac{2\varepsilon_0\tilde{\eta}_{0,\tilde{r}}^3}{\tilde{r}(1+\varepsilon_0^2\tilde{\eta}_{0,\tilde{r}}^2)^{3/2}} - 3\varepsilon_0\tilde{\eta}_{0,\tilde{r}}^2\frac{Bo(\tilde{\eta}_0-1)}{1+\varepsilon_0^2\tilde{\eta}_{0,\tilde{r}}^2}.
\end{aligned}
\tag{3.2.6}
$$

The functions (3.2.6) depend on the solution $\tilde{\eta}_0(\tilde{r})$, constant ε_0, and the Bond number obtained in section 2.4. As an example, for the volume of droplet 0.1 mL, and $\theta_e = 70°$, the functions $H_1(\tilde{r})$, $H_2(\tilde{r})$, $H_3(\tilde{r})$, and $H_4(\tilde{r})$ are depicted in Figure 3.2.1. Here $Bo = 2.90$ and $\varepsilon_0 = 0.97$ for these values of the parameters.

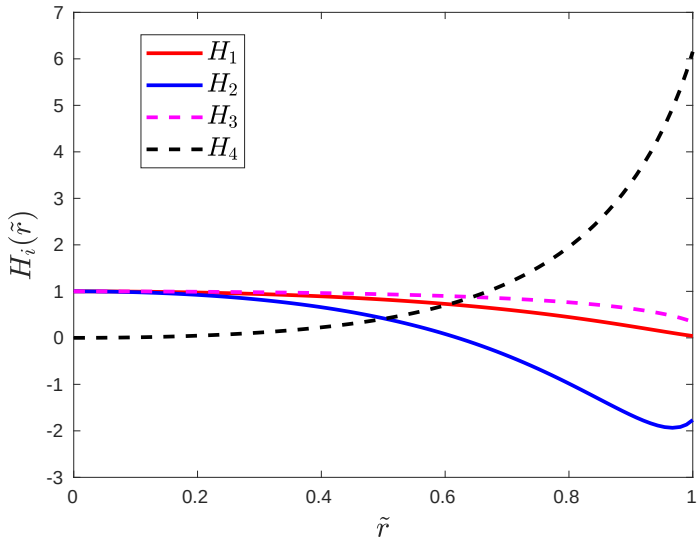

Figure 3.2.1: The functions $H_i(\tilde{r})$, $i = 1, 2, 3, 4$, for $V_0 = 0.1$ mL.

Substituting the expansions (3.2.1) into (3.1.15)–(3.1.17), we have

$$
\tilde{\eta}_0(1) + \delta F_1(1,\varphi) = \delta\tilde{z}_p(1,\varphi) + O(\delta^2), \tag{3.2.7}
$$

$$
\begin{aligned}
\cos\theta_e - \delta\sin\theta_e V(\varphi) =& \frac{1}{\sqrt{1+\varepsilon_0^2\tilde{\eta}_{0,\tilde{r}}^2(1)}} + \delta\frac{\varepsilon_0^2\tilde{\eta}_{0,\tilde{r}}(1)\tilde{z}_{p,\tilde{r}}(1,\varphi)}{\sqrt{1+\varepsilon_0^2\tilde{\eta}_{0,\tilde{r}}^2(1)}}\\
&- \delta\frac{\varepsilon_0\tilde{\eta}_{0,\tilde{r}}^2(1)\varepsilon_1 + \varepsilon_0^2\tilde{\eta}_{0,\tilde{r}}(1)F_{1,\tilde{r}}(1,\varphi)}{\left(1+\varepsilon_0^2\tilde{\eta}_{0,\tilde{r}}^2(1)\right)^{3/2}} + O(\delta^2),
\end{aligned}
\tag{3.2.8}
$$

$$
\begin{aligned}
&-\frac{1}{Bo}\left(\int_{-\pi}^{\pi}\frac{\varepsilon_0\tilde{\eta}_{0,\tilde{r}}(1)}{\sqrt{1+\varepsilon_0^2\tilde{\eta}_{0,\tilde{r}}^2(1)}}d\varphi+\delta\int_{-\pi}^{\pi}\frac{\varepsilon_0 F_{1,\tilde{r}}(1,\varphi)+\tilde{\eta}_{0,\tilde{r}}(1)\varepsilon_1}{\left(1+\varepsilon_0^2\tilde{\eta}_{0,\tilde{r}}^2(1)\right)^{3/2}}d\varphi\right)\\
&=\pi\varepsilon_0-\frac{V_0}{R_0^3}+\delta\left(\pi\varepsilon_1-\varepsilon_0\int_{-\pi}^{\pi}\int_0^1\tilde{z}_p(\tilde{r},\varphi)\tilde{r}d\tilde{r}d\varphi\right)+O(\delta^2). \qquad (3.2.9)
\end{aligned}
$$

Using $\tilde{\eta}_{0,\tilde{r}}(1)=-\tan\theta_e/\varepsilon_0$, see equation (2.4.17), and collecting terms of order $O(\delta)$ from (3.2.7)–(3.2.9), we obtain the boundary condition for equation (3.2.5),

$$F_1(1,\varphi)=\tilde{z}_p(1,\varphi), \qquad (3.2.10)$$

and the equation for ε_1,

$$\frac{2\pi\sin\theta_e\cos^2\theta_e}{Bo\varepsilon_0}\varepsilon_1-\frac{\varepsilon_0\cos^3\theta_e}{Bo}\int_{-\pi}^{\pi}F_{1,\tilde{r}}(1,\varphi)d\varphi=\pi\varepsilon_1-\varepsilon_0\int_{-\pi}^{\pi}\int_0^1\tilde{z}_p(\tilde{r},\varphi)\tilde{r}d\tilde{r}d\varphi. \qquad (3.2.11)$$

Equation (3.2.8) leads to the following formula for the first-order correction of the contact angle,

$$V(\varphi)=\sin\theta_e\cos\theta_e\frac{\varepsilon_1}{\varepsilon_0}-\varepsilon_0\cos^2\theta_e F_{1,\tilde{r}}(1,\varphi)+\varepsilon_0\tilde{z}_{p,\tilde{r}}(1,\varphi). \qquad (3.2.12)$$

The governing equation for the first-order correction of the droplet free surface (3.2.5) is a second-order linear partial differential equation with singular variable coefficients, which should be solved together with the Dirichlet condition (3.2.10) and equation (3.2.11). Next, the first-order correction of the contact angle, $V(\varphi)$, is evaluated using (3.2.12). The function $F_1(\tilde{r},\varphi)$ is sought in the form of Fourier series,

$$F_1(\tilde{r},\varphi)=\alpha_0(\tilde{r})+\sum_{n=1}^{\infty}\left[\alpha_n(\tilde{r})\cos n\varphi+\alpha_n^*(\tilde{r})\sin n\varphi\right], \qquad (3.2.13)$$

with coefficients $\alpha_0(\tilde{r})$, $\alpha_n(\tilde{r})$, $\alpha_n^*(\tilde{r})$, $n=1,2,3,\cdots$, to be determined. Substituting the Fourier series (3.2.13) into equation (3.2.5) and separating the variables, we obtain the following set of ordinary differential equations,

$$H_1(\tilde{r})\alpha_0''+H_2(\tilde{r})\frac{\alpha_0'}{\tilde{r}}-Bo\alpha_0=-H_4(\tilde{r})\varepsilon_1, \qquad (3.2.14)$$

$$H_1(\tilde{r})\alpha_n''+H_2(\tilde{r})\frac{\alpha_n'}{\tilde{r}}-\left[Bo\tilde{r}^2+n^2H_3(\tilde{r})\right]\frac{\alpha_n}{\tilde{r}^2}=0, \qquad (3.2.15)$$

$$H_1(\tilde{r})\alpha_n^{*\prime\prime}+H_2(\tilde{r})\frac{\alpha_n^{*\prime}}{\tilde{r}}-\left[Bo\tilde{r}^2+n^2H_3(\tilde{r})\right]\frac{\alpha_n^*}{\tilde{r}^2}=0. \qquad (3.2.16)$$

Equations (3.2.14)–(3.2.16) are linear second-order ordinary differential equations with singular variable coefficients where $H_i(\tilde{r})$, $i=1,2,3,4$, are given

by equations (3.2.6). Each of the equations (3.2.14)–(3.2.16) requires two boundary conditions. However, in this problem, we have only one condition available for each equation, lacking the required second condition. Nevertheless, there is a restriction on the class of the solutions since we seek the finite curvature of the free surface of the droplet, which could be the required second condition for each of the equations (3.2.14)–(3.2.16).

The Fourier series (3.2.13) and the boundary condition (3.2.10) provide the corresponding boundary conditions for equations (3.2.14)–(3.2.16),

$$\begin{aligned}\alpha_0(1) =&\frac{1}{2\pi}\int_{-\pi}^{\pi}\tilde{z}_p(1,\varphi)d\varphi,\\ \alpha_n(1) =&\frac{1}{\pi}\int_{-\pi}^{\pi}\tilde{z}_p(1,\varphi)\cos(n\varphi)d\varphi,\\ \alpha_n^*(1) =&\frac{1}{\pi}\int_{-\pi}^{\pi}\tilde{z}_p(1,\varphi)\sin(n\varphi)d\varphi.\end{aligned} \tag{3.2.17}$$

Equation (3.2.11) provides

$$\varepsilon_1 = k_1\alpha_0^{'}(1) + k_3, \tag{3.2.18}$$

where k_1 and k_3 are known constants,

$$\begin{aligned}k_1 =&\frac{2\varepsilon_0^2\cos^3\theta_e}{2\sin\theta_e\cos^2\theta_e - Bo\varepsilon_0},\\ k_3 =&-\frac{Bo\varepsilon_0^2}{\pi(2\sin\theta_e\cos^2\theta_e - Bo\varepsilon_0)}\int_{-\pi}^{\pi}\int_0^1\tilde{z}_p(\tilde{r},\varphi)\tilde{r}d\tilde{r}d\varphi,\end{aligned} \tag{3.2.19}$$

and $\alpha_0^{'}(1)$ is to determined. The first-order correction of the contact angle reads, see equation (3.2.12),

$$\begin{aligned}V(\varphi) =&\varepsilon_0\tilde{z}_{p,\tilde{r}}(1,\varphi) + \sin\theta_e\cos\theta_e\frac{\varepsilon_1}{\varepsilon_0}\\ &-\varepsilon_0\cos^2\theta_e\left(\alpha_0^{'}(1) + \sum_{n=1}^{\infty}\left[\alpha_n^{'}(1)\cos n\varphi + \alpha_n^{*'}(1)\sin n\varphi\right]\right),\end{aligned} \tag{3.2.20}$$

where $\alpha_n^{'}(1)$ and $\alpha_n^{*'}(1)$, $n \geq 1$, should be determined as part of the solution.

In this section, we employed the perturbation method to derive the equations for the first-order correction of the droplet shape (3.2.14)–(3.2.16) subjected to the boundary conditions (3.2.17), equation (3.2.18) and the condition that the solutions are bounded together with their first and second derivatives where $0 \leq \tilde{r} \leq 1$.

3.3 Combined solution

The condition of regularity of the solutions makes the problem for equations (3.2.14)–(3.2.16) difficult to solve by numerical means only. We solve the problems by combining regular series solutions for small $\tilde{r}$, $0 \leq \tilde{r} < a$, and numerical solutions on the intervals $a < \tilde{r} \leq 1$. The series solutions and the numerical solutions, which satisfy the boundary conditions (3.2.17), are matched smoothly at the patching point $\tilde{r} = a$.

3.3.1 Series solution

In this subsection, we are looking for regular solutions to the governing equations (3.2.14)–(3.2.16) for small $\tilde{r}$. Note that $\tilde{r} = 0$ is the regular singular point for these equations and the functions $H_i(\tilde{r})$ can be approximated for small $\tilde{r}$ by power series

$$H_i(\tilde{r}) = \sum_{l=0}^{\infty} H_{il}\tilde{r}^l = H_{i0} + H_{i1}\tilde{r} + H_{i2}\tilde{r}^2 + \cdots, \tag{3.3.1}$$

where $i = 1, 2, 3, 4$. Here $H_1(0) = H_2(0) = H_3(0) = 1$ and $H_4(0) = 0$, see (3.2.6), which gives $H_{10} = H_{20} = H_{30} = 1$ and $H_{40} = 0$.

The general solution of equation (3.2.14) has the form $\alpha_0(\tilde{r}) = \varepsilon_1\alpha_0^{(p)}(\tilde{r}) + \alpha_0^{(h)}(\tilde{r})$, where $\varepsilon_1\alpha_0^{(p)}(\tilde{r})$ is a particular solution satisfying equation (3.2.14), and $\alpha_0^{(h)}(\tilde{r})$ is the general solution of the corresponding homogeneous equation,

$$H_1(\tilde{r})\alpha_0'' + H_2(\tilde{r})\frac{\alpha_0'}{\tilde{r}} - Bo\alpha_0 = 0. \tag{3.3.2}$$

The general solution of the equation (3.3.2) has the form,

$$\alpha_0^{(h)}(\tilde{r}) = C_0\alpha_0^{(h1)}(\tilde{r}) + \tilde{C}_0\alpha_0^{(h2)}(\tilde{r}), \tag{3.3.3}$$

where C_0 and $\tilde{C}_0$ are arbitrary constants, and $\alpha^{(h1)}(\tilde{r})$ and $\alpha^{(h2)}(\tilde{r})$ are two linearly independent solutions of the homogeneous equation (3.3.2). To find $\alpha^{(h1)}(\tilde{r})$ and $\alpha^{(h2)}(\tilde{r})$, we use the Frobenius method,

$$\alpha_0^{(h1,2)}(\tilde{r}) = \sum_{m=0}^{\infty} k_{m0}\tilde{r}^{m+R}, \tag{3.3.4}$$

where R needs to be determined by the indicial equation. Substituting the series (3.3.1) and (3.3.4) into equation (3.3.2) and collecting the terms of the lowest power, we obtain the indicial equation,

$$R^2 - R + R = 0,$$

which has a double root $R = 0$. Therefore, the linearly independent solutions of

equation (3.3.2) have the form

$$\alpha_0^{(h1)}(\tilde{r}) = \sum_{m=0}^{\infty} k_{m0}\tilde{r}^m, \tag{3.3.5}$$

$$\alpha_0^{(h2)}(\tilde{r}) = \log(\tilde{r})\alpha_0^{(h1)}(\tilde{r}) + \sum_{m=1}^{\infty} \bar{k}_{m0}\tilde{r}^m. \tag{3.3.6}$$

The solution (3.3.6) is singular since $\log(\tilde{r}) \to -\infty$ as $\tilde{r} \to 0$. However, we are searching for regular solutions. Thus, the constant $\tilde{C}_0$ in (3.3.3) should be set to zero. As a result, the regular solution of the homogeneous equation (3.3.2) is represented by

$$\alpha_0^{(h)}(\tilde{r}) = C_0\alpha_0^{(hr)}(\tilde{r}) = C_0 \sum_{m=0}^{\infty} k_{m0}\tilde{r}^m. \tag{3.3.7}$$

It is convenient to introduce a new function,

$$H_0(\tilde{r}) = \sum_{l=0}^{\infty} H_{0l}\tilde{r}^l, \tag{3.3.8}$$

where

$$H_{0l} = \begin{cases} Bo, & l = 2, \\ 0, & l \neq 2. \end{cases}$$

Substituting the series (3.3.1), (3.3.7), (3.3.8) into equation (3.3.2), we obtain

$$\sum_{m=0}^{\infty}\sum_{l=0}^{\infty} \left[m(m-1)H_{1l} + mH_{2l} - H_{0l}\right] k_{m0}\tilde{r}^{m+l-2} = 0.$$

Let $q = m + l$, then the above equation is transformed to

$$\sum_{q=0}^{\infty} \left(\sum_{m=0}^{q} [m(m-1)H_{1(q-m)} + mH_{2(q-m)} - H_{0(q-m)}]k_{m0} \right) \tilde{r}^{q-2} = 0. \tag{3.3.9}$$

The inner summation terms in equation (3.3.9) should be equal to zero, which leads to the recurrence relation for the coefficients k_{m0}, $m \geq 1$,

$$k_{m0} = \begin{cases} 0 & (m = 1), \\ \dfrac{Bo}{4}k_{00} & (m = 2), \\ -\sum_{i=2}^{m-1} \dfrac{i(i-1)H_{1(m-i)} + iH_{2(m-i)} - H_{0(m-i)}}{m^2} k_{i0} & (m \geq 3). \end{cases} \tag{3.3.10}$$

Note that $H_{10} = H_{20} = 1$. Thus, we obtain the regular homogeneous solution,

$$\begin{aligned}\alpha_0^{(h)}(\tilde{r}) =& C_0\alpha_0^{(hr)}(\tilde{r}) = C_0\sum_{m=0}^{\infty} k_{m0}\tilde{r}^m,\\ =& C_0\left(k_{00} + k_{10}\tilde{r} + k_{20}\tilde{r}^2 + k_{30}\tilde{r}^3 + \cdots\right),\\ =& C_0\left(1 + \tilde{k}_{10}\tilde{r} + \tilde{k}_{20}\tilde{r}^2 + \tilde{k}_{30}\tilde{r}^3 + \cdots\right),\end{aligned} \tag{3.3.11}$$

where constant C_0 should be determined and the coefficients $\tilde{k}_{10}$, $\tilde{k}_{20}$, $\tilde{k}_{30}\cdots$ are obtained using the recurrence relation (3.3.10) with $k_{00} = 1$.

$\varepsilon_1\alpha_0^{(p)}(\tilde{r})$ is a particular solution of equation (3.2.14), where $\alpha_0^{(p)}(\tilde{r})$ satisfies the equation

$$H_1(\tilde{r})\alpha_0^{''} + H_2(\tilde{r})\frac{\alpha_0^{'}}{\tilde{r}} - Bo\alpha_0 = -H_4(\tilde{r}). \tag{3.3.12}$$

The solution of equation (3.3.12) is sought in the form,

$$\alpha_0^{(p)}(\tilde{r}) = \sum_{m=0}^{\infty} f_{m0}\tilde{r}^{m+2}. \tag{3.3.13}$$

Substituting the series (3.3.1), (3.3.8), (3.3.13) into (3.3.12), we get the recurrence relation for $q = 0, 1, 2, 3, \cdots$,

$$\sum_{m=0}^{q}[(m+2)(m+1)H_{1(q-m)} + (m+2)H_{2(q-m)} - H_{0(q-m)}]f_{m0} + H_{4q} = 0,$$

which gives

$$f_{m0} = \begin{cases} 0 \qquad (m = 0),\\ -\sum_{i=0}^{m-1}\dfrac{(i+2)(i+1)H_{1(m-i)} + (i+2)H_{2(m-i)} - H_{0(m-i)}}{(m+2)^2}f_{i0}\\ -\dfrac{H_{4m}}{(m+2)^2} \qquad (m \geq 1). \end{cases} \tag{3.3.14}$$

Note that $H_{10} = H_{20} = 1$ and $H_{40} = 0$. Thus, the general solution of equation (3.2.14) reads

$$\begin{aligned}\alpha_0(\tilde{r}) =& C_0\alpha_0^{(hr)}(\tilde{r}) + \varepsilon_1\alpha_0^{(p)}(\tilde{r}),\\ =& C_0\left(1 + \tilde{k}_{10}\tilde{r} + \tilde{k}_{20}\tilde{r}^2 + \tilde{k}_{30}\tilde{r}^3 + \cdots\right)\\ &+ \varepsilon_1\tilde{r}^2\left(f_{00} + f_{10}\tilde{r} + f_{20}\tilde{r}^2 + f_{30}\tilde{r}^3 + \cdots\right).\end{aligned} \tag{3.3.15}$$

where C_0 and ε_1 should be determined, and the coefficients in the round brackets are determined using the recurrence relations (3.3.10) and (3.3.14), correspondingly.

Given that equations (3.2.15) and (3.2.16) are essentially identical ordinary differential equations, we only illustrate the solution procedure for (3.2.15). The solution of equation (3.2.16) can then be obtained by following the same process for equation (3.2.15) with a change in notation.

The general solution of the homogeneous equation (3.2.15) has the form,

$$\alpha_n^{(h)}(\tilde{r}) = C_n \alpha_n^{(h1)}(\tilde{r}) + \tilde{C}_n \alpha_n^{(h2)}(\tilde{r}) \tag{3.3.16}$$

where C_n and $\tilde{C}_n$ are arbitrary constants, and $\alpha^{(h1)}(\tilde{r})$ and $\alpha^{(h2)}(\tilde{r})$ are linearly independent. We again employ the Frobenius method to find the series solution in the form,

$$\alpha_n^{(h1)}(\tilde{r}) = \sum_{m=0}^{\infty} k_{mn} \tilde{r}^{m+R}.$$

In this case, the indicial equation provides $R^2 = n^2$ where $n \geq 1$ and gives the two roots, $R = \pm n$, differing by an integer. Hence, we obtain

$$\begin{aligned} \alpha_n^{(h1)}(\tilde{r}) &= \tilde{r}^n \sum_{m=0}^{\infty} k_{mn} \tilde{r}^m, \\ \alpha_n^{(h2)}(\tilde{r}) &= \bar{D}_n \log(\tilde{r}) \alpha_n^{(h1)}(\tilde{r}) + \tilde{r}^{-n} \sum_{m=0}^{\infty} \bar{k}_{mn} \tilde{r}^m, \end{aligned} \tag{3.3.17}$$

where $\bar{D}_n$ is an arbitrary constant, see Tenenbaum and Pollard (1985) for details. Since $\bar{k}_{0n} \neq 0$ and $\tilde{r}^{-n} \to \infty$ as $\tilde{r} \to 0$, we set the coefficient $\tilde{C}_n$ to zero to eliminate the singularity from the second solution. Thus, the regular general solution of equation (3.2.15) reads

$$\alpha_n^{(h)}(\tilde{r}) = C_n \alpha_n^{(hr)}(\xi) = C_n \sum_{m=0}^{\infty} k_{mn} \tilde{r}^{m+n}. \tag{3.3.18}$$

Substituting (3.3.18) into equation (3.2.15), we obtain the recurrence relation to determine the coefficients k_{mn}, $m \geq 1$,

$$k_{mn} = -\sum_{i=0}^{m-1} \left[\frac{(i+n)(i+n-1)H_{1(m-i)} + (i+n)H_{2(m-i)} - \tilde{H}_{3(m-i)}}{m(m+2n)} \right] k_{in}, \tag{3.3.19}$$

where coefficients $\tilde{H}_{3(m-i)}$ are defined as

$$\tilde{H}_{3(m-i)} = \tilde{H}_{3l} = \begin{cases} n^2 H_{3l} & (l \neq 2), \\ n^2 H_{3l} + Bo & (l = 2). \end{cases} \tag{3.3.20}$$

Hence, the regular solution of the homogeneous equation (3.2.15) reads

$$\begin{aligned}\alpha_n(\tilde{r}) =& C_n \alpha_n^{(hr)}(\tilde{r}) = C_n \sum_{m=0}^{\infty} k_{mn} \tilde{r}^{m+n}, \\ =& C_n \tilde{r}^n \left(k_{0n} + k_{1n}\tilde{r} + k_{2n}\tilde{r}^2 + k_{3n}\tilde{r}^3 + \cdots\right), \\ =& C_n \tilde{r}^n \left(1 + \tilde{k}_{1n}\tilde{r} + \tilde{k}_{2n}\tilde{r}^2 + \tilde{k}_{3n}\tilde{r}^3 + \cdots\right),\end{aligned} \tag{3.3.21}$$

where the constant C_n is to be determined, and the coefficients $\tilde{k}_{1n}$, $\tilde{k}_{2n}$, $\tilde{k}_{3n}\cdots$, are calculated using the recurrence relation (3.3.19) with $k_{0n} = 1$.

The coefficients in the power series of each function $H_i(\tilde{r})$, where $i = 1, 2, 3, 4$, see equation (3.3.1), are required to find the solutions $\alpha_0^{(hr)}(\tilde{r})$, $\alpha_0^{(p)}(\tilde{r})$, and $\alpha_n^{(hr)}(\tilde{r})$. We have $H_{10} = H_{20} = H_{30} = 1$ and $H_{40} = 0$. The coefficients H_{il}, $l \geq 1$, in the series (3.3.1) are determined by applying the polynomial curve fitting. This fitting, which is a regression method, minimises the sum of the square of the residual to find the approximated solution.

For a given initial droplet shape and contact radius, the functions $H_i(\tilde{r})$ are computed using equation (3.2.6). Figure 3.3.1 depicts the third-order and sixth-order polynomial approximations for $V_0 = 0.1\,\mathrm{mL}$, $\rho = 999\,\mathrm{kg\,m^{-3}}$, $g = 9.8\,\mathrm{m\,s^{-2}}$, $\gamma = 72\,\mathrm{mN\,m^{-2}}$, and $\theta_e = 70°$. The circles denote are $H_i(\tilde{r})$, while the solid lines depict the approximating polynomials, $\hat{H}_i(\tilde{r})$. The red dashed lines represent the relative error,

$$Error = \frac{|H_i(\tilde{r}) - \hat{H}_i(\tilde{r})|}{|H_i(\tilde{r})|}. \tag{3.3.22}$$

In most cases, the error increases towards the edge $\tilde{r} = 1$. As the polynomial order increases, the error decreases.

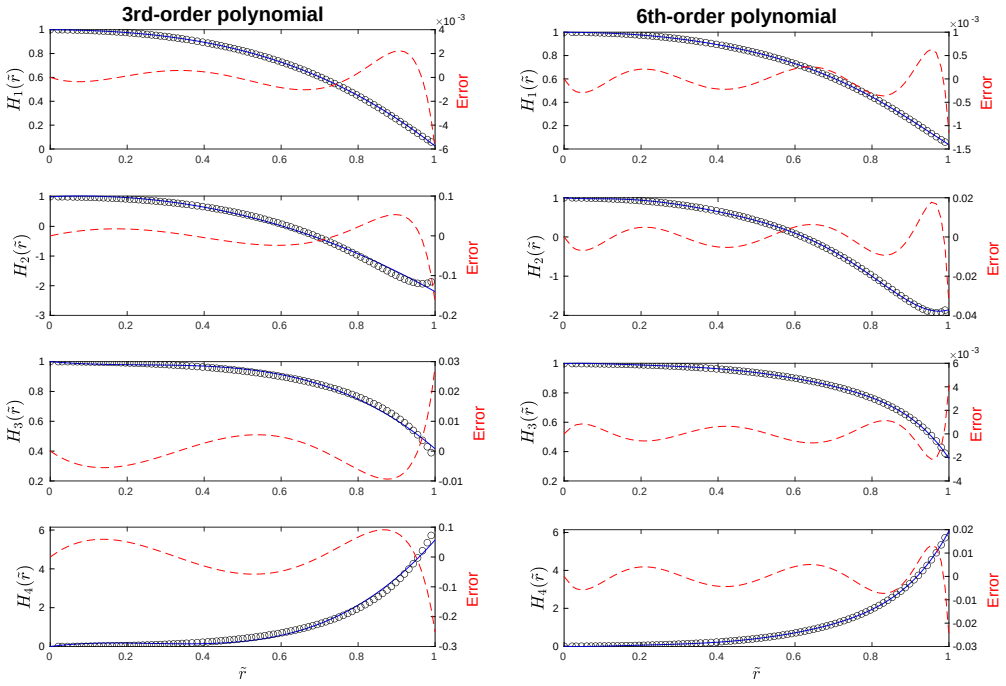

Figure 3.3.1: Polynomial curve fitting to functions $H_i(\tilde{r})$, $i = 1, 2, 3, 4$, within the interval $[0, 1]$. The left column is for the third-order polynomial approximation, and the right column shows the sixth-order approximation.

Subsequently, we consider the approximation in the smaller interval $[0, a]$ where $a \in (0, 1)$. As seen in Figure 3.3.2, we carry out the third-order and sixth-order polynomial curve fitting for the functions $H_i(\tilde{r})$, $i = 1, 2, 3, 4$, within $\tilde{r} \in [0, 0.8]$. Overall, the polynomial approximation in the smaller interval yields more accurate results compared to the entire interval where $\tilde{r} \in [0, 1]$.

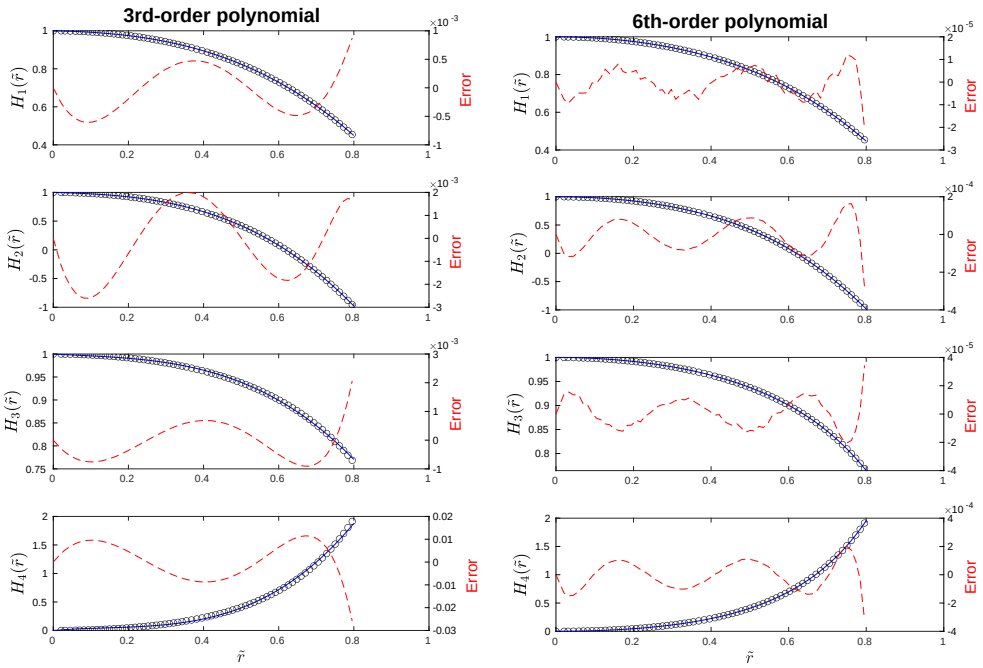

Figure 3.3.2: Polynomial curve fitting to functions $H_i(\tilde{r})$, $i = 1, 2, 3, 4$, within the interval $[0, 0.8]$. The left column is for the third-order polynomial approximation, and the right column shows the sixth-order approximation.

Once the coefficients in series (3.3.1) are calculated, we then compute coefficients $\tilde{k}_{mn}$ and f_{m0}. However, those coefficients grow with m, suggesting that the series solution for the entire interval in each model is not feasible since it diverges. Even though a solution within the interval $[0, 1]$ is not accessible, it can still be used within a smaller interval. The coefficients $\tilde{k}_{m0}$, f_{m0}, $\tilde{k}_{m2}$ increase with m, as illustrated in the upper row of Figure 3.3.3. Meanwhile, the contribution from each power term decreases with m due to $a < 1$, as depicted in the bottom row of Figure 3.3.3.

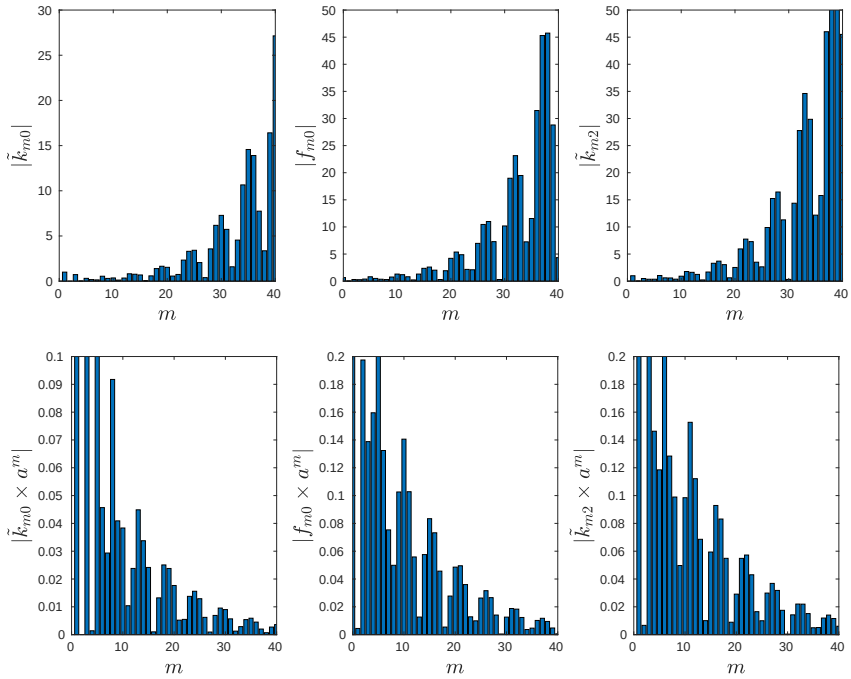

Figure 3.3.3: The coefficients $\tilde{k}_{m0}$, f_{m0}, $\tilde{k}_{m2}$ where $m = 1, 2, 3, \cdots, 40$, in the interval $[0, 0.8]$.

Figure 3.3.4 presents the functions $\alpha_0^{(hr)}(\tilde{r})$, $\alpha_0^{(p)}(\tilde{r})$, $\alpha_n^{(hr)}(\tilde{r})$ within the interval $[0, 0.8]$. To guarantee the convergence of the series solution, we include the additional 100 terms to assess the value of the series solution at any position a. If the discrepancy is less than 10^{-4}, then we consider the value of m to be sufficient. The result in Figure 3.3.4 corresponds to selecting $m = 200$.

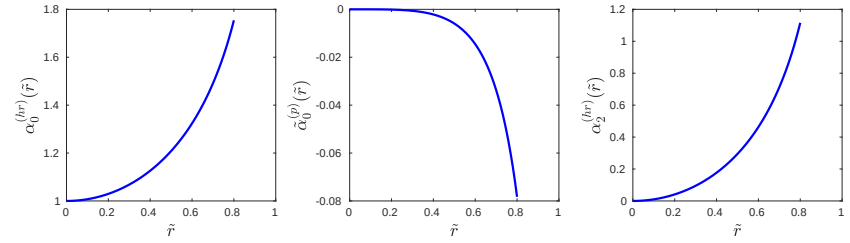

Figure 3.3.4: Series solution valid on $\tilde{r} \in [0, 0.8]$.

The series solutions $\alpha_0^{(hr)}(\tilde{r})$, $\alpha_0^{(p)}(\tilde{r})$, $\alpha_n^{(hr)}(\tilde{r})$ are used only for $\tilde{r} \in [0, a]$ where $0 < a < 1$. We solve the problem numerically for $\tilde{r} \in [a, 1]$. Then the unknown elements C_0, ε_1 and C_n are determined by matching the series and numerical solutions at the patching point $\tilde{r} = a$.

3.3.2 Numerical solution and its matching with the series solution

In this subsection, the numerical solutions of equations (3.2.14) and (3.2.15) will be explained. We then match series and numerical solutions as the combined solution. At the patching point a, there are patching conditions which ensure the combined solution is smooth and continuous.

Numerical solution of equation (3.2.14) close to the contact line $\tilde{r} = 1$ can be presented in the form

$$\alpha_0(\tilde{r}) = \alpha_0(1)\alpha_0^{(1)}(\tilde{r}) + \alpha_0^{'}(1)\alpha_0^{(2)}(\tilde{r}) + \varepsilon_1\alpha_0^{(3)}(\tilde{r}), \tag{3.3.23}$$

where $\alpha_0(1)$ is given using (3.2.17), and $\alpha_0^{'}(1)$, ε_1 are to be determined using the patching conditions. Here, $\alpha_0^{(1)}(\tilde{r})$ and $\alpha_0^{(2)}(\tilde{r})$ satisfy the homogeneous equation (3.3.2) with the boundary conditions,

$$\begin{cases} \alpha_0^{(1)}(1) = 1, \\ \alpha_{0,\tilde{r}}^{(1)}(1) = 0, \end{cases} \quad \begin{cases} \alpha_0^{(2)}(1) = 0, \\ \alpha_{0,\tilde{r}}^{(2)}(1) = 1, \end{cases} \tag{3.3.24}$$

and $\alpha_0^{(3)}(\tilde{r})$ satisfies equation (3.3.12) subject to the boundary conditions,

$$\begin{cases} \alpha_0^{(3)}(1) = 0, \\ \alpha_{0,\tilde{r}}^{(3)}(1) = 0. \end{cases} \tag{3.3.25}$$

The functions $\alpha_0^{(1)}(\tilde{r})$, $\alpha_0^{(2)}(\tilde{r})$, and $\alpha_0^{(3)}(\tilde{r})$ are obtained numerically by employing the fourth-order Runge–Kutta method. Using the series solution (3.3.15) and numerical solution (3.3.23), the combined solution of the governing equation (3.2.14) is expressed as

$$\alpha_0(\tilde{r}) = \begin{cases} C_0\alpha_0^{(hr)}(\tilde{r}) + \varepsilon_1\alpha_0^{(p)}(\tilde{r}) & (0 < \tilde{r} < a), \\ \alpha_0(1)\alpha_0^{(1)}(\tilde{r}) + \alpha_0^{'}(1)\alpha_0^{(2)}(\tilde{r}) + \varepsilon_1\alpha_0^{(3)}(\tilde{r}) & (a < \tilde{r} < 1). \end{cases} \tag{3.3.26}$$

Here, a is the patching point, where series and numerical solutions and their first derivatives are required to be equal. This patching conditions and (3.2.18) for ε_1 lead to the following system with respect to C_0 and $\alpha_0^{'}(1)$:

$$\begin{aligned} \alpha_0^{(hr)}(a)C_0 - M_{03}\alpha_0^{'}(1) &= \alpha_0^{(1)}(a)\alpha_0(1) + M_{01}k_3, \\ \alpha_{0,\tilde{r}}^{(hr)}(a)C_0 - M_{04}\alpha_0^{'}(1) &= \alpha_{0,\tilde{r}}^{(1)}(a)\alpha_0(1) + M_{02}k_3, \end{aligned} \tag{3.3.27}$$

where k_1 and k_3 are given by equation (3.2.19), and

$$M_{01} = \alpha_0^{(3)}(a) - \alpha_0^{(p)}(a), \qquad M_{03} = M_{01}k_1 + \alpha_0^{(2)}(a),$$
$$M_{02} = \alpha_{0,\tilde{r}}^{(3)}(a) - \alpha_{0,\tilde{r}}^{(p)}(a), \qquad M_{04} = M_{02}k_1 + \alpha_{0,\tilde{r}}^{(2)}(a).$$

Once C_0 and $\alpha_0^{'}(1)$ are determined by solving (3.3.27), ε_1 is calculated using equation (3.2.18), and then the combined solution (3.3.26) is completely determined.

Similarly, the numerical solution of equation (3.2.15) near $\tilde{r} = 1$ is sought in the form,

$$\alpha_n(\tilde{r}) = \alpha_n(1)\alpha_n^{(1)}(\tilde{r}) + \alpha_n^{'}(1)\alpha_n^{(2)}\tilde{r}. \tag{3.3.28}$$

Here $\alpha_n(1)$ is given by (3.2.17) and $\alpha_n^{'}(1)$ is to be determined. The functions $\alpha_n^{(1)}(\tilde{r})$ and $\alpha_n^{(2)}(\tilde{r})$ satisfy the governing equation (3.2.15) subject to the boundary conditions,

$$\begin{cases} \alpha_n^{(1)}(1) = 1, \\ \alpha_{n,\tilde{r}}^{(1)}(1) = 0, \end{cases} \quad \begin{cases} \alpha_n^{(2)}(1) = 0, \\ \alpha_{n,\tilde{r}}^{(2)}(1) = 1. \end{cases} \tag{3.3.29}$$

The corresponding initial value problems are solved numerically. The combined solution of the governing equation (3.2.15) reads

$$\alpha_n(\tilde{r}) = \begin{cases} C_n\alpha_n^{(hr)}(\tilde{r}) & (0 < \tilde{r} < a), \\ \alpha_n(1)\alpha_n^{(1)}(\tilde{r}) + \alpha_n^{'}(1)\alpha_n^{(2)}(\tilde{r}) & (a < \tilde{r} < 1). \end{cases} \tag{3.3.30}$$

The matching conditions at $\tilde{r} = a$ provides the following system of equations with respect to C_n and $\alpha_n^{'}(1)$,

$$\begin{aligned} C_n\alpha_n^{(hr)}(a) - \alpha_n^{'}(1)\alpha_n^{(2)}(a) &= \alpha_n(1)\alpha_n^{(1)}(a), \\ C_n\alpha_{n,\tilde{r}}^{(hr)}(a) - \alpha_n^{'}(1)\alpha_{n,\tilde{r}}^{(2)}(a) &= \alpha_n(1)\alpha_{n,\tilde{r}}^{(1)}(a). \end{aligned} \tag{3.3.31}$$

The first-order correction of the droplet shape was searched in the form of the Fourier series, see equation (3.2.13). The coefficients $\alpha_0(\tilde{r})$ and $\alpha_n(\tilde{r})$ were presented by the equations (3.3.26) and (3.3.30). The unknown constants in (3.3.26) and (3.3.30) were determined by matching conditions (3.3.27) and (3.3.31). Once the whole functions and constants are calculated, the first-order correction of the contact angle is then computed using equation (3.2.20).

3.4 Example

If the shape of the solid substrate is continuous in $\varphi \in (-\pi, \pi)$, and is expressed in the form of Fourier series,

$$\tilde{z}_p(\tilde{r}, \varphi) = z_0(\tilde{r}) + \sum_{j=1}^{\infty} \left[z_j(\tilde{r}) \cos j\varphi + z_j^*(\tilde{r}) \sin j\varphi \right], \tag{3.4.1}$$

the first-order correction of the droplet shape is obtained through the superposition of the corresponding n case. We present two examples. The first is the simplest case, where the droplet is placed on a plate inclining gradually. This problem corresponding to the $n = 1$ case only required one single value $n = 1$ to solve. In the second example, we consider a more complex deformation of the substrate, which requires the inclusion of all of n for approximation.

3.4.1 Inclining plate

We consider a solid plate, which is initially horizontal and then starts to incline. In the dimensionless variables, the position of the plate is described by the equation

$$\tilde{z}_p(\tilde{r}, \varphi) = A(t)\tilde{r} \cos \varphi, \tag{3.4.2}$$

where $A(0) = 0$ and $A(t) > 0$ as $t > 0$. The function $A(t)$ is not specific here. The problem for the first-order correction of the droplet shape caused by the plate inclination (3.2.5), (3.2.10), and (3.2.11) is linear with respect to $A(t)$. Therefore, we can solve the problem for $A(t) = 1$ and multiply the final solution by $A(t)$ at the end of the analysis. In particular, the correction to the local contact angle $V(\varphi)$ by (3.2.12) is proportional to $A(t)$. In this case, we get $k_3 = 0$, see equation (3.2.19), and $\alpha_0(1) = 0$, see equation (3.2.17), so the patching conditions (3.3.27) are reduced to

$$\begin{aligned} \alpha_0^{(hr)}(a)C_0 + M_{03}\alpha_0'(1) &= 0, \\ \alpha_{0,\tilde{r}}^{(hr)}(a)C_0 + M_{04}\alpha_0'(1) &= 0, \end{aligned} \tag{3.4.3}$$

resulting in $C_0 = \alpha_0'(1) = 0$. Next, $\varepsilon_1 = 0$ is calculated using equation (3.2.18). Likewise, since $\alpha_n(1) = 0$ for $n \geq 2$, the patching conditions (3.3.31) become

$$\begin{aligned} \alpha_n^{(hr)}(a)C_n - \alpha_n^{(2)}(a)\alpha_n'(1) &= 0, \\ \alpha_{n,\tilde{r}}^{(hr)}(a)C_n - \alpha_{n,\tilde{r}}^{(2)}(a)\alpha_n'(1) &= 0, \end{aligned} \tag{3.4.4}$$

which gives $C_n = \alpha_n'(1) = 0$. In other words, for the inclined plate case, we only need to solve for $\alpha_1(\tilde{r})$ since the remaining terms are all zeros. Thus, the

first-order correction of the droplet shape reads

$$F_1(\tilde{r},\varphi) = \begin{cases} C_1\alpha_1^{(hr)}(\tilde{r})\cos\varphi & (0<\tilde{r}<a), \\ \left(\alpha_1(1)\alpha_1^{(1)}(\tilde{r}) + \alpha_1^{'}(1)\alpha_1^{(2)}(\tilde{r})\right)\cos\varphi & (a<\tilde{r}<1), \end{cases} \tag{3.4.5}$$

where C_1 and $\alpha_1^{'}(1)$ are solutions of the system,

$$\begin{aligned} \alpha_1^{(hr)}(a)C_1 - \alpha_1^{(2)}(a)\alpha_1^{'}(1) &= \alpha_1^{(1)}(a), \\ \alpha_{1,\tilde{r}}^{(hr)}(a)C_1 - \alpha_{1,\tilde{r}}^{(2)}(a)\alpha_1^{'}(1) &= \alpha_{1,\tilde{r}}^{(1)}(a). \end{aligned} \tag{3.4.6}$$

where a is the patching point. By solving the system of equations (3.4.6), we obtain the values of C_1 and $\alpha_1^{'}(1)$. Once getting C_1 and $\alpha_1^{'}(1)$, the solution (3.4.5) is complete determined. The first-order correction of the droplet $F_1(\tilde{r})$ and its first derivative $F_1^{'}(\tilde{r})$ are calculated by selecting the patching point $a = 0.4$, as illustrated in Figure 3.4.1. The blue line represents the series solution from the centre to the patching point, while the red line depicts the numerical solution.

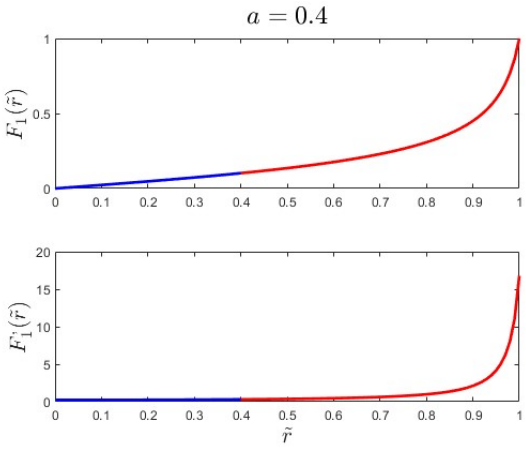

Figure 3.4.1: $F_1(\tilde{r})$ and $F_1^{'}(\tilde{r})$ calculated by choosing the patching point $a = 0.4$.

As expected, the first-order droplet shape is continuous and smooth since it follows the patching conditions. To verify the effect of the patching point, the difference between the second derivatives of the series and numerical solutions at various patching points is depicted in Figure 3.4.2. The significant increase in the jump of the second derivative at $a = 0.2$ and $a = 0.8$ may be due to the series solution's inadequacy as $\tilde{r} \to 1$, while the numerical solution's divergence as $\tilde{r} \to 0$. Given that the difference at $a = 0.4$ is less than in other cases, we adopt $a = 0.4$ as the patching point throughout this thesis unless stated otherwise.

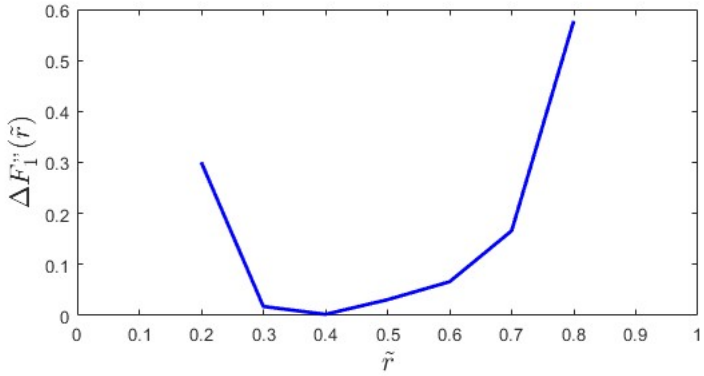

Figure 3.4.2: The difference in the second derivative between the series and numerical solutions varies across different patching points, ranging from $\tilde{r} = 0.2$ to $\tilde{r} = 0.8$.

The droplet shape is obtained by summing the leading order term and the first-order correction. The initial droplet is obtained from section 2.4 for water and $V_0 = 0.1\,\mathrm{mL}$ and $\theta_e = 70°$, depicted in Figure 3.4.3 by the blue dashed line. By choosing $\delta = 0.1$, a cross-section of the free surface of the droplet at $\varphi = 0$ is shown in Figure 3.4.3, while the black line represents the inclined plate.

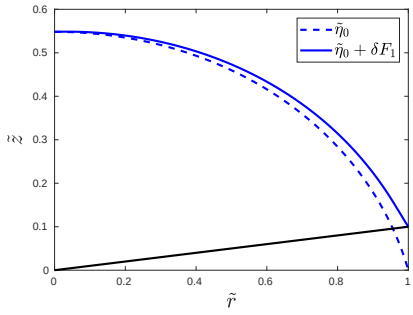

Figure 3.4.3: Cross-sections of the droplet shape at $\varphi = 0$.

Cross-sections of the droplet shape are presented at $\varphi = 0$, $\varphi = \pi/4$, and $\varphi = \pi/2$, as depicted in Figure 3.4.4. To provide a more detailed explanation, let us consider the first figure. The right half of the figure represents the polar angle $\varphi = 0$, while the left half corresponds to $\varphi = \pi$. This shape exhibits line symmetry along the $y = 0$ plane, so we display only the interval $\varphi \in (0, \pi/2)$. Building upon these results, we present a three-dimensional droplet shape in Figure 3.4.5.

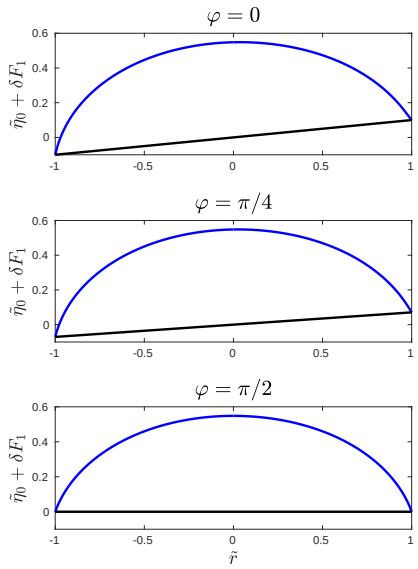

Figure 3.4.4: Cross-sections of the droplet shape at $\varphi = 0$, $\varphi = \pi/4$, and $\varphi = \pi/2$.

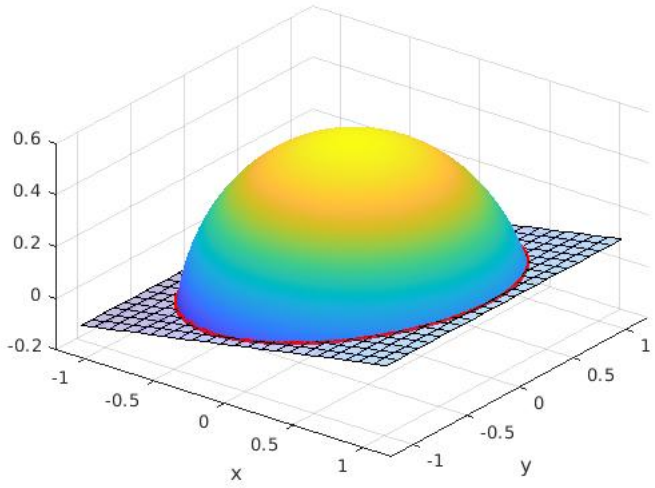

Figure 3.4.5: A three-dimensional droplet on an inclined plate.

Lastly, the local contact angle varying along the contact line is calculated using equation (3.2.20), which is reduced to

$$V(\varphi) = \varepsilon_0 \left(1 - \cos^2 \theta_e \alpha_1'(1)\right) \cos\varphi. \tag{3.4.7}$$

The local contact angle varies with the polar angle φ, as illustrated in Figure 3.4.6. A red line indicates the value of the equilibrium contact angle θ. The local contact angle equals the equilibrium contact angle at $\varphi = \pi/2$ and $\varphi = 3\pi/2$.

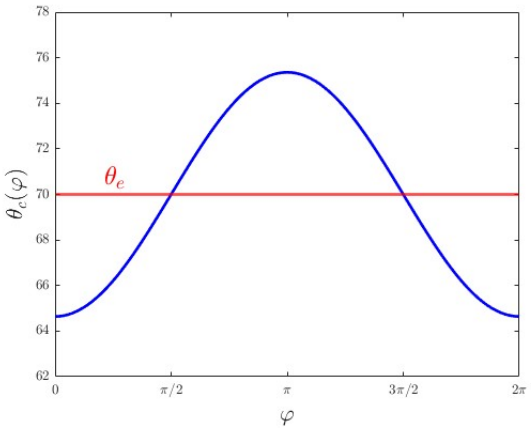

Figure 3.4.6: Contact angle $\theta_c(\varphi)$ varies with the polar angle.

3.4.2 Substrate with a combined slope

We consider the solid surface described by

$$\tilde{z}_p(\tilde{r},\varphi) = \begin{cases} A(t)\tilde{r}\cos\varphi & (-\pi/2 < \varphi < \pi/2), \\ 0 & (-\pi < \varphi < -\pi/2, \quad \pi/2 < \varphi < \pi), \end{cases} \tag{3.4.8}$$

as depicted in Figure 3.4.7. Again, the first-order correction of the droplet shape is proportional to $A(t)$ in the leading order. This is why we set $A(t) = 1$ in the following analysis.

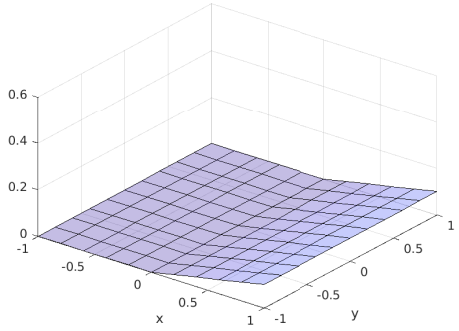

Figure 3.4.7: An solid substrate with a different slope.

The first-order correction of the droplet shape reads

$$F_1(\tilde{r},\varphi) = \begin{cases} C_0\alpha_0^{(hr)}(\tilde{r}) + \varepsilon_1\alpha_0^{(p)}(\tilde{r}) + \sum_{n=1}^{\infty} C_n\alpha_n^{(hr)}(\tilde{r})\cos n\varphi & (0 < \tilde{r} < a), \\ \alpha_0(1)\alpha_0^{(1)}(\tilde{r}) + \alpha_0'(1)\alpha_0^{(2)}(\tilde{r}) + \varepsilon_1\alpha_0^{(3)}(\tilde{r}) \\ + \sum_{n=1}^{\infty}\left(\alpha_n(1)\alpha_n^{(1)}(\tilde{r}) + \alpha_n'(1)\alpha_n^{(2)}(\tilde{r})\right)\cos n\varphi & (a < \tilde{r} < 1), \end{cases} \tag{3.4.9}$$

where a is the patching point. In this case, we have double integrals

$$\int_{-\pi}^{\pi}\int_{0}^{1}\tilde{z}_p(\tilde{r},\varphi)\tilde{r}d\tilde{r}d\varphi=\int_{-\pi/2}^{\pi/2}\int_{0}^{1}\tilde{r}^2\cos\varphi d\tilde{r}d\varphi=2/3. \tag{3.4.10}$$

The corresponding boundary condition to each case gives

$$\begin{aligned}
\alpha_0(1)=&\frac{1}{2\pi}\int_{-\pi}^{\pi}\tilde{z}_p(1,\varphi)d\varphi=\frac{1}{2\pi}\int_{-\pi/2}^{\pi/2}\cos\varphi d\varphi=\frac{1}{\pi},\\
\alpha_1(1)=&\frac{1}{\pi}\int_{-\pi/2}^{\pi/2}\cos^2\varphi d\varphi=\frac{1}{\pi}\int_{-\pi/2}^{\pi/2}\frac{1+\cos(2\varphi)}{2}d\varphi=\frac{1}{2},\\
\alpha_n(1)=&\frac{1}{\pi}\int_{-\pi/2}^{\pi/2}\cos(n\varphi)\cos\varphi d\varphi=-\frac{2}{\pi}\frac{\cos(n\pi/2)}{n^2-1}\quad(n\geq 2),\\
\alpha_n^*(1)=&\frac{1}{\pi}\int_{-\pi/2}^{\pi/2}\sin(n\varphi)\cos\varphi d\varphi=0,\quad(n\geq 1).
\end{aligned}$$

In the current case, we have k_3 due to the unbalanced deformation of the substrate. In addition, the function of the shape of the substrate is symmetric along the x-axis (even function), so there is no contribution from the coefficients A_n^*. The first correction of the droplet shape is more complicated since we now need to consider all values of n. The Fourier series of the first-order correction of the droplet is truncated at $n=N$:

$$F_1(\tilde{r},\varphi)\approx F_N=\alpha_0(\tilde{r})+\sum_{n=1}^{N}\left[\alpha_n(\tilde{r})\cos n\varphi+\alpha_n^*(\tilde{r})\sin n\varphi\right]. \tag{3.4.11}$$

We use the following equation to verify the difference of truncated Fourier approximations at $n=N$ and $n=N+1$,

$$D_e(N)=\int_{0}^{1}\int_{-\pi}^{\pi}|F_{N+1}-F_N|^2d\varphi d\tilde{r}. \tag{3.4.12}$$

D_e is calculated as illustrated in Figure 3.4.8, which shows that D_e decrease with N and it become small once $N>6$. Hence, we choose $N=10$ for this example. Furthermore, the difference D_e is significantly small when N is an odd number. This occurs because the coefficients A_n are equal to zero for $n=2,4,6,8,\cdots$.

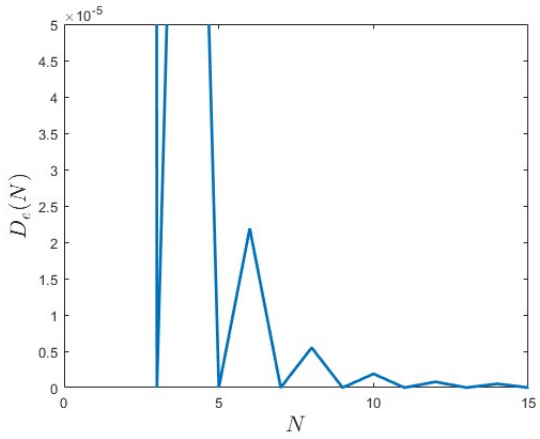

Figure 3.4.8: The difference in the truncated droplet shape corresponds to the values of N.

The initial droplet shape was calculated for $V_0 = 0.1\,\mathrm{mL}$ and $\theta_e = 70°$. We then obtain the final droplet shape by summing the leading order term and first-order correction. Cross-sections of the droplet at $\varphi = 0$ and $\varphi = \pi/2$ are depicted in Figure 3.4.9, while the three-dimensional droplet shape is presented in Figure 3.4.10.

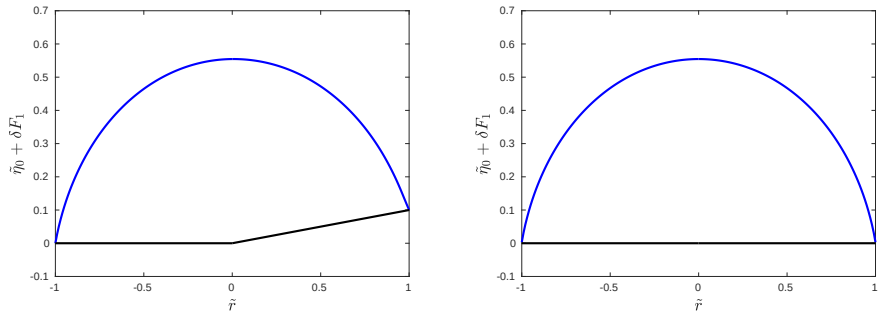

Figure 3.4.9: The asymptotic solution of the droplet at $\varphi = 0$ and $\varphi = \pi/2$.

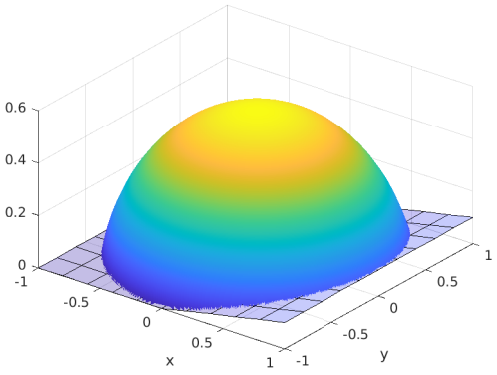

Figure 3.4.10: A three-dimensional droplet shape on a solid shape with different slopes.

After calculating the shape of the droplet, we examine the contact angle, as depicted in Figure 3.4.11. On the left half of the plate, where the solid surface is flat, the local contact angle increases. Since the contact line is pinned, the increase in the local contact angle on the left side balances the change in the local contact angle on the right side of the solid surface. The local contact angle on the inclined right half of the plate becomes smaller than the equilibrium contact angle, but surprisingly, some parts become larger near the $\varphi = \pi/2$ and $\varphi = 3\pi/2$.

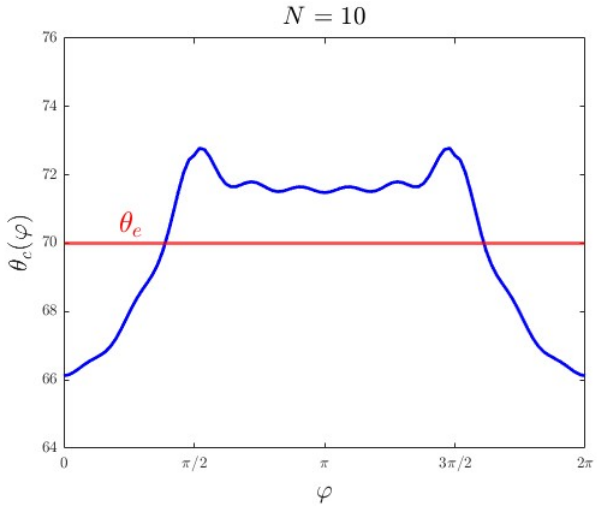

Figure 3.4.11: The local contact angle of the droplet on a solid surface with different slopes.

We observe wiggles in the result when $N = 10$ is chosen. Therefore, we also present the results for higher values of N, as shown in Figure 3.4.12. As N increases, the wiggles diminish, but we observe the significant peaks at $\varphi = \pi/2$ and $\varphi = 3\pi/2$.

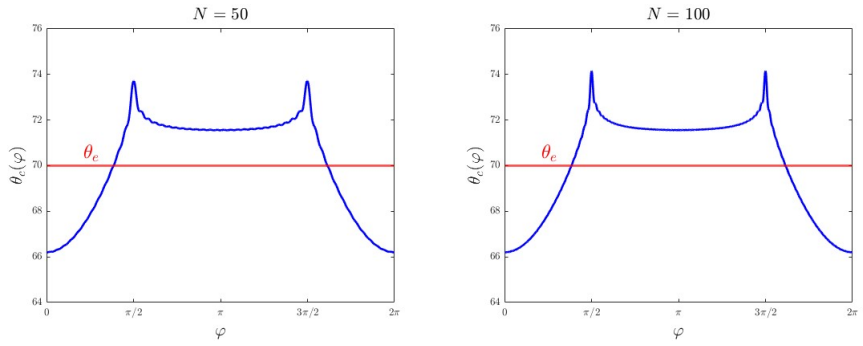

Figure 3.4.12: For the cases where the truncation numbers $N = 50$ and $N = 100$ are selected, the local contact angle varies with the polar angle.

4

Moving contact line model with equilibrium contact angle

We investigate the dynamic behaviour of a three-dimensional droplet with a given volume placed on a solid substrate that undergoes slow changes over time. We employ the quasi-static approximation, see section 2.5, to analyse this dynamic problem. Initially, the solid surface is assumed to be flat and horizontal, while the droplet possesses an axisymmetric shape. In contrast to the previous chapter, the contact line is now unpinned. This implies that the droplet has the freedom to move, making a problem with an unknown domain. We consider that the contact line is allowed to move until the current local contact angle, θ_c, is equal to the equilibrium contact angle, θ_e. Within this model, we should determine both the shape of the droplet and the position of the unknown contact line simultaneously.

This chapter begins by outlining the formulation of the problem in dimensionless cylindrical coordinates, which follows the formulation from Chapter 3. In the model of this chapter, the projection of the contact line onto the xy-plane may no longer remain circular, so we introduce the stretched coordinates to incorporate the contact line into our equations.

A methodology similar to that in the previous chapter is used to analyse the present problem. However, now the position of the contact line is unknown in contrast to the model of chapter 3. By employing the perturbation method under the assumption that the small deformation of the substrate compared to the thickness of the droplet, and the Fourier decomposition, we derive a set of ordinary differential equations with variable coefficients for the functions of the radial coordinate in the Fourier series. The resulting ordinary differential equations are similar to the outcome in the previous chapter, but they become more complicated due to the contribution from the configuration of the contact line, introducing non-homogeneous terms into the equations. These ordinary differential equations are solved independently. As coefficients in the ordinary differential equations are singular, we employ a similar approach as in chapter 3, which involves matching the series solution and the numerical solution at a patching point $a \in (0, 1)$. At the end of the chapter, we provide illustrative examples of the droplet placed on an inclined plate and a saddle shape.

4.1 Problem description

The projection of the contact line is now considered to be non-circular. It is described in dimensionless variables, which are introduced by (3.1.12), by the equation $\tilde{r} = \tilde{r}_c(\varphi, t)$, where $\tilde{r}_c(\varphi, t) = r_c(\varphi, t)/R_0$, see section 2.3. Here R_0 is the contact radius of the initial droplet shape $\bar{\eta}_0(r)$. Note that the function $\tilde{r}_c(\varphi, t)$ is unknown and should be determined as part of the solution. Since we employ the quasi-static approximation, see section 2.5, to analyse our problem, the parameter t is not included in the following formulation.

As a droplet is placed on a given solid substrate described by the equation $\tilde{z} = \delta \tilde{z}_p(\tilde{r}, \varphi)$, where $\delta = Z_{sc}/B(t)$ is the ratio of the vertical scale of the substrate to the current thickness of the droplet, the free surface of the droplet at each time instant is governing by the equation

$$\frac{a_2 + \varepsilon^2 a_3}{(1 + \varepsilon^2 a_1)^{3/2}} = Bo[\tilde{\eta}(\tilde{r}, \varphi) - 1] \qquad (\tilde{r} < \tilde{r}_c(\varphi), \quad -\pi < \varphi < \pi), \tag{4.1.1}$$

where $Bo = \rho g R_0^2/\gamma$ is the Bond number, $\varepsilon = B/R_0$, see equation (3.1.13), and the functions a_1, a_2, a_3 are given by equation (3.1.14). In this model of the unpinned contact line, a boundary condition on the contact line gives

$$\tilde{\eta}(\tilde{r}_c(\varphi), \varphi) = \delta \tilde{z}_p(\tilde{r}_c(\varphi), \varphi), \tag{4.1.2}$$

see equation (3.1.15), and the local contact angle along the contact line is assumed to be equal to the equilibrium contact angle θ_e. Thus, equation (3.1.16) for the contact angle at the contact line gives the second boundary condition,

$$\frac{1 + \varepsilon\varepsilon_z \left(\tilde{\eta}_{\tilde{r}} \tilde{z}_{p\tilde{r}} + \dfrac{1}{\tilde{r}^2} \tilde{\eta}_\varphi \tilde{z}_{p\varphi} \right)}{\sqrt{1 + \varepsilon^2 \left(\tilde{\eta}_{\tilde{r}}^2 + \dfrac{\tilde{\eta}_\varphi^2}{\tilde{r}^2} \right)} \sqrt{1 + \varepsilon_z^2 \left(\tilde{z}_{p\tilde{r}}^2 + \dfrac{\tilde{z}_{p\varphi}^2}{\tilde{r}^2} \right)}} = \cos\theta_e \quad (\tilde{r} = \tilde{r}_c(\varphi), \quad -\pi < \varphi < \pi), \tag{4.1.3}$$

where $\varepsilon_z = \delta\varepsilon$. The condition (3.1.17) of the constant volume of the droplet reads

$$\begin{aligned} -\frac{1}{Bo} \int_{-\pi}^{\pi} \left(\frac{\varepsilon(\tilde{\eta}_{\tilde{r}} \hat{\mathbf{e}}_{\mathbf{r}} + \frac{1}{\tilde{r}} \tilde{\eta}_\varphi \hat{\mathbf{e}}_\varphi)}{\sqrt{1 + \varepsilon^2 (\tilde{\eta}_{\tilde{r}}^2 + \frac{1}{\tilde{r}^2} \tilde{\eta}_\varphi^2)}} \right)_{\tilde{r} = \tilde{r}_c} \cdot \mathbf{n_2} \tilde{r}_c(\varphi) d\varphi \\ = \varepsilon \left(|S| - \delta \int_{-\pi}^{\pi} \int_0^{\tilde{r}_c} \tilde{z}_p(\tilde{r}, \varphi) \tilde{r} d\tilde{r} d\varphi \right) - \frac{V_0}{R_0^3}, \end{aligned} \tag{4.1.4}$$

where $|S| = \frac{1}{2} \int_{-\pi}^{\pi} \tilde{r}_c^2(\varphi) d\varphi$, and $\mathbf{n_2}$ is the outward unit normal vector to the projection of the contact line onto the xy-plane. The two-dimensional contact

line can be represented by parameterised equations in terms of φ,

$$\begin{cases} x(\varphi) = \tilde{r}_c(\varphi)\cos\varphi, \\ y(\varphi) = \tilde{r}_c(\varphi)\sin\varphi. \end{cases}$$

By differentiating these parametric equations with respect to φ, we obtain the tangent vector to the two-dimensional contact line, $\mathbf{T_2} = x^{'}(\varphi)\hat{\mathbf{i}} + y^{'}(\varphi)\hat{\mathbf{j}}$, then the outward unit normal vector reads

$$\begin{aligned} \mathbf{n_2} =& \frac{y^{'}(\varphi)}{\sqrt{(x^{'})^2 + (y^{'})^2}}\hat{\mathbf{i}} - \frac{x^{'}(\varphi)}{\sqrt{(x^{'})^2 + (y^{'})^2}}\hat{\mathbf{j}}, \\ =& \frac{\tilde{r}_c(\varphi)}{\sqrt{\tilde{r}_c^2 + (\tilde{r}_c^{'})^2}}\hat{\mathbf{e}}_{\mathbf{r}} + \frac{\tilde{r}_c^{'}(\varphi)}{\sqrt{\tilde{r}_c^2 + (\tilde{r}_c^{'})^2}}\hat{\mathbf{e}}_{\varphi}. \end{aligned}$$

The boundary value problem (4.1.1)–(4.1.3) in the unknown region $\tilde{r} < \tilde{r}_c(\varphi)$ is complicated, so we introduce the stretched coordinates to incorporate $\tilde{r}_c(\varphi)$ into our equations for the further analysis. In this coordinate system, the radial variable is scaled as follows,

$$\tilde{r} = \xi\tilde{r}_c(\varphi). \tag{4.1.5}$$

Within these dimensionless stretched coordinates, the free surface of the droplet and the solid surface are represented by $F(\xi, \varphi)$ and $Z(\xi, \varphi)$, respectively, where

$$\begin{aligned} \tilde{\eta}(\tilde{r}, \varphi) &= \tilde{\eta}(\xi\tilde{r}_c(\varphi), \varphi) = F(\xi, \varphi), \\ \tilde{z}_p(\tilde{r}, \varphi) &= \tilde{z}_p(\xi\tilde{r}_c(\varphi), \varphi) = Z(\xi, \varphi). \end{aligned}$$

We first establish the transformation between the two coordinate systems to derive the governing equation and boundary conditions in the stretched coordinates. The transformations for the derivatives of the droplet shape take the form

$$\begin{aligned} F_{\xi} =& \tilde{r}_c(\varphi)\tilde{\eta}_{\tilde{r}}, \\ F_{\varphi} =& \xi\tilde{r}_c^{'}(\varphi)\tilde{\eta}_{\tilde{r}} + \tilde{\eta}_{\varphi}, \\ F_{\xi\xi} =& \tilde{r}_c^2(\varphi)\tilde{\eta}_{\tilde{r}\tilde{r}}, \\ F_{\xi\varphi} =& \xi\tilde{r}_c^{'}(\varphi)\tilde{r}_c(\varphi)\tilde{\eta}_{\tilde{r}\tilde{r}} + \tilde{r}_c(\varphi)\tilde{\eta}_{\tilde{r}\varphi} + \tilde{r}_c^{'}(\varphi)\tilde{\eta}_{\tilde{r}}, \\ F_{\varphi\varphi} =& \left(\xi\tilde{r}_c^{'}(\varphi)\right)^2\tilde{\eta}_{\tilde{r}\tilde{r}} + 2\xi\tilde{r}_c^{'}(\varphi)\tilde{\eta}_{\tilde{r}\varphi} + \xi\tilde{r}_c^{''}(\varphi)\tilde{\eta}_{\tilde{r}} + \tilde{\eta}_{\varphi\varphi}. \end{aligned}$$

Rearranging the above equations, we obtain

$$\begin{aligned}
\tilde{\eta}_{\tilde{r}} =& \frac{1}{\tilde{r}_c} F_\xi, \\
\tilde{\eta}_{\varphi} =& F_\varphi - \xi \frac{\tilde{r}_c^{'}}{\tilde{r}_c} F_\xi, \\
\tilde{\eta}_{\tilde{r}\tilde{r}} =& \frac{1}{\tilde{r}_c^2} F_{\xi\xi}, \\
\tilde{\eta}_{\tilde{r}\varphi} =& \frac{1}{\tilde{r}_c} F_{\xi\varphi} - \xi \frac{\tilde{r}_c^{'}}{\tilde{r}_c^2} F_{\xi\xi} - \frac{\tilde{r}_c^{'}}{\tilde{r}_c^2} F_\xi, \\
\tilde{\eta}_{\varphi\varphi} =& F_{\varphi\varphi} + \xi^2 \frac{(\tilde{r}_c^{'})^2}{\tilde{r}_c^2} F_{\xi\xi} - 2\xi \frac{\tilde{r}_c^{'}}{\tilde{r}_c} F_{\xi\varphi} + 2\xi \frac{(\tilde{r}_c^{'})^2}{\tilde{r}_c^2} F_\xi - \xi \frac{\tilde{r}_c^{''}}{\tilde{r}_c} F_\xi.
\end{aligned} \tag{4.1.6}$$

Likewise, following the above equations, we have the transformations for the derivatives of the solid substrate, but now $\tilde{\eta}$ is replaced by $\tilde{z}_p$ and F by Z. Substituting the transformations (4.1.6) into the governing equation (4.1.1), we obtain

$$\frac{a_2 + \varepsilon^2 a_3}{(1 + \varepsilon^2 a_1)^{3/2}} = Bo[F(\xi, \varphi) - 1] \qquad (\xi < 1, \quad -\pi < \varphi < \pi), \tag{4.1.7}$$

where

$$\begin{aligned}
a_1 =& \left(\frac{1}{\tilde{r}_c^2} + \frac{(\tilde{r}_c^{'})^2}{\tilde{r}_c^4} \right) F_\xi^2 - \frac{2}{\xi} \frac{\tilde{r}_c^{'}}{\tilde{r}_c^3} F_\xi F_\varphi + \frac{1}{\xi^2} \frac{1}{\tilde{r}_c^2} F_\varphi^2, \\
a_2 =& \left(\frac{1}{\tilde{r}_c^2} + \frac{(\tilde{r}_c^{'})^2}{\tilde{r}_c^4} \right) F_{\xi\xi} - \frac{2}{\xi} \frac{\tilde{r}_c^{'}}{\tilde{r}_c^3} F_{\xi\varphi} + \frac{1}{\xi^2} \frac{1}{\tilde{r}_c^2} F_{\varphi\varphi} + \frac{1}{\xi} \left(\frac{1}{\tilde{r}_c^2} + 2\frac{(\tilde{r}_c^{'})^2}{\tilde{r}_c^4} - \frac{\tilde{r}_c^{''}}{\tilde{r}_c^3} \right) F_\xi, \\
a_3 =& \frac{1}{\xi^2} \frac{1}{\tilde{r}_c^4} (F_\xi^2 F_{\varphi\varphi} + F_\varphi^2 F_{\xi\xi}) + \frac{1}{\xi} \left(\frac{1}{\tilde{r}_c^4} + 2\frac{(\tilde{r}_c^{'})^2}{\tilde{r}_c^6} - \frac{\tilde{r}_c^{''}}{\tilde{r}_c^5} \right) F_\xi^3 \\
& - \frac{2}{\xi^2} \frac{\tilde{r}_c^{'}}{\tilde{r}_c^5} F_\xi^2 F_\varphi + \frac{2}{\xi^3} \frac{1}{\tilde{r}_c^4} F_\xi F_\varphi^2 - \frac{2}{\xi^2} \frac{1}{\tilde{r}_c^4} F_\xi F_\varphi F_{\xi\varphi}.
\end{aligned} \tag{4.1.8}$$

Substituting the transformations for the droplet shape (4.1.6) and the solid surface into boundary conditions (4.1.2)–(4.1.3), we obtain

$$F(\xi, \varphi) = \delta Z(\xi, \varphi) \qquad (\xi = 1, \quad -\pi < \varphi < \pi), \tag{4.1.9}$$

$$\frac{1 + \varepsilon\varepsilon_z a_5}{\sqrt{1 + \varepsilon^2 a_4}\sqrt{1 + \varepsilon_z^2 a_6}} = \cos\theta_e \qquad (\xi = 1, \quad -\pi < \varphi < \pi), \tag{4.1.10}$$

where

$$\begin{aligned} a_4 =& \frac{1}{\tilde{r}_c^2} F_\varphi^2 - 2\frac{\tilde{r}_c'}{\tilde{r}_c^3} F_\varphi F_\xi + \left(\frac{1}{\tilde{r}_c^2} + \frac{(\tilde{r}_c')^2}{\tilde{r}_c^4} \right) F_\xi^2, \\ a_5 =& \frac{1}{\tilde{r}_c^2} F_\varphi Z_\varphi - \frac{\tilde{r}_c'}{\tilde{r}_c^3} (F_\varphi Z_\xi + Z_\varphi F_\xi) + \left(\frac{1}{\tilde{r}_c^2} + \frac{(\tilde{r}_c')^2}{\tilde{r}_c^4} \right) F_\xi Z_\xi, \\ a_6 =& \frac{1}{\tilde{r}_c^2} Z_\varphi^2 - 2\frac{\tilde{r}_c'}{\tilde{r}_c^3} Z_\varphi Z_\xi + \left(\frac{1}{\tilde{r}_c^2} + \frac{(\tilde{r}_c')^2}{\tilde{r}_c^4} \right) Z_\xi^2. \end{aligned} \tag{4.1.11}$$

Equation (4.1.4) becomes

$$-\frac{1}{Bo} \int_{-\pi}^{\pi} \left(\frac{\varepsilon a_7 \tilde{r}_c(\varphi)}{\sqrt{1+\varepsilon^2 a_4}} \right) d\varphi = \varepsilon \left(|S| - \delta \int_{-\pi}^{\pi} \int_0^1 Z(\xi,\varphi) \tilde{r}_c^2(\varphi) \xi d\xi d\varphi \right) - \frac{V_0}{R_0^3}, \tag{4.1.12}$$

where $|S| = \frac{1}{2} \int_{-\pi}^{\pi} \tilde{r}_c^2(\varphi) d\varphi$,

$$a_7 = \frac{F_\xi(1,\varphi)}{\sqrt{\tilde{r}_c^2 + (\tilde{r}_c')^2}} + \frac{\tilde{r}_c \tilde{r}_c' F_\varphi(1,\varphi) - (\tilde{r}_c')^2 F_\xi(1,\varphi)}{\tilde{r}_c^2 \sqrt{\tilde{r}_c^2 + (\tilde{r}_c')^2}}. \tag{4.1.13}$$

This section presented the complete formulation of the problem with the constant contact angle in the stretched coordinates, where the contact line is incorporated in the governing equation and the boundary conditions.

4.2 Asymptotic method

We seek an asymptotic solution to the problem for small deformations of the substrate with $\delta \to 0$. We are concerned with the first-order correction to the leading order axisymmetric solution obtained in section 2.4. The droplet shape, the radius of the contact line, the aspect ratio and the solid surface are sought in the forms,

$$\begin{aligned} F =& F_0(\xi) + \delta F_1(\xi,\varphi) + O(\delta^2), \\ \tilde{r}_c(\varphi) =& 1 + \delta g(\varphi) + O(\delta^2), \\ \varepsilon =& \varepsilon_0 + \delta \varepsilon_1 + O(\delta^2), \\ Z(\xi,\varphi) =& \tilde{z}_p(\xi,\varphi) + \delta \xi g(\varphi) \tilde{z}_{p,r}(\xi,\varphi) + O(\delta^2). \end{aligned} \tag{4.2.1}$$

The expansions of $(1+\varepsilon^2 a_1)^{-3/2}$ and $a_2+\varepsilon a_3$ are given by

$$\frac{1}{(1+\varepsilon^2 a_1)^{3/2}} = \frac{1}{\left(1+\varepsilon_0^2 F_{0,\xi}^2\right)^{3/2}} - 3\delta \frac{\varepsilon_0^2 F_{0,\xi} F_{1,\xi} + \varepsilon_0 \varepsilon_1 F_{0,\xi}^2 - \varepsilon_0^2 F_{0,\xi}^2 g(\varphi)}{\left(1+\varepsilon_0^2 F_{0,\xi}^2\right)^{5/2}} + O(\delta^2), \tag{4.2.2}$$

$$\begin{aligned} a_2+\varepsilon a_3 = {} & F_{0,\xi\xi} + \frac{1}{\xi} F_{0,\xi} + \frac{1}{\xi}\varepsilon_0^2 F_{0,\xi}^3 \\ & + \delta\left(F_{1,\xi\xi} + (1+3\varepsilon_0^2 F_{0,\xi}^2)\frac{F_{1,\xi}}{\xi} + (1+\varepsilon_0^2 F_{0,\xi}^2)\frac{F_{1,\varphi\varphi}}{\xi^2} + \frac{2\varepsilon_0 F_{0,\xi}^3}{\xi}\varepsilon_1 \right) \\ & - 2\delta\left(F_{0,\xi\xi} + (1+2\varepsilon_0^2 F_{0,\xi}^2)\frac{F_{0,\xi}}{\xi} \right) g(\varphi) - \delta(1+\varepsilon_0^2 F_{0,\xi}^2)\frac{F_{0,\xi}}{\xi} g''(\varphi) + O(\delta^2). \end{aligned} \tag{4.2.3}$$

Substituting the expansions (4.2.2) and (4.2.3) into (4.1.7), and using the leading order term of the governing equation, see equation (3.2.4), the first-order correction of the droplet shape reads

$$\begin{aligned} H_1(\xi) F_{1,\xi\xi} + H_2(\xi)\frac{F_{1,\xi}}{\xi} + H_3(\xi)\frac{F_{1,\varphi\varphi}}{\xi^2} + H_4(\xi)\varepsilon_1 \\ + H_5(\xi) g(\varphi) + H_6(\xi) g''(\varphi) = Bo F_1 \qquad (\xi < 1), \end{aligned} \tag{4.2.4}$$

where the functions $H_i(\xi)$, $i=1,2,3,4$, are defined in equation (3.2.6) and

$$\begin{aligned} H_5(\xi) &= Bo(F_0-1)\left(\frac{3\varepsilon_0^2 F_{0,\xi}^2}{1+\varepsilon_0^2 F_{0,\xi}^2} - 2 \right) - \frac{2\varepsilon_0^2 F_{0,\xi}^3}{\xi\left(1+\varepsilon_0^2 F_{0,\xi}^2\right)^{3/2}}, \\ H_6(\xi) &= -\frac{F_{0,\xi}}{\xi\sqrt{1+\varepsilon_0^2 F_{0,\xi}^2}}. \end{aligned} \tag{4.2.5}$$

Substituting the expansions (4.2.1) into (4.1.9)–(4.1.12), using $F_{0,\xi}(1) = -\tan\theta_e/\varepsilon_0$, see equation (2.4.17), and collecting the terms of order $O(\delta)$, we obtain the first-order corrections of the boundary conditions,

$$F_1(1,\varphi) = \tilde{z}_p(1,\varphi), \tag{4.2.6}$$

$$F_{1,\xi}(1,\varphi) = \frac{\tilde{z}_{p,\xi}(1,\varphi)}{\cos^2\theta_e} + \frac{\tan\theta_e}{\varepsilon_0}\left(\frac{\varepsilon_1}{\varepsilon_0} - g(\varphi) \right), \tag{4.2.7}$$

and the following relation for constant ε_1,

$$\begin{aligned} \frac{1}{Bo}\int_{-\pi}^{\pi} & \left(\sin\theta_e \cos^2\theta_e \frac{\varepsilon_1}{\varepsilon_0} - \cos^3\theta_e \varepsilon_0 F_{1,\xi}(1,\varphi) + \sin^3\theta_e g(\varphi) \right) d\varphi \\ & = \varepsilon_1 \pi + \varepsilon_0 \left(\int_{-\pi}^{\pi} g(\varphi) d\varphi - \int_{-\pi}^{\pi}\int_0^1 \tilde{z}_p(\xi,\varphi)\xi d\xi d\varphi \right). \end{aligned} \tag{4.2.8}$$

The governing equation for the first-order correction of the free surface of the droplet (4.2.4) is a linear second-order partial differential equation with singular variable coefficients, which should be solved together with (4.2.6)–(4.2.8). We employ the Fourier decomposition to separate the variables ξ and φ, where the first-order correction of the free surface, $F_1(\xi,\varphi)$, and the first-order correction of the contact line, $g(\varphi)$, are searched in the Fourier series forms,

$$F_1(\xi,\varphi)=\alpha_0(\xi)+\sum_{n=1}^{\infty}[\alpha_n(\xi)\cos n\varphi+\alpha_n^*(\xi)\sin n\varphi], \tag{4.2.9}$$

$$g(\varphi)=A_0+\sum_{n=1}^{\infty}[A_n\cos n\varphi+A_n^*\sin n\varphi], \tag{4.2.10}$$

where coefficients $\alpha_0(\xi)$, $\alpha_n(\xi)$, $\alpha_n^*(\xi)$, A_0, A_n, A_n^*, $n=1,2,3,\cdots$, to be determined, resulting in an infinite set of ordinary differential equations,

$$H_1(\xi)\alpha_0''+H_2(\xi)\frac{\alpha_0'}{\xi}-Bo\alpha_0=-H_4(\xi)\varepsilon_1-H_5(\xi)A_0, \tag{4.2.11}$$

$$H_1(\xi)\alpha_n''+H_2(\xi)\frac{\alpha_n'}{\xi}-\left[Bo\xi^2+n^2H_3(\xi)\right]\frac{\alpha_n}{\xi^2}=\left[n^2H_6(\xi)-H_5(\xi)\right]A_n, \tag{4.2.12}$$

$$H_1(\xi)\alpha_n^{*\prime\prime}+H_2(\xi)\frac{\alpha_n^{*\prime}}{\xi}-\left[Bo\xi^2+n^2H_3(\xi)\right]\frac{\alpha_n^*}{\xi^2}=\left[n^2H_6(\xi)-H_5(\xi)\right]A_n^*. \tag{4.2.13}$$

Compared to (3.2.14)–(3.2.16) in the model of the pinned contact line, we now have the extra forcing term coming from the first-order correction of the contact line. Equations (4.2.11)–(4.2.13) are linear second-order ordinary differential equations with singular variable coefficients, where $H_i(\xi)$, $i=1,2,\cdots,6$, are given by equations (3.2.6) and (4.2.5). We should determine the regular solutions of (4.2.11)–(4.2.13) subject to the corresponding boundary conditions, as well as the coefficients ε_1, A_0, A_n, A_n^*.

The Fourier series (4.2.9)–(4.2.10) and equations (4.2.6)–(4.2.8) provide the corresponding boundary conditions for equations (4.2.11)–(4.2.13),

$$\begin{aligned}\alpha_0(1)=&\frac{1}{2\pi}\int_{-\pi}^{\pi}\tilde{z}_p(1,\varphi)d\varphi,\\ \alpha_n(1)=&\frac{1}{\pi}\int_{-\pi}^{\pi}\tilde{z}_p(1,\varphi)\cos(n\varphi)d\varphi,\\ \alpha_n^*(1)=&\frac{1}{\pi}\int_{-\pi}^{\pi}\tilde{z}_p(1,\varphi)\sin(n\varphi)d\varphi,\end{aligned} \tag{4.2.14}$$

$$
\begin{aligned}
\alpha_0^{'}(1) =& \frac{1}{2\pi\cos^2\theta_e}\int_{-\pi}^{\pi}\tilde{z}_{p,\xi}(1,\varphi)d\varphi - \frac{\tan\theta_e}{\varepsilon_0}\left(A_0 - \frac{\varepsilon_1}{\varepsilon_0}\right),\\
\alpha_n^{'}(1) =& \frac{1}{\pi\cos^2\theta_e}\int_{-\pi}^{\pi}\tilde{z}_{p,\xi}(1,\varphi)\cos(n\varphi)d\varphi - \frac{\tan\theta_e}{\varepsilon_0}A_n,\\
\alpha_n^{*'}(1) =& \frac{1}{\pi\cos^2\theta_e}\int_{-\pi}^{\pi}\tilde{z}_{p,\xi}(1,\varphi)\sin(n\varphi)d\varphi - \frac{\tan\theta_e}{\varepsilon_0}A_n^*,
\end{aligned}
\tag{4.2.15}
$$

and a relation for ε_1,

$$
\varepsilon_1 = k_1\alpha_0^{'}(1) + k_2A_0 + k_3, \tag{4.2.16}
$$

where

$$
\begin{aligned}
k_1 =& \frac{2\varepsilon_0^2\cos^3\theta_e}{2\sin\theta_e\cos^2\theta_e - Bo\varepsilon_0},\\
k_2 =& \frac{2\varepsilon_0(\varepsilon_0 Bo - \sin^3\theta_e)}{\sin\theta_e\cos^2\theta_e - Bo\varepsilon_0},\\
k_3 =& -\frac{\varepsilon_0^2 Bo}{\pi(2\sin\theta_e\cos^2\theta_e - Bo\varepsilon_0)}\int_{-\pi}^{\pi}\int_0^1\tilde{z}_p(\xi,\varphi)\xi d\xi d\varphi.
\end{aligned}
\tag{4.2.17}
$$

In this section, we applied the perturbation method and Fourier decomposition to derive the first-order correction of the free surface of the droplet given by (4.2.11)–(4.2.13) subjected to the boundary conditions (4.2.14)–(4.2.15) and one equation (4.2.16).

4.3 Combined solution

In the current model, we should determine the position of the contact line as part of the solution. This means that, apart from the free surface of the droplet, the unknown coefficients A_0, A_n, A_n^* need to be determined. Due to the high similarity to the governing equation (3.2.14)–(3.2.16), we employ a methodology similar to the one used in the model of the pinned contact line to establish a general solution. Our approach involves seeking a regular series solution for $\xi \in [0, a]$ and a numerical solution within the interval $[a, 1]$, where $\xi = a \in (0, 1)$ is the patching point. We then combine both solutions by applying the patching conditions, which ensures that the combined solution is continuous and smooth at the patching point.

4.3.1 Series solution

We seek regular solutions to the governing equations (4.2.11)–(4.2.13), where $\xi = 0$ is the regular singular point, for small ξ. The power series approximations of the functions $H_i(\xi)$, where $i = 1, 2, 3, 4, 5, 6$, for small ξ read

$$
H_i(\xi) = \sum_{l=0}^{\infty} H_{il}\xi^l = H_{i0} + H_{i1}\xi + H_{i2}\xi^2 + \cdots, \tag{4.3.1}
$$

see equation (3.3.1).

The general solution of equation (4.2.11) is expected to have the form,

$$\alpha_0(\xi) = C_0\alpha_0^{(hr)}(\xi) + \varepsilon_1\alpha_0^{(p1)}(\xi) + A_0\alpha_0^{(p2)}(\xi), \tag{4.3.2}$$

where constants C_0, ε_1 and A_0 are to be determined. $\alpha_0^{(hr)}(\xi)$ is the regular solution of the corresponding homogeneous equation to (4.2.11), $H_1(\xi)\alpha_0^{''} + H_2(\xi)\dfrac{\alpha_0^{'}}{\xi} - Bo\alpha_0 = 0$, which was solved by applying the Frobenius method, see equation (3.3.11). $\varepsilon_1\alpha_0^{(p1)}(\xi) + A_0\alpha_0^{(p2)}(\xi)$ is a particular solution of (4.2.11). Here $\alpha_0^{(p1)}(\xi)$, which satisfies the equation (3.3.12),

$$H_1(\xi)\alpha_0^{''} + H_2(\xi)\frac{\alpha_0^{'}}{\xi} - Bo\alpha_0 = -H_4(\xi), \tag{4.3.3}$$

is sought in the form

$$\alpha_0^{(p1)}(\xi) = \sum_{m=0}^{\infty} f_{m0}\xi^{m+2}, \tag{4.3.4}$$

where the coefficients f_{m0} are given by the recurrence relation (3.3.14). Likewise, the function $\alpha_0^{(p2)}(\xi)$ is the solution of the equation

$$H_1(\xi)\alpha_0^{''} + H_2(\xi)\frac{\alpha_0^{'}}{\xi} - Bo\alpha_0 = -H_5(\xi), \tag{4.3.5}$$

and is searched in the form

$$\alpha_0^{(p2)}(\xi) = \sum_{m=0}^{\infty} f_{m0}^{*}\xi^{m+2}, \tag{4.3.6}$$

where the coefficients f_{m0}^{*} are given by

$$f_{m0}^{*} = \begin{cases} \dfrac{-1}{4}H_{50} & (m=0), \\ -\sum_{i=0}^{m-1}\dfrac{(i+2)(i+1)H_{1(m-i)} + (i+2)H_{2(m-i)} - H_{0(m-i)}}{(m+2)^2}f_{i0} & \\ -\dfrac{H_{5m}}{(m+2)^2} & (m>0). \end{cases} \tag{4.3.7}$$

Note that the coefficient $H_{0(m-i)}$ is given by equation (3.3.8),

$$H_{0(m-i)} = H_{0l} = \begin{cases} Bo, & l=2, \\ 0, & l\neq 2. \end{cases}$$

Thus, the general solution of equation (4.2.11) reads

$$\begin{aligned}\alpha_0(\xi) =& C_0\left(1+\tilde{k}_{10}\xi+\tilde{k}_{20}\xi^2+\tilde{k}_{30}\xi^3+\cdots\right)\\ &+\varepsilon_1\left(f_{00}\xi^2+f_{10}\xi^3 f_{20}\xi^4+\cdots\right)\\ &+A_0\left(f^*_{00}\xi^2+f^*_{10}\xi^3+f^*_{20}\xi^4+\cdots\right),\end{aligned} \tag{4.3.8}$$

where the coefficients in the round brackets can be found using the recurrence relations (3.3.10), (3.3.14), (4.3.7), and the constants C_0, A_0, ε_1 need to be determined by the patching conditions.

Since equations (4.2.12) and (4.2.13) are essentially identical ordinary differential equations, we will focus on detailing the solution procedure for (4.2.12). Obtaining the solution for equation (4.2.13) involves following the same process as for equation (4.2.12), with a change in notation. The general solution of (4.2.12) is written in

$$\alpha_n(\xi) = C_n\alpha_n^{(hr)}(\xi) + A_n\alpha_n^{(p)}(\xi), \tag{4.3.9}$$

where C_n and A_n are unknown constants that need to be determined. $\alpha_n^{(hr)}(\xi)$ is the regular solution of the homogeneous equation (3.2.15), which was solved using the Frobenius method, see equation (3.3.21). $A_n\alpha_n^{(p)}(\xi)$ is a particular solution, where function $\alpha_n^{(p)}(\xi)$ satisfies the equation

$$H_1(\xi)\alpha_n^{''} + H_2(\xi)\frac{\alpha_n^{'}}{\xi} - \left[Bo\xi^2 + n^2H_3(\xi)\right]\frac{\alpha_n}{\xi^2} = n^2H_6(\xi) - H_5(\xi). \tag{4.3.10}$$

The particular solution $\alpha_n^{(p)}$ is sought in the following form

$$\alpha_n^{(p)}(\xi) = \xi^2\sum_{m=0}^{\infty} f_{mn}\xi^m + \xi^n\log(\xi)\sum_{m=0}^{\infty} h_{mn}\xi^m. \tag{4.3.11}$$

The solution (4.3.11) is similar to the solution (3.3.17), where the latter term is replaced by another series, which starts from ξ^2. The derivatives are

$$\begin{aligned}\alpha_n^{'(p)} &= \sum_{m=0}^{\infty}(m+2)f_{mn}\xi^{m+1} + \sum_{m=0}^{\infty} h_{mn}\xi^{m+n-1} + \log(\xi)\sum_{m=0}^{\infty}(n+m)h_{mn}\xi^{m+n-1},\\ \alpha_n^{''(p)} &= \sum_{m=0}^{\infty}(m+2)(m+1)f_{mn}\xi^m + \sum_{m=0}^{\infty}(2n+2m-1)h_{mn}\xi^{m+n-2}\\ &\quad+\log(\xi)\sum_{m=0}^{\infty}(n+m)(n+m-1)h_{mn}\xi^{m+n-2}.\end{aligned}$$

When we substitute these series into equation (4.3.10), we should ensure that the logarithmic terms balance each other. Collecting all logarithmic terms and

dividing each term by ξ^n, we obtain

$$\log(\xi)\sum_{q}^{\infty}\left(\sum_{m=0}^{q}\left[(n+m)(n+m-1)H_{1(q-m)}+(n+m)H_{2(q-m)}-\tilde{H}_{3(q-m)}\right]h_{mn}\right)\xi^{q-2}, \tag{4.3.12}$$

where coefficients $\tilde{H}_{3(q-m)}$ are defined in equation (3.3.20),

$$\tilde{H}_{3(q-m)}=\tilde{H}_{3l}=\begin{cases}n^2H_{3l}, & l\neq 2,\\ n^2H_{3l}+Bo, & l=2.\end{cases}$$

In fact, the recurrence relation for h_{mn} is identical to (3.3.19). This implies that the logarithmic term can be represented by $K_n\log(\xi)\alpha_n^{(hr)}(\xi)$, where K_n is a constant to be determined. We will explain how to determine this constant later. Here, $\alpha_n^{(hr)}(\xi)=\xi^n\tilde{J}_n(\xi)$, where $\tilde{J}_n(\xi)=\sum_{m=0}^{\infty}\tilde{k}_{mn}\xi^m$, with $\tilde{k}_{0n}=1$. Hence, the particular solution is now expressed as

$$\alpha_n^{(p)}(\xi)=\sum_{m=0}^{\infty}f_{mn}\xi^{m+2}+K_n\log(\xi)\alpha_n^{(hr)}(\xi), \tag{4.3.13}$$

and its derivatives are

$$\begin{aligned}\alpha_n^{\prime(p)}(\xi)&=\sum_{m=0}^{\infty}(m+2)f_{mn}\xi^{m+1}+K_n\left(\log(\xi)\alpha_n^{\prime(hr)}(\xi)+\frac{1}{\xi}\alpha_n^{(hr)}(\xi)\right),\\ \alpha_n^{\prime\prime(p)}(\xi)&=\sum_{m=0}^{\infty}(m+2)(m+1)f_{mn}\xi^{m}\\ &\quad+K_n\left(\log(\xi)\alpha_n^{\prime\prime(hr)}(\xi)+\frac{2}{\xi}\alpha_n^{\prime(hr)}(\xi)-\frac{1}{\xi^2}\alpha_n^{(hr)}(\xi)\right).\end{aligned} \tag{4.3.14}$$

Substituting the series (4.3.13) and (4.3.14) into equation (4.3.10) and multiplying both sides by ξ^2, we find

$$\begin{aligned}&K_n\log(\xi)\left(\xi^2H_1(\xi)\alpha_n^{\prime\prime(hr)}(\xi)+\xi H_2(\xi)\alpha_n^{\prime(hr)}(\xi)-[Bo\xi^2+n^2H_3(\xi)]\alpha_n^{(hr)}(\xi)\right)\\ &\quad+K_n\left([H_2(\xi)-H_1(\xi)]\alpha_n^{(hr)}(\xi)+2\xi H_1(\xi)\alpha_n^{\prime(hr)}(\xi)\right)\\ &\quad+\sum_{m=0}^{\infty}(m+2)\left[(m+1)H_1(\xi)-H_2(\xi)\right]f_{mn}\xi^{m+2}\\ &\quad-\sum_{m=0}^{\infty}(n^2H_3(\xi)+Bo\xi^2)f_{mn}\xi^{m+2}=\xi^2[n^2H_6(\xi)-H_5(\xi)].\end{aligned} \tag{4.3.15}$$

The logarithmic term in (4.3.15) has no contribution since the expression in the

first round brackets is equal to zero. The second term on the left-hand side gives

$$\begin{aligned} & K_n\left([H_2(\xi)-H_1(\xi)]\alpha_n^{(hr)}(\xi)+2\xi H_1(\xi)\alpha_n^{\prime(hr)}(\xi)\right) \\ =&K_n\xi^n\sum_{q}^{\infty}\sum_{m=0}^{q}\left[H_{2(q-m)}-H_{1(q-m)}+2(n+m)H_{1(q-m)}\right]\tilde{k}_{mn}\xi^q \\ =&K_n\xi^n\sum_{q=0}^{\infty}s_{qn}\xi^q, \end{aligned} \tag{4.3.16}$$

where the recurrence relation for s_{qn} reads

$$s_{qn}=\begin{cases} 2n & q=0, \\ \sum_{m=0}^{q}\left[H_{2(q-m)}-H_{1(q-m)}+2(n+m)H_{1(q-m)}\right]\tilde{k}_{mn} & q\geq 1. \end{cases} \tag{4.3.17}$$

Hence, (4.3.15) becomes

$$\begin{aligned} &\sum_{q}^{\infty}\sum_{m=0}^{q}\left[(m+2)(m+1)H_{1(q-m))}+(m+2)H_{2(q-m))}-\tilde{H}_{3(q-m)}\right]f_{mn}\xi^{q+2} \\ &\qquad=\sum_{l=0}^{\infty}[n^2H_{6l}-H_{5l}]\xi^{l+2}-K_n\sum_{q=0}^{\infty}s_{qn}\xi^{q+n}. \end{aligned} \tag{4.3.18}$$

There are three series terms in the equation above. In the case of $n=1$, the third term in equation (4.3.18) starts from ξ, while the rest begin from ξ^2, requiring us to set $K_1=0$. For $n=2$, collecting the lowest terms on both sides yields

$$0\cdot f_{02}=4H_{60}-H_{50}-K_2s_{02}, \tag{4.3.19}$$

where $s_{02}=4$, see equation (4.3.17). Since the first derivative of the leading order of the droplet shape at the centre is zero, $F_{0,\xi}(0)=0$, see equation (2.4.18), we have

$$\begin{aligned} &H_5(0)=-2Bo[F_0(0)-1], \\ &H_6(0)=-\lim_{\xi\to 0}\frac{F_{0,\xi}}{\xi}=-F_{0,\xi\xi}(0)=-\frac{Bo[F_0(0)-1]}{2}, \end{aligned} \tag{4.3.20}$$

see (4.2.5), where the second derivative is calculated using the governing equation (3.2.4). Hence, we find $4H_{60}-H_{50}=0$, and consequently, $K_2=0$. Both K_1 and K_2 are zeros, meaning the logarithmic term is not present in the particular solution for the cases of $n=1$ and $n=2$. In other words, the particular solution

more precisely follows the expressions:

$$\alpha_n^{(p)}(\xi) = \begin{cases} \xi^2 \sum_{m=0}^{\infty} f_{mn}\xi^m & (n=1,2), \\ \xi^2 \sum_{m=0}^{\infty} f_{mn}\xi^m + K_n \log(\xi)\alpha_n^{(hr)}(\xi) & (n \geq 3). \end{cases} \tag{4.3.21}$$

For $n = 1$ and $n = 2$, we have the recurrence relations for the coefficients f_{m1} and f_{m2},

$$f_{m1} = \begin{cases} \dfrac{H_{60} - H_{50}}{3} & (m=0), \\ -\sum_{i=0}^{m-1} \dfrac{(i+2)(i+1)H_{1(m-i)} + (i+2)H_{2(m-i)} - \tilde{H}_{3(m-i)}}{(m+2)^2 - 1} f_{i1} & \\ +\dfrac{H_{6m} - H_{5m}}{(m+2)^2 - 1} & (m \geq 1). \end{cases} \tag{4.3.22}$$

$$f_{m2} = \begin{cases} 0 & (m=0), \\ \dfrac{4H_{61} - H_{51}}{5} & (m=1), \\ -\sum_{i=0}^{m-1} \dfrac{(i+2)(i+1)H_{1(m-i)} + (i+2)H_{2(m-i)} - \tilde{H}_{3(m-i)}}{(m+2)^2 - 4} f_{i2} & \\ +\dfrac{4H_{6m} - H_{5m}}{(m+2)^2 - 4} & (m > 1), \end{cases} \tag{4.3.23}$$

where coefficients $\tilde{H}_{3(m-i)}$ are defined in equation (3.3.20),

$$\tilde{H}_{3(m-i)} = \tilde{H}_{3l} = \begin{cases} n^2 H_{3l} & (l \neq 2), \\ n^2 H_{3l} + Bo & (l = 2). \end{cases}$$

Next, let us discuss how to determine the constant K_n in (4.3.21) for $n \geq 3$. To illustrate this process, we first take the $n = 3$ case as an example. Equating the coefficients of the lowest terms (ξ^2) on both sides, we find the equation for f_{03},

$$(2 + 2 - 3^2) f_{03} = 3^2 H_{60} - H_{50}.$$

We then collect the coefficients of ξ^3 terms,

$$(2H_{11} + 2H_{21} - 9H_{31}) f_{03} + 0 \cdot f_{13} = 9H_{61} - H_{51} - K_3 s_{03}.$$

Here $s_{03} = 6$, see equation (4.3.17), we can determine K_3 from this relation. We let $f_{13} = 0$ for simplicity. Collecting the coefficients of ξ^4 terms on both sides, we have

$$\begin{aligned}(2H_{12} + 2H_{22} - \tilde{H}_{32}) f_{03} + (6H_{11} + 3H_{21} - 9H_{31}) f_{13} + (12 + 4 - 9) f_{23} \\ = 9H_{62} - H_{52} - K_3 s_{13}.\end{aligned}$$

The coefficient f_{23} is determined from the above relation. Note that s_{13} is calculated using equation (4.3.17). In the $n = 3$ case, once K_3 is determined, the coefficients f_{m3}, where $m = 2, 3, 4, \cdots$, can be found. Extending to the n case, where $n \geq 3$, we obtain

$$f_{mn} = \begin{cases} \dfrac{n^2 H_{60} - H_{50}}{4 - n^2} & (m = 0), \\ -\sum_{i=0}^{m-1} \dfrac{(i^2 + 3i + 2)H_{1(m-i)} + (i+2)H_{2(m-i)} - \tilde{H}_{3(m-i)}}{(m+2)^2 - n^2} f_{in} \\ +\dfrac{n^2 H_{6m} - H_{5m}}{(m+2)^2 - n^2} & (0 < m < n-2), \\ 0 & (m = n-2), \\ -\sum_{i=0}^{m-1} \dfrac{(i^2 + 3i + 2)H_{1(m-i)} + (i+2)H_{2(m-i)} - \tilde{H}_{3(m-i)}}{(m+2)^2 - n^2} f_{in} \\ +\dfrac{n^2 H_{6m} - H_{5m}}{(m+2)^2 - n^2} - \dfrac{K_n s_{(m-n+2)n}}{(m+2)^2 - n^2} & (m > n-2). \end{cases} \tag{4.3.24}$$

In this case, we can easily find the coefficients $f_{0n}, \cdots, f_{(n-3)n}$. Collecting the coefficients of ξ^n terms, we get a relation to determine

$$\begin{aligned} K_n =& \frac{n^2 H_{6(n-2)} - H_{5(n-2)}}{2n} \\ & - \sum_{i=0}^{n-3} \frac{(i^2 + 3i + 2)H_{1(n-i-2)} + (i+2)H_{2(n-i-2)} - \tilde{H}_{3(n-i-2)}}{2n} f_{in}. \end{aligned} \tag{4.3.25}$$

The coefficient $f_{(n-2)n}$ is set to zero for simplicity. The coefficients $s_{(m-n+2)n}$ are calculated using the recurrence relation (4.3.17). Hence, the general solution of equation (4.2.12) for $n < 3$ reads

$$\begin{aligned} \alpha_n(\xi) =& C_n \xi^n \left(1 + \tilde{k}_{1n}\xi + \tilde{k}_{2n}\xi^2 + \tilde{k}_{3n}\xi^3 + \cdots\right) \\ & + A_n \left(f_{0n}\xi^2 + f_{1n}\xi^3 + f_{2n}\xi^4 + \cdots\right), \end{aligned} \tag{4.3.26}$$

while for $n \geq 3$ it takes the form

$$\begin{aligned} \alpha_n(\xi) =& C_n \xi^n \left(1 + \tilde{k}_{1n}\xi + \tilde{k}_{2n}\xi^2 + \tilde{k}_{3n}\xi^3 + \cdots\right) \\ & + A_n \left(f_{0n}\xi^2 + f_{1n}\xi^3 + f_{2n}\xi^4 + \cdots\right) \\ & + A_n K_n \xi^n \log(\xi) \left(1 + \tilde{k}_{1n}\xi + \tilde{k}_{2n}\xi^2 + \tilde{k}_{3n}\xi^3 + \cdots\right). \end{aligned} \tag{4.3.27}$$

Here, K_n is determined using equation (4.3.25), the coefficients in the round brackets are found through the recurrence relations (3.3.19), (4.3.22), (4.3.23), (4.3.24) and the unknown constant C_n, A_n should be determined by using the patching conditions at $\xi = a$.

4.3.2 Numerical solution and patching conditions

In this subsection, we explain the numerical solutions of equations (4.2.11)–(4.2.12). Subsequently, the combined solutions are obtained by matching the series and numerical solutions at the patching point $\xi = a$.

The boundary conditions for equation (4.2.11) can be written in terms of A_0 and ε_1,

$$\alpha_0(1) = d_{01} + e_{01}\varepsilon_1 + f_{01}A_0, \tag{4.3.28}$$

$$\alpha_0^{'}(1) = d_{02} + e_{02}\varepsilon_1 + f_{02}A_0, \tag{4.3.29}$$

where $e_{01} = 0$, $e_{02} = \tan\theta_e/\varepsilon_0^2$, $f_{01} = 0$, $f_{02} = -\tan\theta_e/\varepsilon_0$, and

$$\begin{aligned} d_{01} =& \frac{1}{2\pi}\int_{-\pi}^{\pi} \tilde{z}_p(1,\varphi)d\varphi, \\ d_{02} =& \frac{1}{2\pi\cos^2\theta_e}\int_{-\pi}^{\pi} \tilde{z}_{p,\xi}(1,\varphi)d\varphi, \end{aligned}$$

see equations (4.2.14) and (4.2.15). Hence, a numerical solution of equation (4.2.11) near the contact line $\xi = 1$ can be expressed as

$$\alpha_0(\xi) = \alpha_0^{(1)}(\xi) + \varepsilon_1\alpha_0^{(2)}(\xi) + A_0\alpha_0^{(3)}(\xi), \tag{4.3.30}$$

where constants A_0, ε_1 are to be determined. $\alpha_0^{(1)}(\xi)$ is the solution of the homogeneous equation corresponding to the governing equation (4.2.11), subject to the boundary conditions,

$$\alpha_0^{(1)}(1) = d_{01}, \qquad \alpha_{0,\xi}^{(1)}(1) = d_{02}. \tag{4.3.31}$$

$\alpha_0^{(2)}(\xi)$ satisfies equation (4.3.3) with the boundary conditions,

$$\alpha_0^{(2)}(1) = e_{01}, \qquad \alpha_{0,\xi}^{(2)}(1) = e_{02}, \tag{4.3.32}$$

while $\alpha_0^{(3)}(\xi)$ satisfies equation (4.3.5) subject to the boundary conditions,

$$\alpha_0^{(3)}(1) = f_{01}, \qquad \alpha_{0,\xi}^{(3)}(1) = f_{02}. \tag{4.3.33}$$

The functions $\alpha_0^{(1)}(\xi)$, $\alpha_0^{(2)}(\xi)$, $\alpha_0^{(3)}(\xi)$ are determined numerically by the fourth-order Runge–Kutta method. Using the series solution (4.3.8) and the numerical solution (4.3.30), the combined solution of (4.2.11) is represented by

$$\alpha_0 = \begin{cases} C_0\alpha_0^{(hr)}(\xi) + \varepsilon_1\alpha_0^{(p1)}(\xi) + A_0\alpha_0^{(p2)}(\xi) & (0 < \xi < a), \\ \alpha_0^{(1)}(\xi) + \varepsilon_1\alpha_0^{(2)}(\xi) + A_0\alpha_0^{(3)}(\xi) & (a < \xi < 1), \end{cases} \tag{4.3.34}$$

The patching conditions at $\xi = a$ read

$$\begin{aligned} C_0\alpha_0^{(hr)}(a) + A_0\left(\alpha_0^{(p2)}(a) - \alpha_0^{(3)}(a)\right) &= \alpha_0^{(1)}(a) + \varepsilon_1 M_{01}, \\ C_0\alpha_{0,\xi}^{(hr)}(a) + A_0\left(\alpha_{0,\xi}^{(p2)}(a) - \alpha_{0,\xi}^{(3)}(a)\right) &= \alpha_{0,\xi}^{(1)}(a) + \varepsilon_1 M_{02}, \end{aligned} \tag{4.3.35}$$

where $M_{01} = \alpha_0^{(2)}(a) - \alpha_0^{(p1)}(a)$, and $M_{02} = \alpha_{0,\xi}^{(2)}(a) - \alpha_{0,\xi}^{(p1)}(a)$. Using equations (4.2.16) and (4.3.29), ε_1 and $\alpha_0^{'}(1)$ can be written in terms of A_0 as

$$\varepsilon_1 = \tilde{l}_1 A_0 + \tilde{l}_2, \tag{4.3.36}$$

$$\alpha_0^{'}(1) = \tilde{l}_3 A_0 + \tilde{l}_4, \tag{4.3.37}$$

where the constant coefficients are

$$\tilde{l}_1 = \frac{k_2 + k_1 f_{02}}{1 - k_1 e_{02}}, \quad \tilde{l}_2 = \frac{k_3 + k_1 d_{02}}{1 - k_1 e_{02}}, \quad \tilde{l}_3 = \frac{f_{02} + e_{02} k_2}{1 - k_1 e_{02}}, \quad \tilde{l}_4 = \frac{d_{02} + e_{02} k_3}{1 - k_1 e_{02}},$$

and k_1, k_2 and k_3 are given by equation (4.2.17). Substituting (4.3.36) into the patching conditions (4.3.35), we obtain the system of equations with respect to two unknowns, C_0 and A_0,

$$\begin{aligned} C_0\alpha_0^{(hr)}(a) + A_0 M_{03} &= \alpha_0^{(1)}(a) + \tilde{l}_2 M_{01}, \\ C_0\alpha_{0,\xi}^{(hr)}(a) + A_0 M_{04} &= \alpha_{0,\xi}^{(1)}(a) + \tilde{l}_2 M_{02}. \end{aligned} \tag{4.3.38}$$

where $M_{03} = \alpha_0^{(p2)}(a) - \alpha_0^{(3)}(a) - \tilde{l}_1 M_{01}$ and $M_{04} = \alpha_{0,\xi}^{(p2)}(a) - \alpha_{0,\xi}^{(3)}(a) - \tilde{l}_1 M_{02}$. After solving (4.3.38) with respect to C_0 and A_0, the constant ε_1 is calculated using equation (4.3.36). Subsequently, the combined solution (4.3.34) is fully determined.

Similarly, the corresponding boundary conditions for equation (4.2.12) are expressed as

$$\begin{aligned} \alpha_n(1) &= d_{n1} + e_{n1} A_n, \\ \alpha_n^{'}(1) &= d_{n2} + e_{n2} A_n, \end{aligned} \tag{4.3.39}$$

where $e_{n1} = 0$, $e_{n2} = -\tan\theta_e/\varepsilon_0$, and

$$\begin{aligned} d_{n1} =& \frac{1}{\pi}\int_{-\pi}^{\pi} \tilde{z}_p(1,\varphi)\cos(n\varphi)d\varphi, \\ d_{n2} =& \frac{1}{\pi\cos^2\theta_e}\int_{-\pi}^{\pi} \tilde{z}_{p,\xi}(1,\varphi)\cos(n\varphi)d\varphi, \end{aligned}$$

so the numerical solution of equation (4.2.12) near $\xi = 1$ has the following form,

$$\alpha_n(\xi) = \alpha_n^{(1)}(\xi) + A_n\alpha_n^{(2)}(\xi). \tag{4.3.40}$$

Here A_n is to be determined. The function $\alpha_n^{(1)}(\xi)$ satisfies the homogeneous equation corresponding to equation (4.2.12) subject to the boundary conditions,

$$\alpha_n^{(1)}(1) = d_{n1}, \qquad \alpha_{n,\xi}^{(1)}(1) = d_{n2}, \tag{4.3.41}$$

while $\alpha_n^{(2)}(\xi)$ satisfies equation (4.3.10) subject to the boundary conditions

$$\alpha_n^{(2)}(1) = e_{n1}, \qquad \alpha_{n,\xi}^{(2)}(1) = e_{n2}. \tag{4.3.42}$$

The functions $\alpha_n^{(1)}(\xi)$ and $\alpha_n^{(2)}(\xi)$ are calculated by the fourth-order Runge–Kutta method. Thus, the combined solution of the governing equation (4.2.12) reads

$$\alpha_n(\xi) = \begin{cases} C_n\alpha_n^{(hr)}(\xi) + A_n\alpha_n^{(p)}(\xi) & (0 < \xi < a), \\ \alpha_n^{(1)}(\xi) + A_n\alpha_n^{(2)}(\xi) & (a < \xi < 1). \end{cases} \tag{4.3.43}$$

The patching conditions at $\xi = a$ give the following system with respect to C_n and A_n, $n \geq 1$,

$$\begin{aligned} C_n\alpha_n^{(hr)}(a) + A_n\left(\alpha_n^{(p)}(a) - \alpha_n^{(2)}(a)\right) &= \alpha_n^{(1)}(a), \\ C_n\alpha_{n,\xi}^{(hr)}(a) + A_n\left(\alpha_{n,\xi}^{(p)}(a) - \alpha_{n,\xi}^{(2)}(a)\right) &= \alpha_{n,\xi}^{(1)}(a). \end{aligned} \tag{4.3.44}$$

The first-order correction of the droplet shape and the contact line were sought in the form of the Fourier series, see equation (4.2.9) and (4.2.10). The coefficients $\alpha_0(\xi)$ and $\alpha_n(\xi)$ were presented by the equations (4.3.34) and (4.3.43). The unknown constants in (4.3.34) and (4.3.43) were determined by patching conditions (4.3.38) and (4.3.44).

4.4 Example

The deformation of the solid plate is assumed to follow the equation

$$\tilde{z}_p(\xi, \varphi) = A(t)\sum_{j=1}^{\infty} z_j(\xi)\cos j\varphi, \tag{4.4.1}$$

where $A(0) = 0$ and $A(t) > 0$ as $t > 0$. The function $A(t)$ is not specific here. The problem for the first-order correction of the droplet shape caused by the deformation of the solid surface (4.2.4)–(4.2.8) is linear with respect to $A(t)$. Therefore, we consider the problem for $A(t) = 1$ and multiply the final solution by $A(t)$ at the end of the analysis.

In this problem, we only need the combined solutions (4.3.43). Once we get the shape of the solid substrate, the numerical solution (4.3.40) is calculated, and then the corresponding constants C_n and A_n are determined by using the

patching conditions (4.3.44). We select a saddle shape $\tilde{z}_p(\xi, \varphi) = \xi^2 \cos 2\varphi$ and the inclined plate $\tilde{z}_p(\xi, \varphi) = \xi \cos \varphi$ as our examples.

When considering a solid surface given by $\tilde{z}_p(\xi, \varphi) = \xi^2 \cos 2\varphi$, the only solution for $n = 2$ is non-zero due to orthogonality properties. The resulting contact line is given by

$$\tilde{r}_c(\varphi) = 1 + \delta A_2 \cos(2\varphi), \tag{4.4.2}$$

see equation (4.2.10). By selecting the parameter $\delta = 0.2$, Figure 4.4.1 illustrates the original contact line represented by a black dashed line, while the position of the contact line after the deformation of the substrate is depicted by a blue line. On this saddle shape, the contact line is elongated in the y-direction and is shortened in the x-direction.

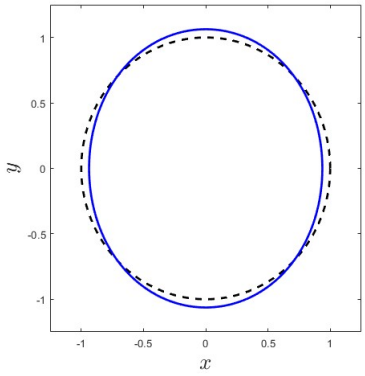

Figure 4.4.1: The contact line of a droplet on a saddle solid surface.

With a droplet volume of $V_0 = 0.1\,\text{mL}$ with $\theta_e = 70°$, the initial shape of the droplet is calculated in section 2.4. We determine the droplet shape on the saddle by combining the initial droplet shape with the first-order corrections, as visualised in Figure 4.4.2. Since this shape shows mirror symmetry along the $y = 0$ plane, we present the cross-sections in the polar angle φ from 0 to $\pi/2$. In the figures, blue represents the free surface of the droplet, while black represents the solid surface. The left column exhibits the cross-section in stretched coordinates, and to understand the actual droplet shape, we need to convert the coordinate system back into dimensionless cylindrical coordinates, presented in the right column of Figure 4.4.2. For enhanced visualisation and comprehension, a three-dimensional representation of the droplet placed on the saddle substrate is provided in Figure 4.4.3.

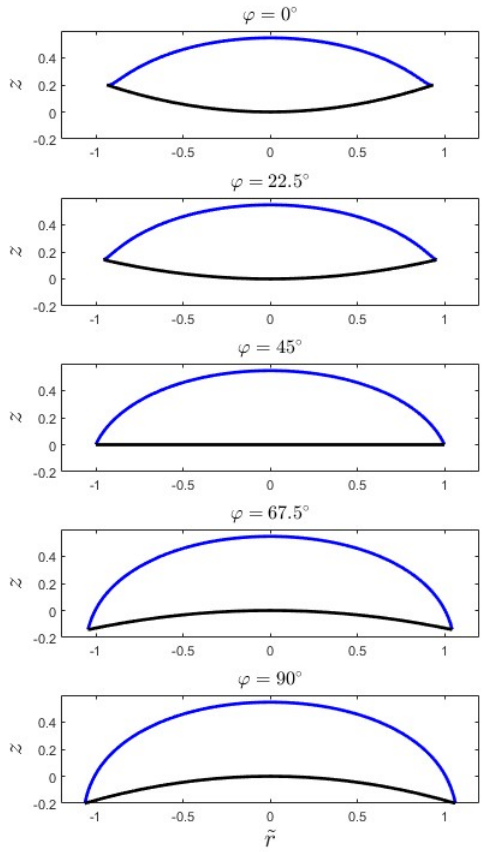

Figure 4.4.2: Cross-sections of a droplet sitting on a saddle-shaped surface at $\varphi = 0$, $\pi/8$, $\pi/4$, $3\pi/8$, and $\pi/2$ in the cylindrical coordinates.

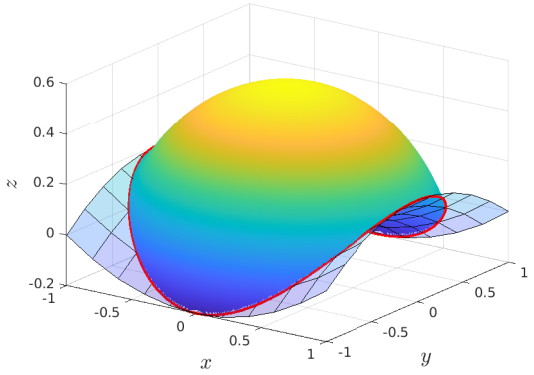

Figure 4.4.3: A three-dimensional droplet shape placed on a saddle shape.

Next, we consider the inclined plate described by the equation $\tilde{z}_p(\xi, \varphi) = \xi \cos\varphi$. Because of orthogonality properties, we only work with the $n = 1$ case. The constants C_1 and A_1 are calculated using patching conditions (4.3.44). The

contact line is given by

$$\tilde{r}_c(\varphi) = 1 + \delta A_1 \cos\varphi, \tag{4.4.3}$$

For $\delta = 0.004$, the contact line is visualised in Figure 4.4.4.

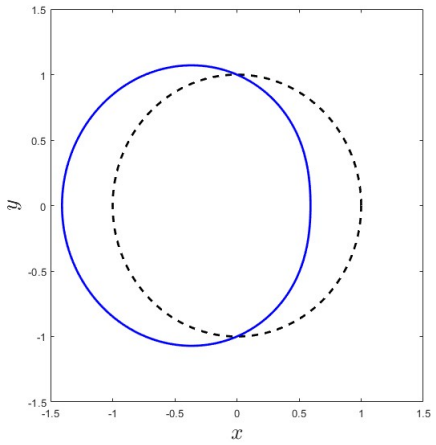

Figure 4.4.4: The contact line of a droplet on an inclined plate.

The droplet shape on the inclined plane is approximated by the sum of the initial axisymmetric droplet shape with the given droplet volume $V_0 = 0.1\,\mathrm{mL}$ and the first-order corrections. This shape exhibits symmetry along the x-axis, allowing us to visualise the cross-sections in the polar angle φ ranging from 0 to $\pi/2$, as shown in Figure 4.4.5. In the figures, the blue line represents the free surface of the droplet, while the black line signifies the solid surface. The left column provides cross-sections in stretched coordinates, while the right column shows the same in dimensionless cylindrical coordinates. For better comprehension, we also provide a three-dimensional representation in Figure 4.4.6.

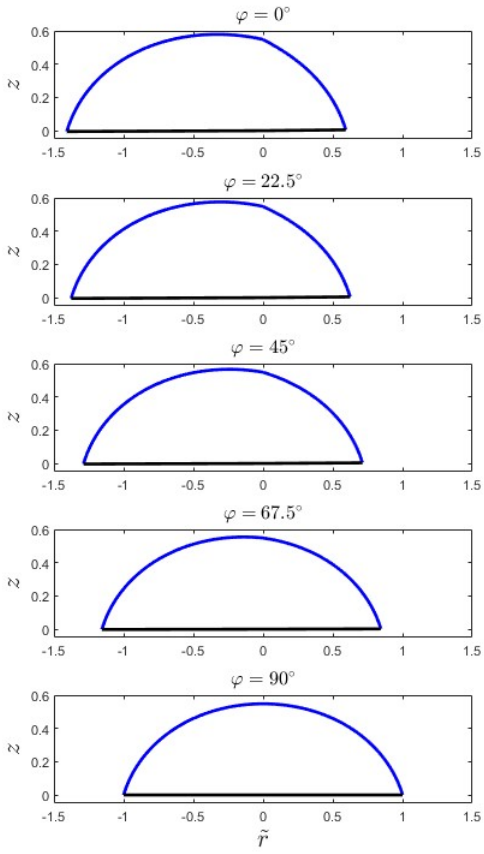

Figure 4.4.5: Cross-sections of a droplet placed on an inclined plate vary with the polar angle in the cylindrical coordinates. These sections correspond to the polar angle of $\varphi = 0$, $\pi/8$, $\pi/4$, $3\pi/8$, and $\pi/2$, respectively.

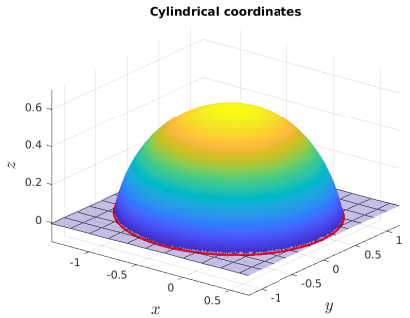

Figure 4.4.6: The three-dimensional figures of a droplet deposited on an inclined plate in the different coordinates. The left one is displayed in the stretched coordinates, while the right one is shown in the cylindrical coordinates.

In these two examples of solid surface deformations, the droplet shape on the saddle shape aligns with our expectations. On the other hand, the droplet shape on the inclined plate in the stretched coordinates has a significant deformation,

especially at $\varphi = 0$. Once converted back to the original coordinate, it looks like a symmetric shape but slides toward the downhill side.

5

Mixed contact line model with pinned and unpinned part of the contact line

Initially, an axisymmetric droplet with a given volume is placed on a flat and horizontal solid substrate. We investigate the three-dimensional droplet motion induced by slow deformations of the solid plate. A quasi-static approximation is applied to analyse the dynamic behaviour of the droplet, see section 2.5. In chapter 3, we considered the model of a pinned contact line, where the contact line was restricted from moving along the substrate. In chapter 4, we explored the model of a moving contact line, where the local contact angle is equal to the equilibrium contact angle at any time instant along the contact line. In the present chapter, we introduce the concept of hysteresis: if the current local contact angle θ_c falls within the range (θ_r, θ_a), with θ_r and θ_a being the receding and advancing contact angles, respectively, the contact line remains pinned; if the current local contact angle surpasses these limits, the contact line in the corresponding intervals of the contact line moves. Within the unpinned intervals of the contact line, we assume that the current local contact angle is equal to either the advancing or receding contact angle. Furthermore, the unpinned interval is unknown in advance and should be determined as part of the solution.

The problem is formulated in the stretched coordinates in this chapter since the contact line is non-circular, which follows the formulations in chapter 4. In the current model, we should determine parts of the contact line with different conditions for the current local contact angle. Note that both the position of the contact line and its subdivision into subintervals with different conditions on them are unknown in advance. The conditions of continuity and smoothness of the contact line are used to determine those subintervals of the contact line.

To solve the quasi-static problem in the stretched coordinates, we employ an asymptotic approach, assuming the substrate deformations are considerably smaller than the vertical dimension of the droplet. The first-order correction of the droplet shape is determined using the perturbation method, resulting in a mixed boundary value problem for a second-order partial differential equation

with variable coefficients. We then apply the Fourier decomposition to convert the problem into an infinite number of ordinary differential equations for the functions of the radial coordinate in the Fourier series.

These ordinary differential equations with the corresponding boundary conditions are solved independently. To find solutions for each of the ordinary differential equations, we employ a combination of series and numerical solutions, similar to the one in chapter 4. However, the condition of the contact angle in the current model becomes complicated since it varies across different subintervals. Substituting the general solution into the conditions on the contact angle, we obtain coupled integral equations. By solving numerically these integral equations, we obtain the entire contact line. Once the contact line is known, the free surface of the droplet can be calculated. At the end of the chapter, examples of a droplet on an inclined plate are provided to demonstrate the present model of the contact line motion.

5.1 Problem description

In this chapter, we utilise the quasi-static approximation, as detailed in section 2.5, to investigate the behaviour of a droplet placed on a solid surface, which varies in time t slowly, so the parameter time t is dropped off from our formulation in the following. The projection of the contact line is non-circular and is described by the equation $\tilde{r} = \tilde{r}_c(\varphi)$, where $\tilde{r}_c(\varphi) = r_c(\varphi)/R_0$, see section 2.3. Here R_0 is the contact radius of the initial droplet shape $\bar{\eta}_0(r)$, and the function $\tilde{r}_c(\varphi)$ is unknown in advance and should be determined. It is worth noting that in the current model, we consider the depinned or pinned timescale to occur at a faster rate than the substrate deformation.

The current model divides the contact line into two distinct parts: the pinned and unpinned regions. Within the pinned region, where the local contact angle is in between the receding, θ_r, and the advancing, θ_a, contact angles, the contact line remains stationary. In contrast, within the unpinned region, the local contact angle is considered constant, being equal to either the receding or advancing contact angle. Note that both receding θ_r and advancing θ_a contact angles are given constants. This model combines the previous two models in the way that $\theta_c = \theta_a$ or $\theta_c = \theta_r$ in the unpinned region and $\theta_r < \theta_c < \theta_a$ along the pinned region of the contact line. Additionally, the unpinned region consists of the advancing and receding parts. To simplify the problem, we consider each advancing and receding part to involve only one interval, which represents a droplet placed on an inclined plate, as observed in Berejnov and Thorne (2007) and Chou et al.

(2012). This results in the following representation

$$\tilde{r}_c(\varphi) = \begin{cases} \tilde{r}_{cr}(\varphi) & (\varphi_{r1} < \varphi < \varphi_{r2}), \\ \tilde{r}_{ca}(\varphi) & (\varphi_{a1} < \varphi < \varphi_{a2}), \\ 1 & (-\pi < \varphi < \varphi_{r1}, \quad \varphi_{r2} < \varphi < \varphi_{a1}, \quad \varphi_{a2} < \varphi < \pi), \end{cases} \tag{5.1.1}$$

as depicted in Figure 5.1.1.

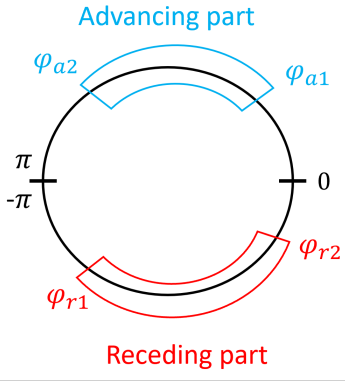

Figure 5.1.1: The unpinned region of the contact line involves the advancing and receding parts.

In equation (5.1.1), the unknown functions $\tilde{r}_{cr}(\varphi)$ and $\tilde{r}_{ca}(\varphi)$ represent the receding and advancing parts of the contact line, respectively, and should be determined. The parameters φ_{r1}, φ_{r2}, φ_{a1}, φ_{a2} are unknown as well. For convenience, we assume that $-\pi < \varphi_{r1} < \varphi_{r2} < \varphi_{a1} < \varphi_{a2} < \pi$. The contact line is supposed to be continuous and smooth, which provides the following equations,

$$\begin{aligned} \tilde{r}_{cr}(\varphi_{r1}) &= \tilde{r}_{cr}(\varphi_{r2}) = 1, \\ \tilde{r}'_{cr}(\varphi_{r1}) &= \tilde{r}'_{cr}(\varphi_{r2}) = 0, \end{aligned} \tag{5.1.2}$$

$$\begin{aligned} \tilde{r}_{ca}(\varphi_{a1}) &= \tilde{r}_{cr}(\varphi_{a2}) = 1, \\ \tilde{r}'_{ca}(\varphi_{a1}) &= \tilde{r}'_{cr}(\varphi_{a2}) = 0, \end{aligned} \tag{5.1.3}$$

to determine φ_{r1}, φ_{r2}, φ_{a1}, φ_{a2}. The contact angle along the contact line satisfies the relations,

$$\begin{aligned} \theta_c(1,\varphi) &= \theta_r \qquad (\varphi_{r1} < \varphi < \varphi_{r2}), \\ \theta_c(1,\varphi) &= \theta_a \qquad (\varphi_{a1} < \varphi < \varphi_{a2}), \\ \theta_r < \theta_c(1,\varphi) &< \theta_a \quad (-\pi < \varphi < \varphi_{r1}, \quad \varphi_{r2} < \varphi < \varphi_{a1}, \quad \varphi_{a2} < \varphi < \pi), \end{aligned} \tag{5.1.4}$$

where the contact line is at $\xi = 1$ in the stretched variables.

In the stretched coordinates $(\xi, \varphi, \tilde{z})$, the governing equation of the droplet

shape deposited on the substrate, $\tilde{z} = \delta Z(\xi, \varphi)$, where $\delta = Z_{sc}/B$ is the ratio of the vertical scale of the substrate to the thickness of the droplet, is described by

$$\frac{a_2 + \varepsilon^2 a_3}{(1 + \varepsilon^2 a_1)^{3/2}} = Bo[F(\xi, \varphi) - 1] \qquad (\xi < 1, -\pi < \varphi < \pi), \tag{5.1.5}$$

see equation (4.1.7), where Bo is Bond number, and the functions a_1, a_2, a_3 are given by equations (4.1.8). The governing equation (5.1.5) is accompanied by a boundary condition, which arises from the fact that the contact line is the intersection between the free surface of the droplet and the solid substrate,

$$F(1, \varphi) = \delta Z(1, \varphi), \tag{5.1.6}$$

see equation (4.1.9), and the condition of constant volume of the droplet

$$-\frac{1}{Bo}\int_{-\pi}^{\pi}\left(\frac{\varepsilon a_7 \tilde{r}_c(\varphi)}{\sqrt{1 + \varepsilon^2 a_4}}\right) d\varphi = \varepsilon\left(|S| - \delta\int_{-\pi}^{\pi}\int_{0}^{1} Z(\xi, \varphi)\tilde{r}_c^2(\varphi)\xi d\xi d\varphi\right) - \frac{V_0}{R_0^3}, \tag{5.1.7}$$

see equation (4.1.12), where $|S| = \frac{1}{2}\int_{-\pi}^{\pi} \tilde{r}_c^2(\varphi) d\varphi$, the functions a_4 and a_7 are given by equations (4.1.11) and (4.1.13). Equations (5.1.5)–(5.1.7) are identical to the equations in the model of the moving contact line since they are applied across the entire contact region, including the contact line, in the current model. The primary difference lies in the condition for the contact angle,

$$\cos\theta_c(1, \varphi) = \frac{1 + \varepsilon\varepsilon_z a_5}{\sqrt{1 + \varepsilon^2 a_4}\sqrt{1 + \varepsilon_z^2 a_6}}, \tag{5.1.8}$$

where $\theta_c(1, \varphi)$ follows the relations in (5.1.4), and the functions a_4, a_5, a_6 are given by equations (4.1.11).

This section formulated the problem in the dimensionless stretched coordinates. In the current model, we used the same equations as in chapter 4 except for the conditions on the contact angle presented in equations (5.1.8), where the unknown parameters φ_{r1}, φ_{r2}, φ_{a1}, φ_{a2} need to be determined using the conditions (5.1.2)–(5.1.3).

5.2 Asymptotic method

An approximate solution of problem (5.1.5)–(5.1.8) is sought for $\varepsilon = O(1)$ and $\delta \ll 1$ in the form,

$$\begin{aligned} F(\xi,\varphi) &= F_0(\xi) + \delta F_1(\xi,\varphi) + O(\delta^2), \\ \varepsilon &= \varepsilon_0 + \delta\varepsilon_1 + O(\delta^2), \\ \tilde{r}_c(\varphi) &= 1 + \delta g(\varphi) + O(\delta^2), \\ \theta_c(\varphi) &= \theta_e + \delta V(\varphi) + O(\delta^2). \end{aligned} \tag{5.2.1}$$

The model is the same as chapter 4, see equations (4.2.4)–(4.2.8), with the contact angle condition (4.2.7) replaced with

$$V(\varphi) = \begin{cases} V_1 & (\varphi_{a1} < \varphi < \varphi_{a2}), \\ V_2 & (\varphi_{r1} < \varphi < \varphi_{r2}), \\ v_0(\varphi) & (-\pi < \varphi < \varphi_{r1}, \quad \varphi_{r2} < \varphi < \varphi_{a1}, \quad \varphi_{a2} < \varphi < \pi), \end{cases} \tag{5.2.2}$$

where $V_1 = (\theta_a - \theta_e)/\delta$ and $V_2 = (\theta_r - \theta_e)/\delta$ are given constants, and the function $v_0(\varphi)$ is to be determined. Furthermore, the first-order correction of the contact line is given by

$$g(\varphi) = \begin{cases} g_a(\varphi) & (\varphi_{a1} < \varphi < \varphi_{a2}), \\ g_r(\varphi) & (\varphi_{r1} < \varphi < \varphi_{r2}), \\ 0 & (-\pi < \varphi < \varphi_{r1}, \quad \varphi_{r2} < \varphi < \varphi_{a1}, \quad \varphi_{a2} < \varphi < \pi). \end{cases} \tag{5.2.3}$$

where the functions $g_a(\varphi)$ and $g_r(\varphi)$ are to be determined. Note that the unknown parameters φ_{a1}, φ_{a2}, φ_{r1}, φ_{r2} should be determined using equations (5.1.2) and (5.1.3), which take the form for the first-order correction,

$$\begin{aligned} g_r(\varphi_{r1}) &= g_r(\varphi_{r2}) = 0, \\ g_r'(\varphi_{r1}) &= g_r'(\varphi_{r2}) = 0, \end{aligned} \tag{5.2.4}$$

$$\begin{aligned} g_a(\varphi_{a1}) &= g_r(\varphi_{a2}) = 0, \\ g_a'(\varphi_{a1}) &= g_a'(\varphi_{a2}) = 0. \end{aligned} \tag{5.2.5}$$

Thus, the first-order correction of the contact angle can be written in the form

$$F_{1,\xi}(1,\varphi) = \frac{\tilde{z}_{p,\xi}(1,\varphi)}{\cos^2\theta_e} + \frac{\tan\theta_e}{\varepsilon_0}\left(\frac{\varepsilon_1}{\varepsilon_0} - g(\varphi)\right) - \frac{V(\varphi)}{\varepsilon_0\cos^2\theta_e}. \tag{5.2.6}$$

This condition differs from (4.2.7) by the term with $V(\varphi)$, which was equal to zero in chapter 4.

The problem for the first-order correction of the free surface is given by (4.2.4)

subject to the boundary conditions (4.2.7), (5.2.6) with condition (4.2.8). The governing equation (4.2.4) is a second-order partial differential equation with variable coefficients. To separate variables ξ and φ, we employ the Fourier series

$$F_1(\xi,\varphi) = \alpha_0(\xi) + \sum_{n=1}^{\infty}[\alpha_n(\xi)\cos n\varphi + \alpha_n^*(\xi)\sin n\varphi], \tag{5.2.7}$$

$$g(\varphi) = A_0 + \sum_{n=1}^{\infty}[A_n\cos n\varphi + A_n^*\sin n\varphi], \tag{5.2.8}$$

$$V(\varphi) = B_0 + \sum_{n=1}^{\infty}[B_n\cos n\varphi + B_n^*\sin n\varphi], \tag{5.2.9}$$

where $\alpha_0(\xi)$, $\alpha_n(\xi)$, $\alpha_n^*(\xi)$, A_0, A_n, A_n^*, B_0, B_n, B_n^*, $n = 1, 2, 3, \cdots$, are to be determined, see equations (4.2.9)–(4.2.10). After applying the Fourier decomposition, the governing equations for the first-order correction of the droplet shape are presented in (4.2.11)–(4.2.13) subject to boundary condition (4.2.14) and one relation (4.2.16). The condition (5.2.6) gives

$$\begin{aligned}
\alpha_0^{'}(1) =& \frac{1}{2\pi\cos^2\theta_e}\int_{-\pi}^{\pi}\tilde{z}_{p,\xi}(1,\varphi)d\varphi - \frac{\tan\theta_e}{\varepsilon_0}\left(A_0 - \frac{\varepsilon_1}{\varepsilon_0}\right) - \frac{B_0}{\varepsilon_0\cos^2\theta_e},\\
\alpha_n^{'}(1) =& \frac{1}{\pi\cos^2\theta_e}\int_{-\pi}^{\pi}\tilde{z}_{p,\xi}(1,\varphi)\cos(n\varphi)d\varphi - \frac{\tan\theta_e}{\varepsilon_0}A_n - \frac{B_n}{\varepsilon_0\cos^2\theta_e},\\
\alpha_n^{*'}(1) =& \frac{1}{\pi\cos^2\theta_e}\int_{-\pi}^{\pi}\tilde{z}_{p,\xi}(1,\varphi)\sin(n\varphi)d\varphi - \frac{\tan\theta_e}{\varepsilon_0}A_n^* - \frac{B_n^*}{\varepsilon_0\cos^2\theta_e},
\end{aligned} \tag{5.2.10}$$

Since the functions $g(\varphi)$ and $V(\varphi)$ are not periodic over the entire interval $(-\pi,\pi)$ but in the small subintervals, we introduce the two Fourier series

$$g_a(\varphi) = I_0 + \sum_{m=1}^{\infty}\left[I_m\cos\left(\frac{m\pi}{L}(\varphi-\varphi_{a0})\right) + I_m^*\sin\left(\frac{m\pi}{L}(\varphi-\varphi_{a0})\right)\right] \quad (\varphi_{a1}<\varphi<\varphi_{a2}), \tag{5.2.11}$$

$$g_r(\varphi) = G_0 + \sum_{m=1}^{\infty}\left[G_m\cos\left(\frac{m\pi}{R}(\varphi-\varphi_{r0})\right) + G_m^*\sin\left(\frac{m\pi}{R}(\varphi-\varphi_{r0})\right)\right] \quad (\varphi_{r1}<\varphi<\varphi_{r2}), \tag{5.2.12}$$

where

$$\varphi_{a0} = (\varphi_{a1}+\varphi_{a2})/2, \qquad L = (\varphi_{a2}-\varphi_{a1})/2,$$
$$\varphi_{r0} = (\varphi_{r1}+\varphi_{r2})/2, \qquad R = (\varphi_{r2}-\varphi_{r1})/2.$$

We now seek the relation between $g(\varphi)$ and $g_a(\varphi)$, $g_r(\varphi)$. Integrating (5.2.3) by φ from $-\pi$ to π and using the Fourier series (5.2.8), (5.2.11), (5.2.12), we obtain

$$\begin{aligned}2\pi A_0 =& \int_{-\pi}^{\pi} g(\varphi)d\varphi = \int_{\varphi_{r1}}^{\varphi_{r2}} g_r(\varphi_0)d\varphi_0 + \int_{\varphi_{a1}}^{\varphi_{a2}} g_a(\varphi_0)d\varphi_0 \\ =& G_0\int_{-R}^{R} d\varphi_0 + \sum_{m=1}^{\infty}\left(G_m\int_{-R}^{R}\cos\frac{m\pi\varphi_0}{R}d\varphi_0 + G_m^*\int_{-R}^{R}\sin\frac{m\pi\varphi_0}{R}d\varphi_0\right) \\ &+ I_0\int_{-L}^{L} d\varphi_0 + \sum_{m=1}^{\infty}\left(I_m\int_{-L}^{L}\cos\frac{m\pi\varphi_0}{L}d\varphi_0 + I_m^*\int_{-L}^{L}\sin\frac{m\pi\varphi_0}{L}d\varphi_0\right).\end{aligned} \tag{5.2.13}$$

Multiplying equation (5.2.3) by $\cos n\varphi$ and integrating the resulting equation over φ from $-\pi$ to π, we obtain the relations between the coefficients A_n and the coefficients in the function G_a and G_r.

$$\begin{aligned}\pi A_n =& G_0\int_{-R}^{R}\cos n(\varphi_0+\varphi_{r0})d\varphi_0 + I_0\int_{-L}^{L}\cos n(\varphi_0+\varphi_{a0})d\varphi_0 \\ &+ \sum_{m=1}^{\infty} G_m\int_{-R}^{R}\cos\frac{m\pi\varphi_0}{R}\cos n(\varphi_0+\varphi_{r0})d\varphi_0 \\ &+ \sum_{m=1}^{\infty} G_m^*\int_{-R}^{R}\sin\frac{m\pi\varphi_0}{R}\cos n(\varphi_0+\varphi_{r0})d\varphi_0 \\ &+ \sum_{m=1}^{\infty} I_m\int_{-L}^{L}\cos\frac{m\pi\varphi_0}{L}\cos n(\varphi_0+\varphi_{a0})d\varphi_0 \\ &+ \sum_{m=1}^{\infty} I_m^*\int_{-L}^{L}\sin\frac{m\pi\varphi_0}{L}\cos n(\varphi_0+\varphi_{a0})d\varphi_0\end{aligned} \tag{5.2.14}$$

Similarly, using the same operation but replacing $\cos n\varphi$ by $\sin n\varphi$, we have the relations between A_n^* and the coefficients in the function G_a and G_r. This resulting relation is similar to equation (5.2.14), where A_n is replaced by A_n^*, $\cos n(\varphi_0+\varphi_{r0})$ by $\sin n(\varphi_0+\varphi_{r0})$ and $\cos n(\varphi_0+\varphi_{a0})$ by $\sin n(\varphi_0+\varphi_{a0})$.

The series (5.2.8), (5.2.11) and (5.2.12) are truncated to n term. We introduce the vectors

$$\vec{A} = (A_0, A_1, A_2, A_3, \cdots, A_n, A_1^*, A_2^*, A_3^*, \cdots, A_n^*)^\intercal, \tag{5.2.15}$$

$$\vec{G}_r = (G_0, G_1, G_2, G_3, \cdots, G_n, G_1^*, G_2^*, G_3^*, \cdots, G_n^*)^\intercal, \tag{5.2.16}$$

$$\vec{G}_a = (I_0, I_1, I_2, I_3, \cdots, I_n, I_1^*, I_2^*, I_3^*, \cdots, I_n^*)^\intercal, \tag{5.2.17}$$

of length $2n+1$, so the above equations can be represented by

$$\vec{A} = \frac{\mathbb{C}_1}{\pi}\vec{G}_a + \frac{\mathbb{C}_2}{\pi}\vec{G}_r. \tag{5.2.18}$$

Here $\mathbb{C}_1$ and $\mathbb{C}_2$ are $(2n+1)\times(2n+1)$ matrices. The components of the matrix $\mathbb{C}_1$ are

$$C_{ij}=\begin{cases}\frac{1}{2}\int_{-L}^{L}\cos\left(\dfrac{(j-1)\pi}{L}(\varphi_0+\varphi_{a0})\right)d\varphi_0 \qquad (i=1,\quad 1\le j\le n+1),\\ \frac{1}{2}\int_{-L}^{L}\sin\left(\dfrac{(j-n-1)\pi}{L}(\varphi_0+\varphi_{a0})\right)d\varphi_0\\ \qquad (i=1,\quad n+1<j\le 2n+1),\\ \int_{-L}^{L}\cos\left((i-1)(\varphi_0+\varphi_{a0})\right)\cos\left(\dfrac{(j-1)\pi\varphi_0}{L}\right)d\varphi_0\\ \qquad (2\le i\le n+1,\quad 1\le j\le n+1),\\ \int_{-L}^{L}\cos\left((i-1)(\varphi_0+\varphi_{a0})\right)\sin\left(\dfrac{(j-n-1)\pi\varphi_0}{L}\right)d\varphi_0\\ \qquad (2\le i\le n+1,\quad n+1<j\le 2n+1),\\ \int_{-L}^{L}\sin\left((i-n-1)(\varphi_0+\varphi_{a0})\right)\cos\left(\dfrac{(j-1)\pi\varphi_0}{L}\right)d\varphi_0\\ \qquad (n+1<i\le 2n+1,\quad 1\le j\le n+1),\\ \int_{-L}^{L}\sin\left((i-n-1)(\varphi_0+\varphi_{a0})\right)\sin\left(\dfrac{(j-n-1)\pi\varphi_0}{L}\right)d\varphi_0\\ \qquad (n+1<i\le 2n+1,\quad n+1<j\le 2n+1).\end{cases}\tag{5.2.19}$$

The components of the matrix $\mathbb{C}_2$ are similar to those of $\mathbb{C}_1$, where R is replaced by L and φ_{a0} by φ_{r0}, For the function v_0 in (5.2.2), we should solve the governing equations (4.2.11)–(4.2.13) along with the corresponding conditions (4.2.14) (4.2.16) and (5.2.10) to determine the functions $\alpha_0(\xi)$, $\alpha_n(\xi)$, $\alpha_n^*(\xi)$ and the constants A_0, A_n, A_n^*, B_0, B_n, B_n^* together. However, the condition (5.2.10) is reliant on the functions $g_a(\varphi)$, $g_r(\varphi)$, which are components of the contact line $g(\varphi)$. Therefore, we need to employ equation (5.2.18), which establishes the coefficient relationship between the functions $g_a(\varphi)$, $g_r(\varphi)$, and $g(\varphi)$.

5.3 General solution

The governing equations (4.2.11)–(4.2.13) subject to the corresponding boundary conditions (4.2.14) with the condition (4.2.16) keep the same forms, so we can obtain the solution, which combines series and numerical solutions at the patching point, by following the previous work.

The series solution of equation (4.2.11) for small ξ reads

$$\alpha_0(\xi)=C_0\alpha_0^{(hr)}(\xi)+\varepsilon_1\alpha_0^{(p1)}(\xi)+A_0\alpha_0^{(p2)}(\xi),\tag{5.3.1}$$

see equation (4.3.8). The numerical solution of equation (4.2.11) near the contact

line $\xi = 1$ is presented in the form

$$\alpha_0(\xi) = \alpha_0(1)\alpha_0^{(1)}(\xi) + \alpha_0^{'}(1)\alpha_0^{(2)}(\xi) + \varepsilon_1\alpha_0^{(3)}(\xi) + A_0\alpha_0^{(4)}(\xi), \tag{5.3.2}$$

where $\alpha_0(1)$ is given by (4.2.14), $\alpha_0^{'}(1)$ and ε_1 are to be determined using the patching conditions, and the unknown A_0 needs to be determined using the boundary condition (5.2.6). $\alpha_0^{(1)}(\xi)$ and $\alpha_0^{(2)}(\xi)$ satisfy the homogeneous equation associated to (4.2.11) subject to the boundary conditions,

$$\begin{cases} \alpha_0^{(1)}(1) = 1, \\ \alpha_{0,\xi}^{(1)}(1) = 0, \end{cases} \quad \begin{cases} \alpha_0^{(2)}(1) = 0, \\ \alpha_{0,\xi}^{(2)}(1) = 1. \end{cases} \tag{5.3.3}$$

$\alpha_0^{(3)}(\xi)$ satisfies equation (4.3.3) with the boundary condition,

$$\alpha_0^{(3)}(1) = 0, \qquad \alpha_{0,\xi}^{(3)}(1) = 0. \tag{5.3.4}$$

$\alpha_0^{(4)}(\xi)$ is the solution of (4.3.5) subject to the boundary condition,

$$\alpha_0^{(4)}(1) = 0, \qquad \alpha_{0,\xi}^{(4)}(1) = 0. \tag{5.3.5}$$

Here $\alpha_0^{(1)}(\xi)$, $\alpha_0^{(2)}(\xi)$, $\alpha_0^{(3)}(\xi)$, $\alpha_0^{(4)}(\xi)$ are obtained numerically by the fourth-order Runge–Kutta method. Hence, the combined solution of (4.2.11) reads

$$\alpha_0(\xi) = \begin{cases} C_0\alpha_0^{(hr)}(\xi) + \varepsilon_1\alpha_0^{(p1)}(\xi) + A_0\alpha_0^{(p2)}(\xi) & (0 < \xi < a), \\ \alpha_0(1)\alpha_0^{(1)}(\xi) + \alpha_0^{'}(1)\alpha_0^{(2)}(\xi) + \varepsilon_1\alpha_0^{(3)}(\xi) + A_0\alpha_0^{(4)}(\xi) & (a < \xi < 1), \end{cases} \tag{5.3.6}$$

where a is the patching point. At $\xi = a$, the series solution (5.3.1) is equal to the numerical solution (5.3.2), and their derivatives are equal as well, called the patching conditions. These conditions and equation (4.2.16) for ε_1 give the system of equations with respect to C_0 and $\alpha_0^{'}(1)$,

$$\begin{aligned} \alpha_0^{(hr)}(a)C_0 - M_{03}\alpha_0^{'}(1) &= M_{05}A_0 + \alpha_0^{(1)}(a)\alpha_0(1) + M_{01}k_3, \\ \alpha_{0,\xi}^{(hr)}(a)C_0 - M_{04}\alpha_0^{'}(1) &= M_{06}A_0 + \alpha_{0,\xi}^{(1)}(a)\alpha_0(1) + M_{02}k_3, \end{aligned} \tag{5.3.7}$$

where k_1, k_2, k_3 are given by equations (4.2.17), $M_{01} = \alpha_0^{(3)}(a) - \alpha_0^{(p1)}(a)$, $M_{02} = \alpha_{0,\xi}^{(3)}(a) - \alpha_{0,\xi}^{(p1)}(a)$, $M_{03} = \alpha_0^{(2)}(a) + M_{01}k_1$, $M_{04} = \alpha_{0,\xi}^{(2)}(a) + M_{02}k_1$, $M_{05} = \alpha_0^{(4)}(a) - \alpha_0^{(p2)}(a) + M_{01}k_2$, and $M_{06} = \alpha_{0,\xi}^{(4)}(a) - \alpha_{0,\xi}^{(p2)}(a) + M_{02}k_2$. Note that A_0 is to be determined.

Similarly, the series solution of (4.2.12) for small ξ is represented by

$$\alpha_n(\xi) = C_n\alpha_n^{(hr)}(\xi) + A_n\alpha_n^{(p)}(\xi), \tag{5.3.8}$$

see equations (4.3.26) and (4.3.27), while the numerical solution of (4.2.12) near $\xi = 1$ takes the form

$$\alpha_n(\xi) = \alpha_n(1)\alpha_n^{(1)}(\xi) + \alpha_n^{'}(1)\alpha_n^{(2)}(\xi) + A_n\alpha_n^{(3)}(\xi). \tag{5.3.9}$$

Here, $\alpha_n(1)$ is calculated using (4.2.14), $\alpha_n^{'}(1)$ and A_n are to be determined. The functions $\alpha_n^{(1)}(\xi)$ and $\alpha_n^{(2)}(\xi)$ satisfy the homogeneous equation corresponding to (4.2.12) subject to the boundary conditions,

$$\begin{cases} \alpha_n^{(1)}(1) = 1, \\ \alpha_{n,\xi}^{(1)}(1) = 0, \end{cases} \quad \begin{cases} \alpha_n^{(2)}(1) = 0, \\ \alpha_{n,\xi}^{(2)}(1) = 1, \end{cases} \tag{5.3.10}$$

$\alpha_n^{(3)}(\xi)$ satisfies equation (4.3.10) with the boundary conditions,

$$\alpha_n^{(3)}(1) = 0, \qquad \alpha_{n,\xi}^{(3)}(1) = 0. \tag{5.3.11}$$

The combined solution of equation (4.2.12) reads

$$\alpha_n(\xi) = \begin{cases} C_n\alpha_n^{(hr)}(\xi) + A_n\alpha_n^{(p)}(\xi), & (0 < \xi < a), \\ \alpha_n(1)\alpha_n^{(1)}(\xi) + \alpha_n^{'}(1)\alpha_n^{(2)}(\xi) + A_n\alpha_n^{(3)}(\xi) & (a < \xi < 1). \end{cases} \tag{5.3.12}$$

The patching conditions at $\xi = a$ provide the following system with respect to C_n and $\alpha_n^{'}(1)$,

$$\begin{aligned} \alpha_n^{(hr)}(a)C_n - \alpha_n^{(2)}(a)\alpha_n^{'}(1) &= M_{n1}A_n + \alpha_n^{(1)}(a)\alpha_n(1), \\ \alpha_{n,\xi}^{(hr)}(a)C_n - \alpha_{n,\xi}^{(2)}(a)\alpha_n^{'}(1) &= M_{n2}A_n + \alpha_{n,\xi}^{(1)}(a)\alpha_n(1). \end{aligned} \tag{5.3.13}$$

where $M_{n1} = \alpha_n^{(3)}(a) - \alpha_n^{(p)}(a)$ and $M_{n2} = \alpha_{n,\xi}^{(3)}(a) - \alpha_{n,\xi}^{(p)}(a)$. Note that A_n is to be determined. Likewise, the combined solution of (4.2.13) is obtained by following the same process as for equation (4.2.12), with a change in notation,

$$\alpha_n^*(\xi) = \begin{cases} C_n^*\alpha_n^{*(hr)}(\xi) + A_n^*\alpha_n^{*(p)}(\xi) & (0 < \xi < a), \\ \alpha_n^*(1)\alpha_n^{*(1)}(\xi) + \alpha_n^{*'}(1)\alpha_n^{*(2)}(\xi) + A_n^*\alpha_n^{*(3)}(\xi) & (a < \xi < 1). \end{cases} \tag{5.3.14}$$

The patching conditions of equation (4.2.13) read

$$\begin{aligned} \alpha_n^{*(hr)}(a)C_n^* - \alpha_n^{*(2)}(a)\alpha_n^{*'}(1) &= M_{n1}^*A_n^* + \alpha_n^{*(1)}(a)\alpha_n^*(1), \\ \alpha_{n,\xi}^{*(hr)}(a)C_n^* - \alpha_{n,\xi}^{*(2)}(a)\alpha_n^{*'}(1) &= M_{n2}^*A_n^* + \alpha_{n,\xi}^{*(1)}(a)\alpha_n^*(1). \end{aligned} \tag{5.3.15}$$

The systems of equations (5.3.7), (5.3.13), (5.3.15) can be rewritten in the following forms:

$$\begin{aligned} C_0 =& D_{01}A_0 + E_{01}\alpha_0(1) + F_{01}, \\ \alpha_0^{'}(1) =& D_{02}A_0 + E_{02}\alpha_0(1) + F_{02}, \end{aligned} \tag{5.3.16}$$

$$\begin{aligned} C_n =& D_{n1}A_n + E_{n1}\alpha_n(1), \\ \alpha_n^{'}(1) =& D_{n2}A_n + E_{n2}\alpha_n(1), \end{aligned} \tag{5.3.17}$$

$$\begin{aligned} C_n^* =& D_{n1}^*A_n^* + E_{n1}^*\alpha_n^*(1), \\ \alpha_n^{*'}(1) =& D_{n2}^*A_n^* + E_{n2}^*\alpha_n^*(1). \end{aligned} \tag{5.3.18}$$

The constants D_{01}, E_{01}, F_{01}, D_{02}, E_{02}, F_{02} are given by the following equations:

$$\begin{aligned} D_{01} =& \frac{M_{05}M_{04} - M_{06}M_{03}}{\alpha_0^{(hr)}(a)M_{04} - \alpha_{0,\xi}^{(hr)}(a)M_{03}}, \\ E_{01} =& \frac{\alpha_0^{(1)}(a)M_{04} - \alpha_{0,\xi}^{(1)}(a)M_{03}}{\alpha_0^{(hr)}(a)M_{04} - \alpha_{0,\xi}^{(hr)}(a)M_{03}}, \\ F_{01} =& \frac{M_{01}M_{04} - M_{02}M_{03}}{\alpha_0^{(hr)}(a)M_{04} - \alpha_{0,\xi}^{(hr)}(a)M_{03}}k_3, \\ D_{02} =& \frac{M_{05}\alpha_{0,\xi}^{(hr)}(a) - M_{06}\alpha_0^{(hr)}(a)}{M_{04}\alpha_0^{(hr)}(a) - M_{03}\alpha_{0,\xi}^{(hr)}(a)} \\ E_{02} =& \frac{\alpha_0^{(1)}(a)\alpha_{0,\xi}^{(hr)}(a) - \alpha_{0,\xi}^{(1)}(a)\alpha_0^{(hr)}(a)}{M_{04}\alpha_0^{(hr)}(a) - M_{03}\alpha_{0,\xi}^{(hr)}(a)}, \\ F_{02} =& \frac{M_{01}\alpha_{0,\xi}^{(hr)}(a) - M_{02}\alpha_0^{(hr)}(a)}{M_{04}\alpha_0^{(hr)}(a) - M_{03}\alpha_{0,\xi}^{(hr)}(a)}k_3. \end{aligned} \tag{5.3.19}$$

The constants D_{n1}, E_{n1}, D_{n2}, E_{n2} are given by

$$\begin{aligned} D_{n1} =& \frac{M_{n1}\alpha_{n,\xi}^{(2)}(a) - M_{n2}\alpha_n^{(2)}(a)}{\alpha_n^{(hr)}(a)\alpha_{n,\xi}^{(2)}(a) - \alpha_{n,\xi}^{(hr)}(a)\alpha_n^{(2)}(a)}, \\ E_{n1} =& \frac{\alpha_n^{(1)}(a)\alpha_{n,\xi}^{(2)}(a) - \alpha_{n,\xi}^{(1)}(a)\alpha_n^{(2)}(a)}{\alpha_n^{(hr)}(a)\alpha_{n,\xi}^{(2)}(a) - \alpha_{n,\xi}^{(hr)}(a)\alpha_n^{(2)}(a)}, \\ D_{n2} =& \frac{M_{n1}\alpha_{n,\xi}^{(hr)}(a) - M_{n2}\alpha_n^{(hr)}(a)}{\alpha_{n,\xi}^{(2)}(a)\alpha_n^{(hr)}(a) - \alpha_n^{(2)}(a)\alpha_{n,\xi}^{(hr)}(a)}, \\ E_{n2} =& \frac{\alpha_n^{(1)}(a)\alpha_{n,\xi}^{(hr)}(a) - \alpha_{n,\xi}^{(1)}(a)\alpha_n^{(hr)}(a)}{\alpha_{n,\xi}^{(2)}(a)\alpha_n^{(hr)}(a) - \alpha_n^{(2)}(a)\alpha_{n,\xi}^{(hr)}(a)}. \end{aligned} \tag{5.3.20}$$

The constants D_{n1}^*, E_{n1}^*, D_{n2}^*, E_{n2}^* are similar to the above equations (5.3.20) but with the addition of the symbol *.

Substituting (5.3.16) into (4.2.16), the parameter ε_1 take the form

$$\varepsilon_1 = (k_1 D_{02} + k_2)A_0 + k_1 E_{02}\alpha_0(1) + k_1 F_{02} + k_3. \tag{5.3.21}$$

Substituting (5.3.16)–(5.3.18) into (5.2.7), the first derivative of the first-order corrections of the droplet shape at $\xi = 1$ is expressed as

$$\begin{aligned} F_{1,\xi}(1,\varphi) =& D_{02}A_0 + E_{02}\alpha_0(1) + F_{02} + \sum_{n=1}^{\infty}[D_{n2}A_n + E_{n2}\alpha_n(1)]\cos n\varphi \\ &+ \sum_{n=1}^{\infty}[D^*_{n2}A^*_n + E^*_{n2}\alpha^*_n(1)]\sin n\varphi. \end{aligned} \tag{5.3.22}$$

Substituting (5.3.21)–(5.3.22) into the boundary conditions (5.2.6), we obtain

$$\begin{aligned} g_a(\varphi) + (\lambda_1 D_{02} - \lambda_2)A_0 + \lambda_1 \sum_{n=1}^{\infty}[D_{n2}A_n \cos n\varphi + D^*_{n2}A^*_n \sin n\varphi] \\ = \tilde{F}_a(\varphi) \qquad (\varphi \in (\varphi_{a1}, \varphi_{a2})), \end{aligned} \tag{5.3.23}$$

$$\begin{aligned} g_r(\varphi) + (\lambda_1 D_{02} - \lambda_2)A_0 + \lambda_1 \sum_{n=1}^{\infty}[D_{n2}A_n \cos n\varphi + D^*_{n2}A^*_n \sin n\varphi] \\ = \tilde{F}_r(\varphi) \qquad (\varphi \in (\varphi_{r1}, \varphi_{r2})), \end{aligned} \tag{5.3.24}$$

where $\lambda_1 = \dfrac{\varepsilon_0}{\tan\theta_e}$, $\lambda_2 = \dfrac{k_1 D_{02} + k_2}{\varepsilon_0}$, and the functions $\tilde{F}_a(\varphi)$ and $\tilde{F}_r(\varphi)$ are

$$\begin{aligned} \tilde{F}_a(\varphi) =& \frac{1}{\varepsilon_0}(k_1 E_{02}\alpha_0(1) + k_1 F_{02} + k_3) - \frac{V_1}{\sin\theta_e \cos\theta_e} + \frac{\varepsilon_0 \tilde{z}_{p,\xi}(1,\varphi)}{\sin\theta_e \cos\theta_e} \\ &- \lambda_1 \left(E_{02}\alpha_0(1) + F_{02} + \sum_{n=1}^{\infty}[E_{n2}\alpha_n(1)\cos n\varphi + E^*_{n2}\alpha^*_n(1)\sin n\varphi] \right), \\ \tilde{F}_r(\varphi) =& \frac{1}{\varepsilon_0}(k_1 E_{02}\alpha_0(1) + k_1 F_{02} + k_3) - \frac{V_2}{\sin\theta_e \cos\theta_e} + \frac{\varepsilon_0 \tilde{z}_{p,\xi}(1,\varphi)}{\sin\theta_e \cos\theta_e} \\ &- \lambda_1 \left(E_{02}\alpha_0(1) + F_{02} + \sum_{n=1}^{\infty}[E_{n2}\alpha_n(1)\cos n\varphi + E^*_{n2}\alpha^*_n(1)\sin n\varphi] \right). \end{aligned} \tag{5.3.25}$$

It is convenient to express $\tilde{F}_a(\varphi)$ and $\tilde{F}_r(\varphi)$ in the form of the Fourier Series

$$\tilde{F}_a(\varphi) = F_{a0} + \sum_{n=1}^{\infty}\left[F_{an}\cos n\varphi + F^*_{an}\sin n\varphi\right], \tag{5.3.26}$$

$$\tilde{F}_r(\varphi) = F_{r0} + \sum_{n=1}^{\infty}\left[F_{rn}\cos n\varphi + F^*_{rn}\sin n\varphi\right]. \tag{5.3.27}$$

The series (5.3.26) and (5.3.27) are truncated to n term. We introduce the vectors

$$\vec{F}_a = (F_{a0}, F_{a1}, F_{a2}, F_{a3}, \cdots, F_{an}, F^*_{a1}, F^*_{a2}, F^*_{a3}, \cdots, F^*_{an})^\intercal, \tag{5.3.28}$$

$$\vec{F}_r = (F_{r0}, F_{r1}, F_{r2}, F_{r3}, \cdots, F_{rn}, F^*_{r1}, F^*_{r2}, F^*_{r3}, \cdots, F^*_{rn})^\intercal, \tag{5.3.29}$$

of length $2n+1$. Integrating equation (5.3.23) in φ from φ_{a1} to φ_{a2}, we get the first equation. Next, multiplying (5.3.23) by $\cos\left(\frac{m\pi}{L}(\varphi-\varphi_{a0})\right)$, where $m \geq 1$, on both sides and integrating the resulting equation in φ from φ_{a1} to φ_{a2}, we obtain the second equation. Likewise, multiplying (5.3.23) by $\sin\left(\frac{m\pi}{L}(\varphi-\varphi_{a0})\right)$ on both sides and integrating the resulting equation in φ from φ_{a1} to φ_{a2}, we get the third equation. The sum of these three integral equations is represented by

$$\mathbb{D}_1\vec{G}_a + \lambda_1\mathbb{E}_1\vec{A} - \lambda_2\mathbb{F}_1\vec{A} = \mathbb{M}_1\vec{F}_a, \tag{5.3.30}$$

where the vectors $\vec{A}$, $\vec{G}_a$, $\vec{F}_a$ are given by (5.2.15), (5.2.17), (5.3.28), and $\mathbb{D}_1$, $\mathbb{E}_1$, $\mathbb{F}_1$, $\mathbb{M}_1$ are $(2n+1)\times(2n+1)$ matrices. $\mathbb{D}_1$ is a diagonal matrix with the element,

$$D_{ii} = \begin{cases} 2L & (i=1), \\ L & (i \neq 1). \end{cases} \tag{5.3.31}$$

The matrix $\mathbb{M}_1$ has the elements,

$$M_{ij} = \begin{cases} \int_{-L}^{L} \cos\left((j-1)(\varphi_0+\varphi_{a0})\right)\cos\left(\dfrac{(i-1)\pi\varphi_0}{L}\right)d\varphi_0 \\ \qquad (1 \leq j \leq n+1, \quad 1 \leq i \leq n+1), \\ \int_{-L}^{L} \cos\left((j-1)(\varphi_0+\varphi_{a0})\right)\sin\left(\dfrac{(i-n-1)\pi\varphi_0}{L}\right)d\varphi_0 \\ \qquad (1 \leq j \leq n+1, \quad n+1 < i \leq 2n+1), \\ \int_{-L}^{L} \sin\left((j-n-1)(\varphi_0+\varphi_{a0})\right)\cos\left(\dfrac{(i-1)\pi\varphi_0}{L}\right)d\varphi_0 \\ \qquad (n+1 < j \leq 2n+1, \quad 1 \leq i \leq n+1), \\ \int_{-L}^{L} \sin\left((j-n-1)(\varphi_0+\varphi_{a0})\right)\sin\left(\dfrac{(i-n-1)\pi\varphi_0}{L}\right)d\varphi_0 \\ \qquad (n+1 < j \leq 2n+1, \quad n+1 < i \leq 2n+1). \end{cases} \tag{5.3.32}$$

The components of the matrix $\mathbb{E}_1$ are

$$E_{ij} = \begin{cases} D_{(j-1)2}M_{ij} & (1 \leq j \leq n+1), \\ D^*_{(j-1)2}M_{ij} & (n+1 < j \leq 2n+1). \end{cases} \tag{5.3.33}$$

The matrix $\mathbb{F}_1$ has the elements,

$$F_{ij} = \begin{cases} \int_{-L}^{L} \cos\left(\frac{(j-1)\pi}{L}\varphi_0\right) d\varphi_0 & (i=1, \quad 1 \le j \le n+1), \\ \int_{-L}^{L} \sin\left(\frac{(j-n-1)\pi}{L}\varphi_0\right) d\varphi_0 & (i=1, \quad n+1 < j \le 2n+1), \\ 0 & (i \ne 1). \end{cases} \tag{5.3.34}$$

Likewise, employing the similar operation on the equation (5.3.24), where φ_{a0} is replaced by φ_{r0}, φ_{a1} by φ_{r1}, and φ_{a2} by φ_{r2}, we obtain

$$\mathbb{D}_2\vec{G}_r + \lambda_1\mathbb{E}_2\vec{A} - \lambda_2\mathbb{F}_2\vec{A} = \mathbb{M}_2\vec{F}_r, \tag{5.3.35}$$

where the vectors $\vec{G}_r$ and $\vec{F}_r$ are given by (5.2.16) and (5.3.29). $\mathbb{D}_2$, $\mathbb{E}_2$, $\mathbb{F}_2$, $\mathbb{M}_2$ are $(2n+1)\times(2n+1)$ matrices. The components of the matrix $\mathbb{D}_2$ are similar to those of $\mathbb{D}_1$, where L is replaced by R,

$$\tilde{D}_{ii} = \begin{cases} 2R & (i=1), \\ R & (i \ne 1). \end{cases} \tag{5.3.36}$$

The matrix $\mathbb{M}_2$ has the elements

$$\tilde{M}_{ij} = \begin{cases} \int_{-R}^{R} \cos\left((j-1)(\varphi_0+\varphi_{r0})\right) \cos\left(\dfrac{(i-1)\pi\varphi_0}{R}\right) d\varphi_0 \\ \qquad (1 \le j \le n+1, \quad 1 \le i \le n+1), \\ \int_{-R}^{R} \cos\left((j-1)(\varphi_0+\varphi_{r0})\right) \sin\left(\dfrac{(i-n-1)\pi\varphi_0}{R}\right) d\varphi_0 \\ \qquad (1 \le j \le n+1, \quad n+1 < i \le 2n+1), \\ \int_{-R}^{R} \sin\left((j-n-1)(\varphi_0+\varphi_{r0})\right) \cos\left(\dfrac{(i-1)\pi\varphi_0}{R}\right) d\varphi_0 \\ \qquad (n+1 < j \le 2n+1, \quad 1 \le i \le n+1), \\ \int_{-R}^{R} \sin\left((j-n-1)(\varphi_0+\varphi_{r0})\right) \sin\left(\dfrac{(i-n-1)\pi\varphi_0}{R}\right) d\varphi_0 \\ \qquad (n+1 < j \le 2n+1, \quad n+1 < i \le 2n+1). \end{cases} \tag{5.3.37}$$

The components of the matrix $\mathbb{E}_2$ are

$$\tilde{E}_{ij} = \begin{cases} D_{(j-1)^2}\tilde{M}_{ij} & (1 \le j \le n+1), \\ D^*_{(j-1)^2}\tilde{M}_{ij} & (n+1 < j \le 2n+1). \end{cases} \tag{5.3.38}$$

The matrix $\mathbb{F}_2$ has the elements,

$$\tilde{F}_{ij} = \begin{cases} \int_{-R}^{R} \cos\left(\frac{(j-1)\pi}{R}\varphi_0\right) d\varphi_0 & (i=1, \quad 1 \le j \le n+1), \\ \int_{-R}^{R} \sin\left(\frac{(j-n-1)\pi}{R}\varphi_0\right) d\varphi_0 & (i=1, \quad n+1 < j \le 2n+1), \\ 0 & (i \ne 1). \end{cases} \tag{5.3.39}$$

Substituting the relation (5.2.18) into (5.3.30) and (5.3.35), we obtain

$$\begin{aligned} \left(\mathbb{D}_1 + \frac{\lambda_1}{\pi}\mathbb{E}_1 \cdot \mathbb{C}_1 - \frac{\lambda_2}{\pi}\mathbb{F}_1 \cdot \mathbb{C}_1\right)\vec{G}_a + \left(\frac{\lambda_1}{\pi}\mathbb{E}_1 \cdot \mathbb{C}_2 - \frac{\lambda_2}{\pi}\mathbb{F}_1 \cdot \mathbb{C}_2\right)\vec{G}_r = \vec{F}_a, \\ \left(\frac{\lambda_1}{\pi}\mathbb{E}_2 \cdot \mathbb{C}_1 - \frac{\lambda_2}{\pi}\mathbb{F}_2 \cdot \mathbb{C}_1\right)\vec{G}_a + \left(\mathbb{D}_2 + \frac{\lambda_1}{\pi}\mathbb{E}_2 \cdot \mathbb{C}_2 - \frac{\lambda_2}{\pi}\mathbb{F}_2 \cdot \mathbb{C}_2\right)\vec{G}_r = \vec{F}_r. \end{aligned} \tag{5.3.40}$$

Once the vectors $\vec{G}_a$ and $\vec{G}_r$ is determined by solving the coupled equations (5.3.40), $\vec{A}$ is calculated using relation (5.2.18), the combined solutions (5.3.6), (5.3.12) and (5.3.14) are fully determined.

In the current model, the droplet shape in the first-order correction was searched in the form of the Fourier series, see equation (5.2.7), where the coefficients $\alpha_0(\xi)$, $\alpha_n(\xi)$ and $\alpha_n^*(\xi)$ were presented by the combined solutions (5.3.6), (5.3.12) and (5.3.14). In the unpinned part of the contact line, the position of the contact line presented by the Fourier series (5.2.11) and (5.2.12) was part of the solution.

5.4 Examples

In practice, before a droplet moves on a solid substrate, we can observe the phenomenon where the droplet deforms (elongates or shortens) but still stays on the substrate. This occurs because only either advancing or receding is overcome, rather than both simultaneously. Thus, we provide examples where only receding occurs in the contact line and both advancing and receding occur. In the first case, the change in the local contact angle only encounters the receding contact angle. In the second case, however, the change exceeds the interval between the advancing and receding contact angles. Both advancing and receding contact angles are considered constants and are given in our examples.

We consider only one interval on each advancing and receding part of the contact line, so we take a droplet on an inclined plate as an example. The deformation of the solid plate is described by

$$Z(\xi, \varphi) = A(t)\xi\cos\varphi, \tag{5.4.1}$$

where $A(0) = 0$ and $A(t) > 0$ as $t > 0$. This problem is linear concerning the

function $A(t)$. Therefore, we can address the problem by setting $A(t) = 1$ during the solution process and multiplying the obtained solution by $A(t)$ at the end of the analysis.

5.4.1 Simplified unpinned part of the contact line

We first consider a simplified case with a single receding region only. The receding part of the contact line is within the interval $(\varphi_{r1}, \varphi_{r2})$. The shape of the droplet and contact line are assumed to be symmetric along the x–axis, which gives $\varphi_{r2} = R = -\varphi_{r1}$. The first-order correction of the contact line is described by

$$g(\varphi) = \begin{cases} g_r(\varphi) & (-R < \varphi < R), \\ 0 & (-\pi < \varphi < -R, \quad R < \varphi < \pi), \end{cases} \tag{5.4.2}$$

In the current example, where $G_a = 0$, there is no more coupling. Thus, (5.3.40) can be sorted exactly, yielding

$$\vec{G}_r = \left(\mathbb{D}_2 + \frac{\lambda_1}{\pi} \mathbb{E}_2 \cdot \mathbb{C}_2 - \frac{\lambda_2}{\pi} \mathbb{F}_2 \cdot \mathbb{C}_2 \right)^{-1} \vec{F}_r. \tag{5.4.3}$$

In this example, we set the receding contact angle to $\theta_r = 65°$. Although this value does not have a specific physical interpretation, it is suitable for illustrating the results in this particular case. The value of R is obtained by satisfying the conditions (5.2.4) and (5.2.5), resulting in $R = 0.91$. The two-dimensional contact line is computed using (5.4.3) and (5.2.18), depicted by a blue line in Figure 5.4.1, while the original contact line is denoted by a black dashed line. As expected, the contact line recedes in the region $\varphi \in (-R, R)$ only.

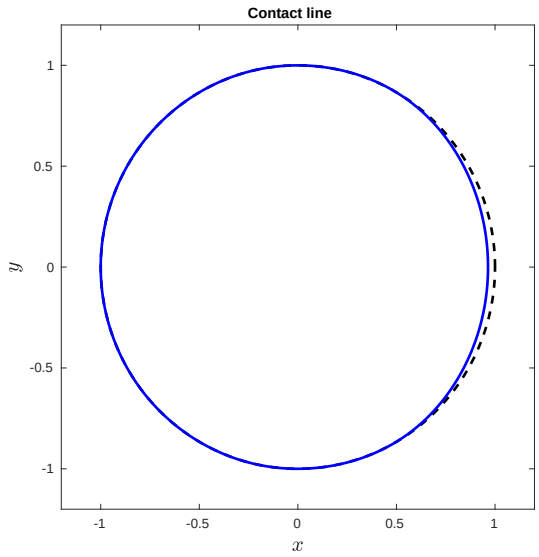

Figure 5.4.1: The two-dimensional contact line motion in the simplified case.

Once we obtain the first-order correction of the contact line, the first-order correction of the droplet shape is determined by equations (5.3.6) and (5.3.12). The leading order term of the droplet shape is obtained from section 2.4 for $V_0 = 0.1\,\mathrm{mL}$ and $\theta_e = 70°$. A three-dimensional figure of the droplet shape is shown in Figure 5.4.2.

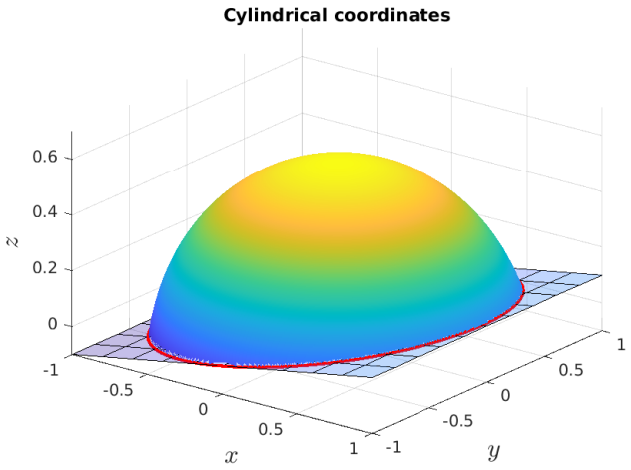

Figure 5.4.2: A three-dimensional droplet shape with only one unpinned part.

The change of droplet shape primarily occurs in the polar angle $\varphi \in (-R, R)$ corresponding to the position of the contact line. The droplet shape is continuous and smooth at $\varphi = R$ since the contact line satisfies the conditions (5.2.4) and (5.2.5). However, to ensure the validity of this truncated approximation, we need to verify it using equation (3.4.12), depicted in Figure 5.4.3. We observe that D_e is small for $N > 8$. For this example, we opt for $N = 15$ to truncate the Fourier series of the droplet.

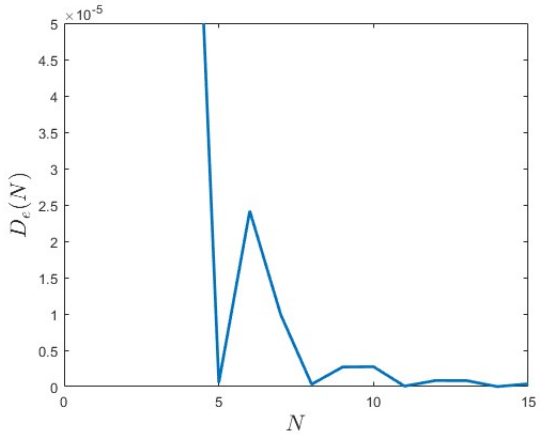

Figure 5.4.3: The difference of the droplet shape with the values of N.

Furthermore, we need to examine the contact angle $\theta_c(\varphi)$ for $\varphi \in (-\pi, \pi)$.

The contact angle remains constant and equal to the receding contact angle in the unpinned part, while it exhibits variation along the pinned part of the contact line. The Fourier wiggles are evident in the pinned region. To address this, we increase the value of N to 200, resulting in the disappearance of these wiggles, as shown in Figure 5.4.5.

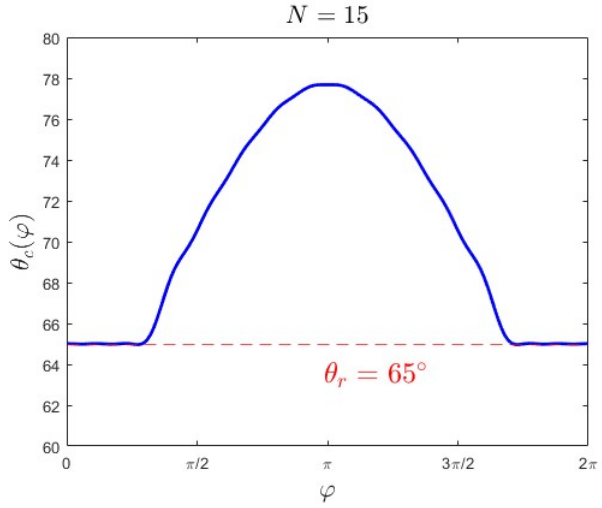

Figure 5.4.4: The contact angle along the contact line in the simplified case.

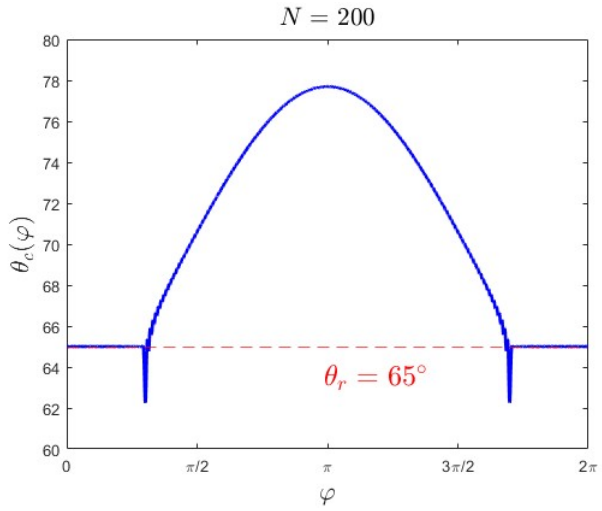

Figure 5.4.5: The contact angle along the contact line in the simplified case.

5.4.2 Two regions of the unpinned part

Consider the contact line is symmetric along x–axis. The unpinned part of the contact line is assumed to be split into the advancing and receding parts, which are represented by the functions $g_r(\varphi)$ and $g_a(\varphi)$. Thus, the first-order correction

of the contact line is described by

$$g(\varphi) = \begin{cases} 0 & (-\pi + L < \varphi < -R, \quad R < \varphi < \pi - L), \\ g_r(\varphi) & (-R < \varphi < R), \\ g_a(\varphi) & (-\pi < \varphi < -\pi + L, \quad \pi - L < \varphi < \pi), \end{cases} \tag{5.4.4}$$

and the first-order correction of the contact angle reads

$$V(\varphi) = \begin{cases} v_0(\varphi) & (-\pi + L < \varphi < -R, \quad R < \varphi < \pi - L), \\ V_2 & (-R < \varphi < R), \\ V_1 & (-\pi < \varphi < -\pi + L, \quad \pi - L < \varphi < \pi), \end{cases} \tag{5.4.5}$$

where the constants $V_2 = \dfrac{\theta_r - \theta_e}{\delta}$, $V_1 = \dfrac{\theta_a - \theta_e}{\delta}$, and the functions $v_0(\varphi)$, $g_r(\varphi)$, $g_a(\varphi)$ are to be determined. In this example, we set the equilibrium contact angle $\theta_e = 70°$, receding contact angle $\theta_r = 65°$ and advancing contact angle $\theta_r = 75°$.

The coefficients of $g_r(\varphi)$ and $g_a(\varphi)$ are determined by solving the coupled equations (5.3.40), where $R = L = 0.91$ is obtained using the conditions (5.2.4) and (5.2.4). Subsequently, the coefficients of the first-order correction of the contact line are computed using (5.2.18). The resulting contact line is illustrated in Figure 5.4.6, represented by a blue line, while the initial contact line is depicted as a dashed line.

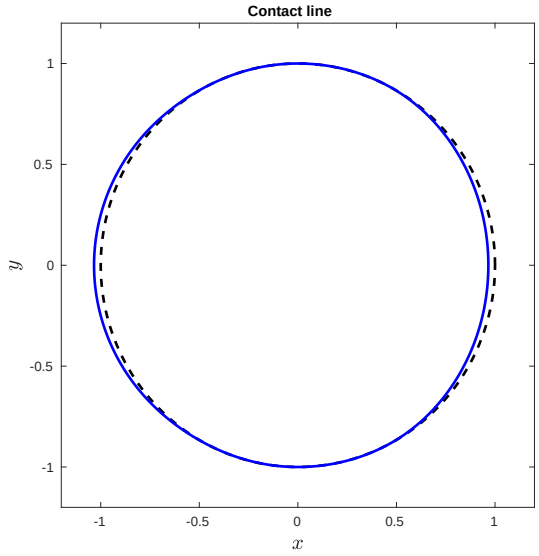

Figure 5.4.6: A two-dimensional contact line motion with advancing and receding regions on an inclined plate.

Next, the first-order correction of the droplet shape is obtained from (5.3.6) and (5.3.12). By adding the leading order term, where $V_0 = 0.1\,\mathrm{mL}$, we obtain

the droplet shape presented in the stretched coordinates. Converting the system back to the dimensionless cylindrical coordinates, the droplet shape on the inclined plate is shown in Figure 5.4.7. The primary change in the droplet shape corresponds to the change in the position of the contact line.

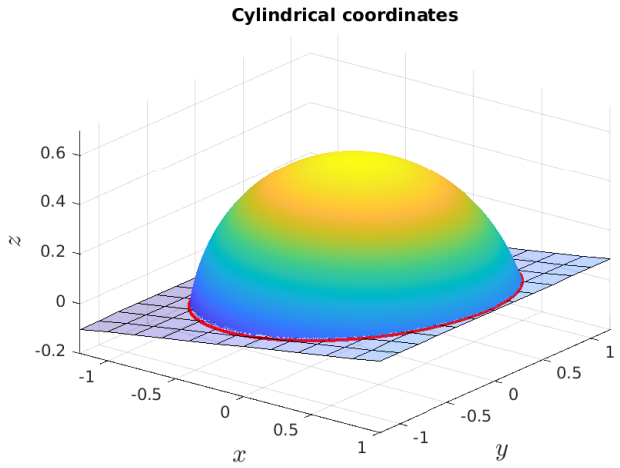

Figure 5.4.7: A three-dimensional droplet shape on an inclined plate.

To validate the accuracy of this truncated approximation, we use (3.4.12) to verify, as shown in Figure 5.4.8. We observe that D_e is small for $N > 9$. Hence, we adopt $N = 20$ to truncate the Fourier series of the droplet in this example.

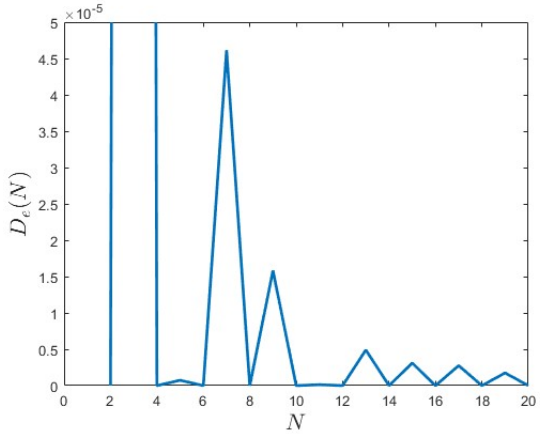

Figure 5.4.8: The change in the droplet shape D_e varies with N.

The first-order correction of the contact angle is calculated using (5.2.6), presented in Figure 5.4.9. The contact angle remains constant and equal to the receding or advancing contact angle in the unpinned part. There is variation in the contact angle along the pinned region of the contact line. The Fourier wiggles in the pinned region are observed at the $N = 20$ case. These wiggles disappear when a truncated number of $N = 200$ is employed

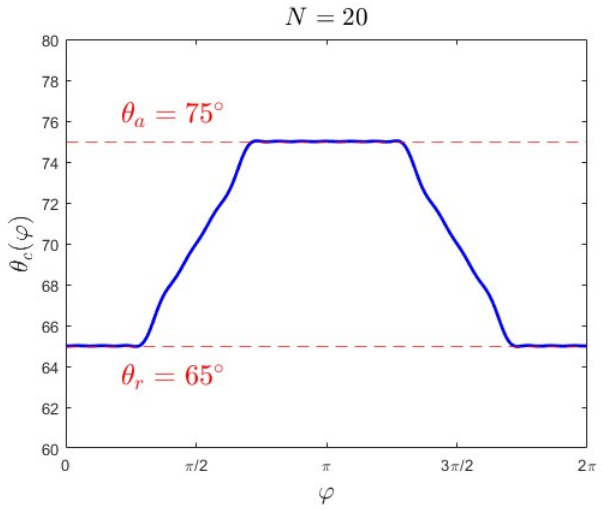

Figure 5.4.9: The contact angle $\theta_c(\varphi)$ along the contact line.

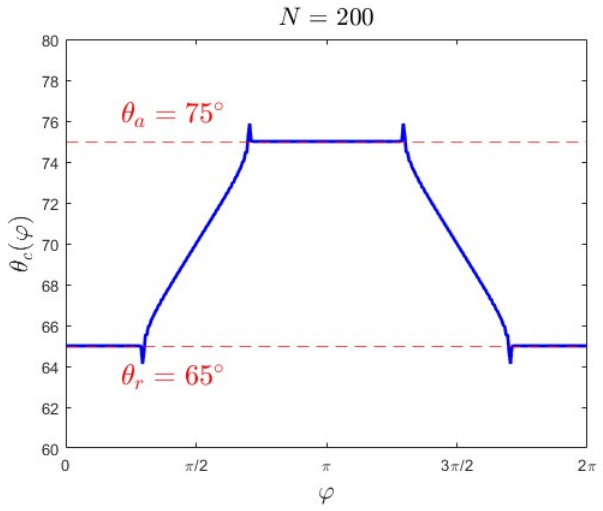

Figure 5.4.10: The contact angle $\theta_c(\varphi)$ along the contact line for choosing $N = 200$.

6

Cox-Voinov model of contact line motion

An axisymmetric droplet of a given volume, initially sitting on a flat and horizontal solid surface, undergoes motion due to deformations in the solid substrate. The investigation focuses on slow deformations, allowing the application of the quasi-static approximation, see section 2.5. The Cox-Voinov equation is employed as the contact line model in this chapter. This equation establishes a relation between the current local contact angle θ_c and the normal velocity of the contact line. In this model, the problem is solved in two steps at each time instant. The first step is to determine the droplet shape together with the contact angle at the time instant for the known contact line, similar to the analysis performed in chapter 3, while the second step is to find the new position of the contact line at the next time instant using the Cox-Voinov formula for the local speed of the contact line.

In the current model, the problem is formulated in the stretched coordinates as the contact line is not circular and moves. Due to the high similarity of the present problem to the problem in the model of the pinned contact line, the focus in this chapter is on the definition of the normal velocity of the contact line and its formulation in the stretched coordinates.

We apply a similar methodology as in previous chapters to asymptotically solve the quasi-static problem in the current model. The perturbation method, by considering the small change of the solid substrate in its vertical direction compared to the height of the droplet, and Fourier decomposition are used. The resulting governing equation for the first-order correction of the droplet shape is presented as a set of second-order ordinary differential equations with variables coefficient, which is identical to the one in chapter 4. This set of ordinary differential equations subject to the corresponding boundary conditions is solved independently by combining series and numerical solutions at the patching point, similar to the solution in chapter 5.

In addition, in this chapter, we obtain the first-order correction of the Cox-Voinov equation, providing the relationship between the position of the contact line at the current and next time instants. After determining the free surface

of the droplet along with the contact angle at the current time instant in the first step, the contact line at the next time instant is calculated using the Cox-Voinov equation in the second step. Given the position of the contact line at the next time instant, the free surface of the droplet and the contact angle can be recalculated in the first step. This iterative process implies that the entire problem in the current model is solved through forward iteration. Lastly, an example of the drop motion on an inclined plate is provided.

6.1 Problem description

In this chapter, the motion of the contact line is governed by the Cox-Voinov equation (Cox, 1986), which relates the current local contact angle, θ_c, to the normal contact line velocity,

$$\tilde{V}_n = c_T \left(\theta_c^3 - \theta_e^3\right), \tag{6.1.1}$$

where c_T is a constant depending on the solid–liquid–vapour combination and θ_e is the equilibrium contact angle. The definition of the normal velocity of the contact line for a non-flat substrate will be given below. This model does not account for hysteresis effects, meaning that the contact line always moves and only comes to a stop when and where the local current contact angle equals the equilibrium contact angle.

In the cylindrical coordinates (r, φ, z), the free surface of the droplet is described by the equation $z = \bar{\eta}(r, \varphi, t)$ and the solid substrate is given by $z = \bar{z}_p(r, \varphi, t)$. The intersection of these two surfaces is the contact line. The projection of the contact line onto xy-plane is described by the equation $r = r_c(\varphi, t)$, then the normal velocity of the contact line takes the form

$$V_n = \mathbf{X}_t(\varphi, t) \cdot \left(\mathbf{n_3} - \frac{\mathbf{X}_\varphi(\varphi, t) \cdot \mathbf{n_3}}{\mathbf{X}_\varphi(\varphi, t) \cdot \mathbf{T_3}} \mathbf{T_3}\right), \tag{6.1.2}$$

see equation (2.3.7), where the derivatives of the position vector $\mathbf{X}_t$, $\mathbf{X}_\varphi$ are given by equations (2.3.10), and the vectors $\mathbf{T_3}$, $\mathbf{n_3}$ are given by equations (2.3.8) and (2.3.9), respectively. Equation (6.1.2) gives the speed of the contact line in the normal direction with dimensional parameters. We should convert the system into dimensionless coordinates. Within these dimensionless coordinates,

$$\begin{aligned} r &= R_0 \tilde{r}, \\ r_c &= R_0 \tilde{r}_c, \\ \bar{\eta}(r, \varphi, t) &= B(t) \tilde{\eta}(\tilde{r}, \varphi, t), \\ \bar{z}_p(r, \varphi, t) &= Z_{sc} \tilde{z}_p(\tilde{r}, \varphi, t). \end{aligned} \tag{6.1.3}$$

see equations (3.1.12), where R_0 is the initial radius of the axisymmetric droplet calculated from section 2.4, $B(t)$ is the vertical scale of the droplet and Z_{sc} is the maximum displacement of deformations of the solid substrate, the free surface of the droplet is described by $\tilde{z} = \tilde{\eta}(\tilde{r}, \varphi, t)$ while the solid surface is given by $\tilde{z} = \delta\tilde{\eta}(\tilde{r}, \varphi, t)$ where $\delta = Z_{sc}/B(t)$. Substituting the dimensionless variables (6.1.3) into (6.1.2), we have $V_n = R_0\tilde{V}_n$, where the dimensionless normal velocity of the contact line reads

$$\tilde{V}_n = \tilde{\mathbf{X}}_t(\varphi, t) \cdot \left(\mathbf{n_3} - \frac{\tilde{\mathbf{X}}_\varphi(\varphi, t) \cdot \mathbf{n_3}}{\tilde{\mathbf{X}}_\varphi(\varphi, t) \cdot \mathbf{T_3}} \mathbf{T_3} \right). \tag{6.1.4}$$

Here the derivatives of the position vector are given by

$$\begin{aligned} \tilde{\mathbf{X}}_t(\varphi, t) =& \frac{\partial \tilde{r}_c}{\partial t}\hat{\mathbf{e}}_\mathbf{r} + \varepsilon_z \left(\frac{\partial \tilde{z}_p}{\partial \tilde{r}} \frac{\partial \tilde{r}_c}{\partial t} + \frac{\partial \tilde{z}_p}{\partial t} \right) \hat{\mathbf{k}} = \frac{\partial \tilde{r}_c}{\partial t}\mathbf{K} + \varepsilon_z \frac{\partial \tilde{z}_p}{\partial t}\hat{\mathbf{k}}, \\ \tilde{\mathbf{X}}_\varphi(\varphi, t) =& \frac{\partial \tilde{r}_c}{\partial \varphi}\mathbf{K} + \mathbf{A_p}, \end{aligned} \tag{6.1.5}$$

where $\mathbf{K} = \hat{\mathbf{e}}_\mathbf{r} + \varepsilon_z \dfrac{\partial \tilde{z}_p}{\partial \tilde{r}}\hat{\mathbf{k}}$, $\mathbf{A_p} = \tilde{r}_c\hat{\mathbf{e}}_\varphi + \varepsilon_z \dfrac{\partial \tilde{z}_p}{\partial \varphi}\hat{\mathbf{k}}$, and $\varepsilon_z = Z_{sc}/R_0$. The elements of vectors $\mathbf{T_3}$ and $\mathbf{n_3}$ become

$$\bar{q}_1 = \varepsilon \frac{\tilde{\eta}_\varphi}{\tilde{r}} - \varepsilon_z \frac{\tilde{z}_{p\varphi}}{\tilde{r}}, \qquad \bar{q}_2 = \varepsilon_z \tilde{z}_{pr} - \varepsilon\tilde{\eta}_{\tilde{r}}, \qquad \bar{q}_3 = \varepsilon\varepsilon_z \frac{\tilde{z}_{p\tilde{r}}\tilde{\eta}_\varphi - \tilde{\eta}_{\tilde{r}}\tilde{z}_{p\varphi}}{\tilde{r}}, \tag{6.1.6}$$

$$\begin{aligned} \bar{q}_4 =& \varepsilon_z \tilde{z}_{p\tilde{r}} - \varepsilon\tilde{\eta}_{\tilde{r}} + \varepsilon\varepsilon_z^2 \frac{\tilde{z}_{p\tilde{r}}\tilde{\eta}_\varphi \tilde{z}_{p\varphi} - \tilde{\eta}_{\tilde{r}}\tilde{z}_{p\varphi}^2}{\tilde{r}^2}, \\ \bar{q}_5 =& \varepsilon\varepsilon_z^2 \frac{\tilde{\eta}_{\tilde{r}}\tilde{z}_{p\tilde{r}}\tilde{z}_{p\varphi} - \tilde{z}_{p\tilde{r}}^2\tilde{\eta}_\varphi}{\tilde{r}} + \varepsilon_z \frac{\tilde{z}_{p\varphi}}{\tilde{r}} - \varepsilon\frac{\tilde{\eta}_\varphi}{\tilde{r}}, \\ \bar{q}_6 =& \varepsilon_z^2 \left(\tilde{z}_{p\tilde{r}}^2 + \frac{\tilde{z}_{p\varphi}^2}{\tilde{r}^2} \right) - \varepsilon\varepsilon_z \left(\tilde{\eta}_{\tilde{r}}\tilde{z}_{p\tilde{r}} + \frac{\tilde{\eta}_\varphi \tilde{z}_{p\varphi}}{\tilde{r}^2} \right), \end{aligned} \tag{6.1.7}$$

where $\varepsilon = B(t)/R_0$. Substituting (6.1.4) into (6.1.1), we obtain the following equation for the evolution of the contact line,

$$\tilde{\mathbf{X}}_t(\varphi, t) \cdot \left(\mathbf{n_3} - \frac{\tilde{\mathbf{X}}_\varphi(\varphi, t) \cdot \mathbf{n_3}}{\tilde{\mathbf{X}}_\varphi(\varphi, t) \cdot \mathbf{T_3}} \mathbf{T_3} \right) = c_T \left(\theta_c^3 - \theta_e^3 \right). \tag{6.1.8}$$

It is convenient to convert equation (6.1.8) into the stretched coordinates $(\xi, \varphi, \tilde{z})$, where the radial variable is scaled by $\xi = \tilde{r}/\tilde{r}_c(\varphi, t)$, see equation (4.1.5). The free surface of the droplet and the solid surface in the stretched coordinates are denoted by $F(\xi, \varphi, t)$ and $Z(\xi, \varphi, t)$, where

$$\begin{aligned} \tilde{\eta}(\tilde{r}, \varphi, t) &= \tilde{\eta}(\xi\tilde{r}_c(\varphi), \varphi, t) = F(\xi, \varphi, t), \\ \tilde{z}_p(\tilde{r}, \varphi, t) &= \tilde{z}_p(\xi\tilde{r}_c(\varphi), \varphi, t) = Z(\xi, \varphi, t). \end{aligned}$$

Substituting the transformations for the first derivatives, see equation (4.1.6) into equation (6.1.8), we obtain the Cox-Voinov equation presented in the stretched coordinates,

$$\frac{\partial \tilde{r}_c}{\partial t}(\mathbf{K}\cdot\mathbf{n_3} - M\mathbf{K}\cdot\mathbf{T_3}) + \varepsilon_z \frac{\partial Z}{\partial t}(\bar{b}_3 - M\bar{a}_3) = c_T\left(\theta_c^3 - \theta_e^3\right), \tag{6.1.9}$$

where

$$M = \frac{\frac{\partial \tilde{r}_c}{\partial \varphi}\mathbf{K}\cdot\mathbf{n_3} + \mathbf{A_p}\cdot\mathbf{n_3}}{\frac{\partial \tilde{r}_c}{\partial \varphi}\mathbf{K}\cdot\mathbf{T_3} + \mathbf{A_p}\cdot\mathbf{T_3}}. \tag{6.1.10}$$

The vectors in the stretched coordinates (at $\xi = 1$) are presented in the following forms,

$$\mathbf{K} = \hat{\mathbf{e}}_\mathbf{r} + \varepsilon_z \frac{Z_\xi(\xi,\varphi,t)}{\tilde{r}_c(\varphi,t)}\hat{\mathbf{k}}, \tag{6.1.11}$$

$$\mathbf{A_p} = \tilde{r}_c\hat{\mathbf{e}}_\varphi + \varepsilon_z\left(Z_\varphi - \frac{\tilde{r}_c'}{\tilde{r}_c}Z_\xi\right)\hat{\mathbf{k}}. \tag{6.1.12}$$

(6.1.6) and (6.1.7) in the stretched coordinates (at $\xi = 1$) become

$$\begin{aligned}
\bar{q}_1 =& \frac{1}{\tilde{r}_c}\left(\varepsilon(F_\varphi - \frac{\tilde{r}_c'}{\tilde{r}_c}F_\xi) - \varepsilon_z(Z_\varphi - \frac{\tilde{r}_c'}{\tilde{r}_c}Z_\xi)\right),\\
\bar{q}_2 =& \frac{\varepsilon_z Z_\xi - \varepsilon F_\xi}{\tilde{r}_c},\\
\bar{q}_3 =& \frac{\varepsilon\varepsilon_z}{\tilde{r}_c^2}\left(Z_\xi(F_\varphi - \frac{\tilde{r}_c'}{\tilde{r}_c}F_\xi) - F_\xi(Z_\varphi - \frac{\tilde{r}_c'}{\tilde{r}_c}Z_\xi)\right),
\end{aligned} \tag{6.1.13}$$

$$\begin{aligned}
\bar{q}_4 =& \frac{\varepsilon_z Z_\xi - \varepsilon F_\xi}{\tilde{r}_c} + \frac{\varepsilon\varepsilon_z^2}{\tilde{r}_c^3}\left(Z_\xi(F_\varphi - \frac{\tilde{r}_c'}{\tilde{r}_c}F_\xi)(Z_\varphi - \frac{\tilde{r}_c'}{\tilde{r}_c}Z_\xi) - F_\xi(Z_\varphi - \frac{\tilde{r}_c'}{\tilde{r}_c}Z_\xi)^2\right)\\
\bar{q}_5 =& \frac{\varepsilon\varepsilon_z^2}{\tilde{r}_c^3}\left(F_\xi Z_\xi(Z_\varphi - \frac{\tilde{r}_c'}{\tilde{r}_c}Z_\xi) - Z_\xi^2(F_\varphi - \frac{\tilde{r}_c'}{\tilde{r}_c}F_\xi)\right)\\
&+ \frac{1}{\tilde{r}_c}\left(\varepsilon_z(Z_\varphi - \frac{\tilde{r}_c'}{\tilde{r}_c}Z_\xi) - \varepsilon(F_\varphi - \frac{\tilde{r}_c'}{\tilde{r}_c}F_\xi)\right),\\
\bar{q}_6 =& \varepsilon_z^2\left((\frac{Z_\xi}{\tilde{r}_c})^2 + \frac{1}{\tilde{r}_c^2}(Z_\varphi - \frac{\tilde{r}_c'}{\tilde{r}_c}Z_\xi)^2\right) - \varepsilon\varepsilon_z\frac{F_\xi Z_\xi}{\tilde{r}_c^2}\\
&- \frac{\varepsilon\varepsilon_z}{\tilde{r}_c^2}(F_\varphi - \frac{\tilde{r}_c'}{\tilde{r}_c}F_\xi)(Z_\varphi - \frac{\tilde{r}_c'}{\tilde{r}_c}Z_\xi).
\end{aligned} \tag{6.1.14}$$

Equation (6.1.9) is a partial differential equation of the first order with only first derivatives of the contact line $\frac{\partial \tilde{r}_c}{\partial t}$, $\frac{\partial \tilde{r}_c}{\partial \varphi}$, involved, and it depends on the position function of contact line $\tilde{r}_c(\varphi,t)$, shape of the droplet $F(\xi,\varphi,t)$, and

shape of the solid substrate $Z(\xi, \varphi, t)$. In our study, we are concerned with slow deformations of the solid substrate, which allows us to analyse the dynamic behaviour of the droplet by the quasi-static approximation without time derivatives in the boundary conditions on the free surface of the droplet. However, we keep the time derivative $\dfrac{\partial \tilde{r}_c}{\partial t}$ in the Cox-Voinov equation. To find the motion of the contact line within the present model, we consider the next time instant

$$\hat{t} = t + \Delta t, \tag{6.1.15}$$

where Δt is the step of integration of the Cox-Voinov equation in time. For small $\Delta t \to 0$, the partial derivatives $\dfrac{\partial \tilde{r}_c}{\partial t}$ and $\dfrac{\partial Z}{\partial t}$ can be approximated as

$$\begin{aligned} \frac{\partial \tilde{r}_c(\varphi, t)}{\partial t} &= \frac{\tilde{r}_c(\varphi, \hat{t}) - \tilde{r}_c(\varphi, t)}{\Delta t} \approx \frac{\hat{r}_c(\varphi) - \tilde{r}_c(\varphi)}{\Delta t}, \\ \frac{\partial Z(\xi, \varphi, t)}{\partial t} &= \frac{Z(\xi, \varphi, \hat{t}) - Z(\xi, \varphi, t)}{\Delta t} \approx \frac{\hat{Z}(\xi, \varphi) - Z(\xi, \varphi)}{\Delta t}. \end{aligned} \tag{6.1.16}$$

Here, $\tilde{r}_c(\varphi)$ and $Z(\xi, \varphi)$ are the functions describing the positions of the contact line and the solid surface at the current time instant while $\hat{r}_c(\varphi)$ and $\hat{Z}(\xi, \varphi)$ represent the contact line and solid surface at the next time instant, respectively. Thus, the Cox-Voinov equation in the quasi-static approximation read

$$\begin{aligned} &\left(\hat{r}_c(\varphi) - \tilde{r}_c(\varphi)\right)\left(\mathbf{K} \cdot \mathbf{n_3} - M\mathbf{K} \cdot \mathbf{T_3}\right) + \varepsilon_z(\bar{b}_3 - M\bar{a}_3)\left(\hat{Z}(\xi, \varphi) - Z(\xi, \varphi)\right) \\ &\qquad = c_T \Delta t \left(\theta_c^3(\xi, \varphi) - \theta_e^3\right), \end{aligned} \tag{6.1.17}$$

where the vectors in (6.1.17) are given by equations (6.1.10)–(6.1.14).

As we employ the quasi-static approximation, the parameter t is not shown in the following equations. The results of chapter 4 provide that the free surface of the droplet is governed by the Young-Laplace equation at each time instant,

$$\frac{a_2 + \varepsilon^2 a_3}{(1 + \varepsilon^2 a_1)^{3/2}} = Bo[F(\xi, \varphi) - 1] \qquad (\xi < 1, \quad -\pi < \varphi < \pi), \tag{6.1.18}$$

see equation (4.1.7), where Bo is the Bond number, a_1, a_2 and a_3 are given by (4.1.8). The governing equation (6.1.18) subject to a boundary condition,

$$F(1, \varphi) = \delta Z(1, \varphi), \tag{6.1.19}$$

see equation (4.1.9), and a condition of the constant droplet volume,

$$-\frac{1}{Bo}\int_{-\pi}^{\pi}\left(\frac{\varepsilon a_7 \tilde{r}_c(\varphi)}{\sqrt{1 + \varepsilon^2 a_8}}\right) d\varphi = \varepsilon\left(|S| - \delta\int_{-\pi}^{\pi}\int_0^1 Z(\xi, \varphi)\tilde{r}_c^2(\varphi)\xi d\xi d\varphi\right) - \frac{V_0}{R_0^3}, \tag{6.1.20}$$

where $|S| = \frac{1}{2}\int_{-\pi}^{\pi} \tilde{r}_c^2(\varphi)d\varphi$, see equation (4.1.12). Here a_7 and a_8 are given by equation (4.1.13). The contact angle is calculated by the following equation,

$$\cos\theta_c(\xi,\varphi) = \frac{1+\varepsilon\varepsilon_z a_5}{\sqrt{1+\varepsilon^2 a_4}\sqrt{1+\varepsilon_z^2 a_6}} \qquad (\xi = 1, \quad -\pi < \varphi < \pi), \tag{6.1.21}$$

see equation (4.1.10), where the functions a_4, a_5, a_6 are given by equation (4.1.11). The problem of (6.1.18)–(6.1.20) with the model of the contact line (6.1.17) should be solved using the initial contact line,

$$\tilde{r}_c(\varphi) = 1 \qquad (t = 0), \tag{6.1.22}$$

and droplet shape obtained in section 2.4.

This section presented the conversion of the Cox-Voinov equation to the stretched coordinates (6.1.17). Within the stretched coordinates, the contact line was incorporated into the governing equation (6.1.18) and conditions (6.1.19)–(6.1.21).

6.2 Asymptotic solution

We employ a similar way following the previous chapters to find the asymptotic solution of the problem (6.1.17)–(6.1.22) by considering a small deformation of the solid substrate $\delta \ll 1$ and $\varepsilon = O(1)$. The droplet shape, contact angle, aspect ratio and position of the contact line are sought in the form,

$$\begin{aligned} F(\xi,\varphi) &= F_0(\xi) + \delta F_1(\xi,\varphi) + O(\delta^2),\\ \theta_c(\varphi) &= \theta_e + \delta V(\varphi) + O(\delta^2),\\ \varepsilon &= \varepsilon_0 + \delta\varepsilon_1 + O(\delta^2),\\ \tilde{r}_c(\varphi) &= 1 + \delta g(\varphi) + O(\delta^2),\\ \hat{r}_c(\varphi) &= 1 + \delta\hat{g}(\varphi) + O(\delta^2). \end{aligned} \tag{6.2.1}$$

Note that $g(\varphi)$ is known in this model of the contact line, but we need to add this function to present the contribution from a non-circular contact line. The function $\hat{g}(\varphi)$, representing the position of the contact line at the next time instant, is to be determined.

The results of chapter 4 give the governing equation for the first-order correction of the droplet shape,

$$\begin{aligned} H_1(\xi)F_{1,\xi\xi} + H_2(\xi)\frac{F_{1,\xi}}{\xi} + H_3(\xi)\frac{F_{1,\varphi\varphi}}{\xi^2} + H_4(\xi)\varepsilon_1 \\ + H_5(\xi)g(\varphi) + H_6(\xi)g''(\varphi) = BoF_1, \end{aligned} \tag{6.2.2}$$

see equation (4.2.4), where the functions $H_i(\xi)$, $i = 1, 2, \cdots, 6$, are given by

equations (3.2.6) and (4.2.5), and the boundary condition

$$F_1(1,\varphi) = \tilde{z}_p(1,\varphi), \tag{6.2.3}$$

see equation (4.2.6). The condition (6.1.20) provides

$$\begin{aligned}\frac{1}{Bo}\int_{-\pi}^{\pi}\left(\sin\theta_e\cos^2\theta_e\frac{\varepsilon_1}{\varepsilon_0} - \cos^3\theta_e\varepsilon_0 F_{1,\xi}(1,\varphi) + \sin^3\theta_e g(\varphi)\right)d\varphi \\ = \varepsilon_1\pi + \varepsilon_0\left(\int_{-\pi}^{\pi} g(\varphi)d\varphi - \int_{-\pi}^{\pi}\int_0^1 \tilde{z}_p(\xi,\varphi)\xi d\xi d\varphi\right),\end{aligned} \tag{6.2.4}$$

see equation (4.2.8). The first-order correction of the contact angle is calculated using the following equation

$$V(\varphi) = \varepsilon_0\tilde{z}_{p,\xi}(1,\varphi) + \sin\theta_e\cos\theta_e\left(\frac{\varepsilon_1}{\varepsilon_0} - g(\varphi)\right) - \varepsilon_0\cos^2\theta_e F_{1,\xi}(1,\varphi), \tag{6.2.5}$$

see equation (**??**).

Substituting the expansions (6.2.1) into (6.1.13) and (6.1.14), we have

$$\begin{aligned}\bar{q}_1 =& \delta\left(\varepsilon_0 F_{1,\varphi}(1,\varphi) - \varepsilon_0 F_{0,\xi}(1)g'(\varphi) - \varepsilon_0\tilde{z}_{p,\varphi}(1,\varphi)\right) + O(\delta^2),\\ \bar{q}_2 =& -\varepsilon_0 F_{0,\xi}(1) + \delta\left(\varepsilon_0\tilde{z}_{p,\xi}(1,\varphi) + \varepsilon_0 F_{0,\xi}(1)g(\varphi) - \varepsilon_0 F_{1,\xi}(1,\varphi) - \varepsilon_1 F_{0,\xi}(1)\right) + O(\delta^2),\\ \bar{q}_3 =& -\delta\varepsilon_0^2 F_{0,\xi}(1)\tilde{z}_{p,\varphi}(1,\varphi) + O(\delta^2),\end{aligned} \tag{6.2.6}$$

$$\begin{aligned}\bar{q}_4 =& -\varepsilon_0 F_{0,\xi}(1) + \delta\left(\varepsilon_0\tilde{z}_{p,\xi}(1) + \varepsilon_0 F_{0,\xi}(1)g(\varphi) - \varepsilon_0 F_{1,\xi}(1,\varphi) - \varepsilon_1 F_{0,\xi}(1)\right) + O(\delta^2),\\ \bar{q}_5 =& -\delta\left(\varepsilon_0 F_{1,\varphi}(1,\varphi) - \varepsilon_0 F_{0,\xi}(1)g'(\varphi) - \varepsilon_0\tilde{z}_{p,\varphi}(1,\varphi)\right) + O(\delta^2),\\ \bar{q}_6 =& -\delta\varepsilon_0^2 F_{0,\xi}(1)\tilde{z}_{p,\xi}(1,\varphi) + O(\delta^2).\end{aligned} \tag{6.2.7}$$

Hence, the term $\varepsilon_z(\bar{b}_3 - M\bar{a}_3)[\hat{Z}(\xi,\varphi) - Z(\xi,\varphi)]$ in equation (6.1.17) has no contribution up to $O(\delta^2)$. The magnitude $\sqrt{\bar{q}_1^2+\bar{q}_2^2+\bar{q}_3^2}$ only depends on the component $\bar{q}_2$ while $\sqrt{\bar{q}_4^2+\bar{q}_5^2+\bar{q}_6^2}$ depends on $\bar{q}_4$ since the rest terms start with $O(\delta^2)$, which gives

$$\begin{aligned}&\frac{1}{\sqrt{\bar{q}_1^2+\bar{q}_2^2+\bar{q}_3^2}} = \frac{1}{\sqrt{\bar{q}_4^2+\bar{q}_5^2+\bar{q}_6^2}}\\ &= -\frac{1}{\varepsilon_0 F_{0,\xi}(1)} - \delta\frac{\varepsilon_0\tilde{z}_{p,\xi}(1,\varphi) + \varepsilon_0 F_{0,\xi}(1)g(\varphi) - \varepsilon_0 F_{1,\xi}(1,\varphi) - \varepsilon_1 F_{0,\xi}(1)}{\varepsilon_0^2 F_{0,\xi}^2(1)} + O(\delta^2).\end{aligned}$$

Once we get the magnitude of the vectors $\mathbf{T_3}$ and $\mathbf{n_3}$, the scalar products $\mathbf{K}\cdot\mathbf{n_3}$,

$\mathbf{A_p}\cdot\mathbf{n_3}$, $\mathbf{K}\cdot\mathbf{T_3}$, $\mathbf{A_p}\cdot\mathbf{T_3}$ can then be calculated

$$\begin{aligned}
\mathbf{K}\cdot\mathbf{n_3} =& \frac{\bar{q}_4}{\sqrt{\bar{q}_4^2+\bar{q}_5^2+\bar{q}_6^2}} = 1+O(\delta^2),\\
\mathbf{A_p}\cdot\mathbf{n_3} =& \frac{\tilde{r}_c(\varphi)\bar{q}_5}{\sqrt{\bar{q}_4^2+\bar{q}_5^2+\bar{q}_6^2}} = -\delta\left(\frac{\tilde{z}_{p,\varphi}(1,\varphi)-F_{1,\varphi}(1,\varphi)}{F_{0,\xi}(1)}+g^{'}(\varphi)\right)+O(\delta^2),\\
\mathbf{K}\cdot\mathbf{T_3} =& \frac{\bar{q}_1}{\sqrt{\bar{q}_1^2+\bar{q}_2^2+\bar{q}_3^2}} = \delta\left(\frac{\tilde{z}_{p,\varphi}(1,\varphi)-F_{1,\varphi}(1,\varphi)}{F_{0,\xi}(1)}+g^{'}(\varphi)\right)+O(\delta^2),\\
\mathbf{A_p}\cdot\mathbf{T_3} =& \frac{\tilde{r}_c(\varphi)\bar{q}_2}{\sqrt{\bar{q}_1^2+\bar{q}_2^2+\bar{q}_3^2}} = 1+\delta g(\varphi)+O(\delta^2).
\end{aligned} \tag{6.2.8}$$

As a result, the expansions of (6.1.10) gives

$$M = -\delta\frac{\tilde{z}_{p,\varphi}(1,\varphi)-F_{1,\varphi}(1,\varphi)}{F_{0,\xi}(1)}+O(\delta^2), \tag{6.2.9}$$

so the term $M\mathbf{K}\cdot\mathbf{T_3}$ in (6.1.17) is negligible. Therefore, the first-order correction of the Cox-Voinov equation reads

$$\hat{g}(\varphi)-g(\varphi) = 3c_T\theta_e^2\Delta t V(\varphi). \tag{6.2.10}$$

The governing equation (6.2.2) is a second-order partial differential equation with singular variables coefficients, which is solved by the same methodology as the previous chapter by employing Fourier series to separate variables ξ and φ. See equations (5.2.7)–(5.2.9) for $F_1(\xi,\varphi)$, $g(\varphi)$, $V(\varphi)$. The contact line at next time step, $\hat{g}(\varphi)$, is searched in the form of Fourier series,

$$\hat{g}(\varphi) = \hat{A}_0+\sum_{n=1}^{\infty}[\hat{A}_n\cos n\varphi+\hat{A}_n^*\sin n\varphi], \tag{6.2.11}$$

where $\hat{A}_0$, $\hat{A}_n$, $\hat{A}_n^*$, $n=1,2,3,\cdots$, are to be determined. Applying the Fourier decomposition to equation (6.2.2), the resulting set of ordinary differential equations takes the form

$$H_1(\xi)\alpha_0^{''}+H_2(\xi)\frac{\alpha_0^{'}}{\xi}-Bo\alpha_0 = -H_4(\xi)\varepsilon_1-H_5(\xi)A_0, \tag{6.2.12}$$

$$H_1(\xi)\alpha_n^{''}+H_2(\xi)\frac{\alpha_n^{'}}{\xi}-\left[Bo\xi^2+n^2H_3(\xi)\right]\frac{\alpha_n}{\xi^2} = \left[n^2H_6(\xi)-H_5(\xi)\right]A_n, \tag{6.2.13}$$

$$H_1(\xi)\alpha_n^{*''}+H_2(\xi)\frac{\alpha_n^{*'}}{\xi}-\left[Bo\xi^2+n^2H_3(\xi)\right]\frac{\alpha_n^{*}}{\xi^2} = \left[n^2H_6(\xi)-H_5(\xi)\right]A_n^*, \tag{6.2.14}$$

see equations (4.2.11)–(4.2.13). The Fourier series and the boundary condition

(6.2.3) provide the corresponding boundary conditions for equations (6.2.12)–(6.2.14),

$$\begin{aligned}\alpha_0(1) =&\frac{1}{2\pi}\int_{-\pi}^{\pi}\tilde{z}_p(1,\varphi)d\varphi,\\ \alpha_n(1) =&\frac{1}{\pi}\int_{-\pi}^{\pi}\tilde{z}_p(1,\varphi)\cos(n\varphi)d\varphi,\\ \alpha_n^*(1) =&\frac{1}{\pi}\int_{-\pi}^{\pi}\tilde{z}_p(1,\varphi)\sin(n\varphi)d\varphi.\end{aligned} \tag{6.2.15}$$

Also, we have a condition for ε_1,

$$\varepsilon_1 = k_1\alpha_0'(1) + k_2A_0 + k_3, \tag{6.2.16}$$

see equation (4.2.16), where constants k_1, k_2, k_3 are given by equations (4.2.17). Two boundary conditions are required for each of the equations (6.2.12)–(6.2.14), but we get only one available condition for each equation. However, we seek the finite curvature of the free surface of the droplet at the droplet centre, so there could exist a restriction on the class of solutions, which serves as the required second condition for each of them, as in chapter 3. Using the Fourier series of $F_1(\xi,\varphi)$, $g(\varphi)$ and $V(\varphi)$, the first-order correction of the contact angle (6.2.5) are given by

$$\begin{aligned}B_0 =&\varepsilon_0\int_{-\pi}^{\pi}\tilde{z}_{p,\xi}(1,\varphi)d\varphi + \sin\theta_e\cos\theta_e\left(\frac{\varepsilon_1}{\varepsilon_0} - A_0\right) - \varepsilon_0\cos^2\theta_e\alpha_0'(1),\\ B_n =&\varepsilon_0\int_{-\pi}^{\pi}\tilde{z}_{p,\xi}(1,\varphi)\cos(n\varphi)d\varphi - \sin\theta_e\cos\theta_eA_n - \varepsilon_0\cos^2\theta_e\alpha_n'(1),\\ B_n^* =&\varepsilon_0\int_{-\pi}^{\pi}\tilde{z}_{p,\xi}(1,\varphi)\sin(n\varphi)d\varphi - \sin\theta_e\cos\theta_eA_n^* - \varepsilon_0\cos^2\theta_e\alpha_n'^*(1).\end{aligned} \tag{6.2.17}$$

Substituting (5.2.8) and (6.2.11) into (6.2.10), we obtain the relation of the position of the contact line at the current and next time instant,

$$\begin{aligned}\hat{A}_0 =&A_0 + 3c_T\theta_e^2\Delta tB_0,\\ \hat{A}_n =&A_n + 3c_T\theta_e^2\Delta tB_n,\\ \hat{A}_n^* =&A_n^* + 3c_T\theta_e^2\Delta tB_n^*,\end{aligned} \tag{6.2.18}$$

The initial condition (6.1.22) provides ($t = 0$)

$$A_0 = 0, \qquad A_n = 0, \qquad A_n^* = 0. \tag{6.2.19}$$

6.3 General solution

In this model, the governing equations (6.2.12)–(6.2.14) subject to the corresponding boundary conditions (6.2.15) and condition (6.2.16) are first solved with the given position of the contact line at the current time instant. Once the droplet shape $F_1(\xi, \varphi)$ at the current instant is determined, the contact angle $V(\varphi)$ at the current instant is calculated using (6.2.17). After that, the position of the contact line at the next time instant is determined using (6.2.18). Following this, we obtain the droplet shape at the next time instant by solving the problem of (6.2.12)–(6.2.16) with the new position of the contact line from (6.2.18). This iterative process continues until the terminal time is reached.

A similar approach to the one in chapter 5 is used to obtain the combined solutions at the patching point $a \in (0, 1)$. In this approach, regular series solutions are applied for $\xi \in [0, a]$ while numerical solutions are applied for the interval $\xi \in [a, 1]$. For the current time instant, the combined solutions of the governing equations (6.2.12) reads

$$\alpha_0(\xi) = \begin{cases} C_0\alpha_0^{(hr)}(\xi) + \varepsilon_1\alpha_0^{(p1)}(\xi) + A_0\alpha_0^{(p2)}(\xi) & (0 < \xi < a), \\ \alpha_0(1)\alpha_0^{(1)}(\xi) + \alpha_0^{'}(1)\alpha_0^{(2)}(\xi) + \varepsilon_1\alpha_0^{(3)}(\xi) + A_0\alpha_0^{(4)}(\xi) & (a < \xi < 1), \end{cases} \tag{6.3.1}$$

see equation (5.3.6), where $\alpha_0(1)$ is given by equation (6.2.15), C_0 and $\alpha_0^{'}(1)$ are determined by solving the system of equations (5.3.7) with given A_0, and ε_1 is calculated using (6.2.16) once A_0 are $\alpha_0^{'}(1)$ are known. The solution (6.3.1) is fully determined since A_0 is given in the present model.

Likewise, the combined solution of (6.2.13) takes the form

$$\alpha_n(\xi) = \begin{cases} C_n\alpha_n^{(hr)}(\xi) + A_n\alpha_n^{(p)}(\xi) & (0 < \xi < a), \\ \alpha_n(1)\alpha_n^{(1)}(\xi) + \alpha_n^{'}(1)\alpha_n^{(2)}(\xi) + A_n\alpha_n^{(3)}(\xi) & (a < \xi < 1), \end{cases} \tag{6.3.2}$$

see equation (5.3.12), where $\alpha_n(1)$, $n = 1, 2, 3, \cdots$, are given by equations (6.2.15), C_n and $\alpha_n^{'}(1)$ are determined by solving the system of equations (5.3.13) with given A_n. In this model, the solution (6.3.2) is completely determined as A_n is given. Note that equation (6.2.13) is identical to (6.2.14), so the combined solution of (6.2.14) can be obtained by changing the notation in (6.3.2).

In this model, we have the initial contact line (6.2.19) and the relation of the contact line between the current and next time instant (6.2.18). Hence, the evolution of the position of the contact line can be completely described through the forward iteration.

6.4 Example

We consider an inclining plate, which is initially horizontal and gradually starts to incline. This inclination is represented by the equation

$$\tilde{z}_p(\xi, \varphi) = A(t)\xi \cos\varphi, \tag{6.4.1}$$

where $A(t) = 0$ at the initial time instant and $A(t) > 0$ as $t > 0$. Note that $A(t)$ cannot be scaled out in the current case since we now have the time derivative in the Cox-Voinov equation.

In this particular case, only the $n = 1$ terms in equations (6.3.2) are required due to the orthogonality, resulting in a simplified expression

$$\alpha_1(\xi) = \begin{cases} C_1\alpha_1^{(hr)}(\xi) + A_1\alpha_1^{(p)}(\xi) & (0 < \xi < a), \\ \alpha_1(1)\alpha_1^{(1)}(\xi) + \alpha_1^{'}(1)\alpha_1^{(2)}(\xi) + A_1\alpha_1^{(3)}(\xi) & (a < \xi < 1). \end{cases} \tag{6.4.2}$$

Here, C_1 and $\alpha_1^{'}(1)$ are determined by solving the following system with respect to C_1 and $\alpha_1^{'}(1)$,

$$\begin{aligned} \alpha_1^{(hr)}(a)C_1 - \alpha_1^{(2)}(a)\alpha_1^{'}(1) &= M_{11}A_1 + \alpha_1^{(1)}(a)\alpha_1(1), \\ \alpha_{1,\xi}^{(hr)}(a)C_1 - \alpha_{1,\xi}^{(2)}(a)\alpha_1^{'}(1) &= M_{12}A_1 + \alpha_{1,\xi}^{(1)}(a)\alpha_1(1), \end{aligned} \tag{6.4.3}$$

see equations (5.3.13), where $M_{11} = \alpha_1^{(3)}(a) - \alpha_1^{(p)}(a)$ and $M_{12} = \alpha_{1,\xi}^{(3)}(a) - \alpha_{1,\xi}^{(p)}(a)$. Since $\alpha_1^{'}(1)$ can be written in the form

$$\alpha_1^{'}(1) = D_{12}A_1 + E_{12}\alpha_1(1), \tag{6.4.4}$$

see equation (5.3.17), where D_{12} and E_{12} are given by (5.3.20). The first-order correction of the contact angle (6.2.17) is simplified to

$$B_1 = \varepsilon_0 \int_{-\pi}^{\pi} \tilde{z}_{p,\xi}(1, \varphi)\cos\varphi d\varphi - \sin\theta_e \cos\theta_e A_1 - \varepsilon_0 \cos^2\theta_e \left[D_{12}A_1 + E_{12}\alpha_1(1)\right], \tag{6.4.5}$$

and the Cox-Voinov equation (6.2.18) is reduced to

$$\hat{A}_1 = A_1 + C\Delta t B_1, \tag{6.4.6}$$

where $C = 3c_T\theta_e^2$. From the literature, c_T, depending on the properties of the fluid and the solid substrate, typically ranges from 2×10^{-3} to 6×10^{-3}. Given an equilibrium contact angle of 70° and $c_T = 4.5 \times 10^{-3}$, we have $C \approx 0.02$. Since we are considering the slow deformation of the substrate, we set $A(t) = 0.01t$. By choosing $\delta = 0.1$, the evolution of the contact line is depicted in Figure 6.4.1. Initially, the contact line has a circular shape. As time progresses, the contact

line deforms and moves to the left.

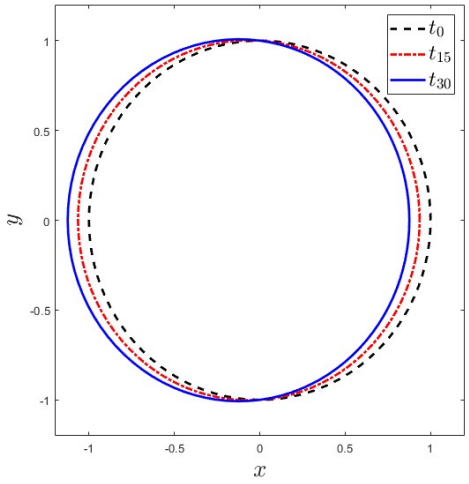

Figure 6.4.1: The position of the contact line at the time instant of t_0, t_{15}, t_{30}, for $C = 0.02$.

Essentially, there is a geometric limitation to our contact line evolution. In this example, the position of the contact line at a given time can be described by the equation

$$\tilde{r}_c(\varphi) = 1 + Q\cos\varphi, \tag{6.4.7}$$

where Q is a negative number as the contact line moves to the left. Figure 6.4.2 illustrates the position of the contact line corresponding to different values of Q. For large values of Q, the contact line deviates from physical interpretation since it has an intersection. To ensure meaningful simulation results, the terminal time will be set when $Q = -0.5$.

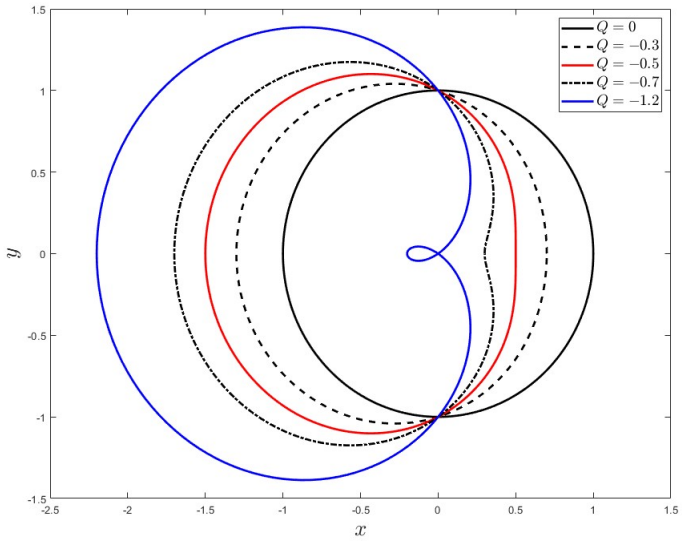

Figure 6.4.2: The position of the contact line changes with different values of Q.

To examine the influence of C, we introduce another scenario where all parameters remain the same except for C, which varies from 0.02 to 0.1. Figure 6.4.3 displays two cases of the droplet's cross-section, with $V_0 = 0.1\,\text{mL}$. A higher value of C represents better mobility.

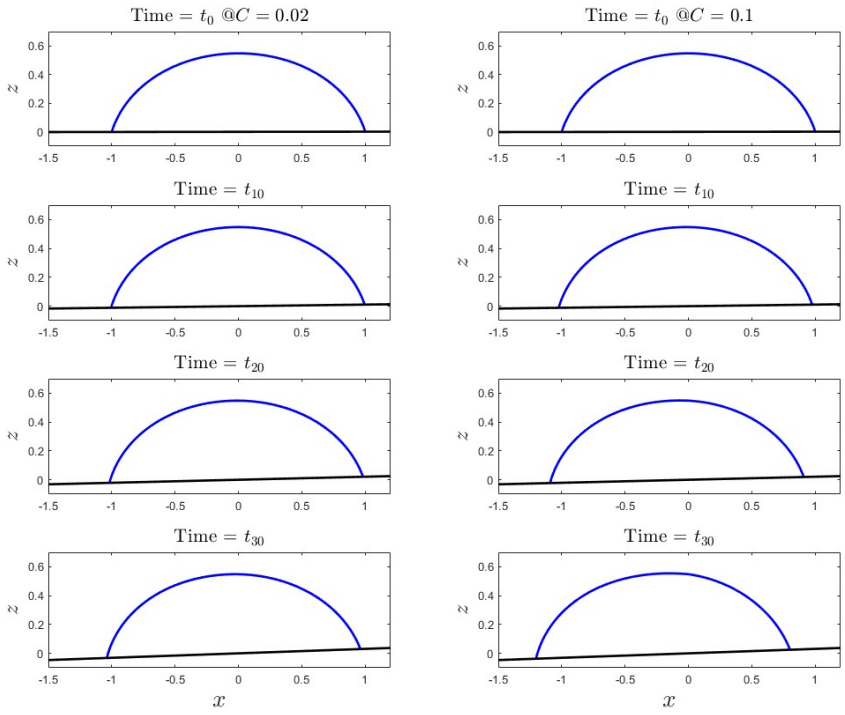

Figure 6.4.3: Cross-section of the droplet shape with different C at the time instant of t_0, t_{10}, t_{20} and t_{30}.

Figure 6.4.4 illustrates the three-dimensional motion of a droplet on an inclined plate. The initial shape of the droplet is axisymmetric, and the black line represents the initial position of the contact line. The elevation of the substrate varies slowly over time, causing the droplet to move downward.

Up to this point, we have considered small values of $A(t)$ to align with our assumption. However, when adjusting to larger values of A(t), the evolution of the contact line changes direction (the droplet climbs uphill), which reminds us of the results observed by Brunet et al. (2007). In their finding, the droplet climbs upward when the acceleration of the solid substrate exceeds a certain threshold. Nevertheless, with large values of $A(t)$, the droplet shape breaks due to the large deformation of the substrate.

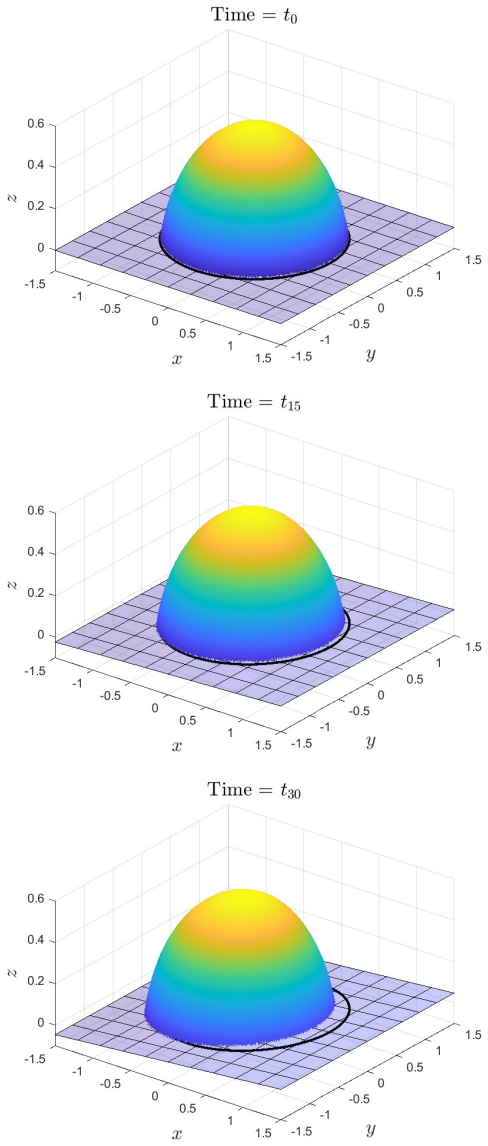

Figure 6.4.4: A three-dimensional droplet slides down along the inclined plate at the instant times t_0 t_0, and t_{30}.

7

Conclusion

7.1 Summary

The analysis of droplet shapes on solid surfaces has been extensively studied for over 20 years. It is well-known, especially for flat solid surfaces, since it could be reasonable to assume the axisymmetric shape. However, discussing non-flat surfaces still presents challenges. We are interested in studying droplet motion induced by deformations of a solid substrate. Since we concentrate on slow substrate deformations, we can analyse the droplet dynamics using the quasi-static approximation. In this approximation, in the leading order, the flow inside the droplet is neglected, and the droplet shape at each instant is balanced by gravity and capillary forces.

This thesis explores various contact line models to understand droplet dynamics. In each scenario, the axisymmetric droplet initially rests on a flat and horizontal solid substrate before the substrate experiences a time-dependent deformation. This initial axisymmetric free surface of the droplet is calculated in section 2.4 numerically for appropriate droplet volumes and asymptotically for large volumes. Then, we apply asymptotic methods to solve the quasi-static problem, considering small deformations of the substrate in the vertical dimension compared to the thickness of the droplet. The free surface of the droplet is obtained by summing the leading order term and the first-order correction, where the leading order term originates from the initial axisymmetric droplet shape, and the first-order correction depends on the chosen contact line model.

In chapter 3, the contact line remains circular at all time instants. The model of the pinned contact line is represented as a Dirichlet boundary value problem. The governing equation for the first-order correction of the droplet shape is simplified to an infinite set of ordinary differential equations with variable coefficients by employing Fourier decomposition. To find a solution for each of the ordinary differential equations, we combine the series solution, which is solved using the Frobenius method close to the centre of the droplet, and the numerical solution at the patching point $\tilde{r} = a$. The unknown constants in both series and numerical solutions are determined through the patching conditions that

ensure the combined solution is continuous and smooth. We provide the most straightforward example where only one value of $n = 1$ is required to solve, which refers to a droplet placed on an inclined plate. This scenario is commonly studied to investigate non-axisymmetric shapes. In addition, we extend our analysis to cases that require multiple values of n to illustrate the broader applicability of our method.

We address a free boundary value problem in chapter 4, where the position of the contact line $\tilde{r} = \tilde{r}_c(\varphi)$ is unknown in advance and should be determined. In this scenario, the contact line is non-circular, so we introduce the new coordinates called the stretched coordinates $(\xi, \varphi, \tilde{z})$ where $\xi = \tilde{r}/\tilde{r}_c(\varphi)$ to handle the issue. After substituting the asymptotic expansions and utilising the Fourier decomposition to separate variables, the resulting governing equation in the first-order correction is similar to the one in the model of the pinned contact line but becomes more complicated due to the influence of the contact line. Following a methodology similar to the one applied in the previous chapter, we derive a combined solution for the free surface of the droplet and the position of the contact line in the first correction.

In chapter 5, the model of the contact line integrates the characteristics of the previous two models. The contact line is split into the pinned, where $\theta_r < \theta_c < \theta_a$, and unpinned regions, where $\theta_c = \theta_a$ or $\theta_c = \theta_r$. The position of the contact line in the unpinned region and the intervals of the unpinned region are to be determined, so this is a free mixed boundary value problem. Following the similar methodology as in chapter 4, we have the same governing equation for the first-order correction of the droplet shape and then obtain a similar form of a combined solution for the free surface of the droplet. However, in the present model, the coefficients in the combined solution are not completely determined. To resolve this, we solve the coupled equations to obtain the position of the contact line. Once the contact line is known, the combined solution for the first-order correction of droplet shape is fully determined. Here, we present the motion of a droplet on an inclined surface, taking into account the hysteresis effect. Our results closely align with experimental observations. The phenomenon of advancing or receding can occur separately or simultaneously.

In chapter 6, we utilise The Cox-Voinov equation as the contact line model. In this scenario, the contact line is not circular and moves at each time instant. The problem is approached in two segments for each time instant. The first phase involves determining the droplet shape together with the contact angle at the time instant for the known contact line, similar to as in chapter 3. We use a similar way to analyse the problem in this step. Essentially, the governing equation for the free surface of the droplet and the combined solution of the droplet shape have been presented in the previous chapters. The second phase involves using the Cox-Voinov equation to establish the relationship between the position of the

contact line in the first-order correction at the current and next time instants. Hence, the problem in the present model is resolved through forward iteration.

7.2 Conclusion and future work

We develop our method for analysing droplet hydrodynamics by employing the quasi-static approximation. The quasi-static problem is solved asymptotically. While many studies in the literature have numerically solved this problem or focused on specific substrate shapes theoretically, our methodology can be applied to any shape of solid substrate with a theoretical solution.

Droplet dynamics are complicated, and our focus lies on determining the shape (domain) of the droplet in the leading order. Since the droplet shape is now known, we could consider calculating the flow inside the droplet through computational fluid dynamics (CFD) simulation to extend our work. Additionally, accounting for viscous effects would bring our model closer to reality.

When addressing the hysteresis effect, many researchers have utilised specialized software such as Surface Evolver. Our contact line models successfully present the hysteresis effect, with results closely aligning with qualitative experimental observations. However, for a more rigorous analysis, it would be beneficial to compare our results with other data for quantitative validation.

In our final model, we incorporated the Cox-Voinov equation to describe the evolution of the contact line, including the time derivative. In future work, verifying the value of C will be crucial for extending our approach to more realistic scenarios.

Bibliography

Abramowitz, M., Stegun, I. A., and Romer, R. H. (1988). Handbook of mathematical functions with formulas, graphs, and mathematical tables.

Allen, J. S. (2003). An analytical solution for determination of small contact angles from sessile drops of arbitrary size. *Journal of Colloid and Interface Science*, 261(2):481–489.

Bashforth, F. and Adams, J. (1883). *An attempt to test the theories of capillarity.* Cambridge University Press.

Berejnov, V. and Thorne, R. E. (2007). Effect of transient pinning on stability of drops sitting on an inclined plane. *Physical Review E*, 75(6):066308.

Blake, T. D. (2006). The physics of moving wetting lines. *Journal of Colloid and Interface Science*, 299(1):1–13.

Bonn, D., Eggers, J., Indekeu, J., Meunier, J., and Rolley, E. (2009). Wetting and spreading. *Reviews of Modern Physics*, 81(2):739.

Bormashenko, E. (2009). Wetting of flat and rough curved surfaces. *The Journal of Physical Chemistry C*, 113(40):17275–17277.

Brandon, S., Wachs, A., and Marmur, A. (1997). Simulated contact angle hysteresis of a three-dimensional drop on a chemically heterogeneous surface: A numerical example. *Journal of Colloid and Interface Science*, 191(1):110–116.

Brunet, P., Eggers, J., and Deegan, R. (2007). Vibration-induced climbing of drops. *Physical Review Letters*, 99(14):144501.

Brutin, D. and Starov, V. (2018). Recent advances in droplet wetting and evaporation. *Chemical Society Reviews*, 47(2):558–585.

Buguin, A., Talini, L., and Silberzan, P. (2002). Ratchet-like topological structures for the control of microdrops. *Applied Physics A*, 75:207–212.

Butt, H.-J., Liu, J., Koynov, K., Straub, B., Hinduja, C., Roismann, I., Berger, R., Li, X., Vollmer, D., Steffen, W., et al. (2022). Contact angle hysteresis. *Current Opinion in Colloid and Interface Science*, page 101574.

Cassie, A. and Baxter, S. (1944). Wettability of porous surfaces. *Transactions of the Faraday Society*, 40:546–551.

Chen, Y., He, B., Lee, J., and Patankar, N. A. (2005). Anisotropy in the wetting of rough surfaces. *Journal of Colloid and Interface Science*, 281(2):458–464.

Chou, T.-H., Hong, S.-J., Sheng, Y.-J., and Tsao, H.-K. (2012). Drops sitting on a tilted plate: Receding and advancing pinning. *Langmuir*, 28(11):5158–5166.

Cox, R. (1986). The dynamics of the spreading of liquids on a solid surface: Viscous flow. *Journal of Fluid Mechanics*, 168:169–194.

Daniel, S., Chaudhury, M. K., and De Gennes, P.-G. (2005). Vibration-actuated drop motion on surfaces for batch microfluidic processes. *Langmuir*, 21(9):4240–4248.

Daniel, S., Sircar, S., Gliem, J., and Chaudhury, M. K. (2004). Ratcheting motion of liquid drops on gradient surfaces. *Langmuir*, 20(10):4085–4092.

De Coninck, J., Dunlop, F., and Huillet, T. (2017). Contact angles of a drop pinned on an incline. *Physical Review E*, 95(5):052805.

de la Madrid, R., Garza, F., Kirk, J., Luong, H., Snowden, L., Taylor, J., and Vizena, B. (2019). Comparison of the lateral retention forces on sessile, pendant, and inverted sessile drops. *Langmuir*, 35(7):2871–2877.

Duncombe, T. A., Erdem, E. Y., Shastry, A., Baskaran, R., and Böhringer, K. F. (2012). Controlling liquid drops with texture ratchets. *Advanced Materials*, 24(12):1545–1550.

ElSherbini, A. and Jacobi, A. (2004). Liquid drops on vertical and inclined surfaces: A method for approximating drop shapes. *Journal of Colloid and Interface Science*, 273(2):566–575.

Extrand, C. (2006). Relation between contact angle and the cross-sectional area of small, sessile liquid drops. *Langmuir*, 22(20):8431–8434.

Extrand, C. W. and Kumagai, Y. (1995). Liquid drops on an inclined plane: The relation between contact angles, drop shape, and retentive force. *Journal of Colloid and Interface Science*, 170(2):515–521.

Fordham, S. (1948). On the calculation of surface tension from measurements of pendant drops. *Proceedings of the Royal Society of London. Series A. Mathematical and Physical Sciences*, 194(1036):1–16.

Gennes, P.-G., Brochard-Wyart, F., Quéré, D., et al. (2004). *Capillarity and wetting phenomena: drops, bubbles, pearls, waves*. Springer.

Hamrock, B. J., Schmid, S. R., and Jacobson, B. O. (2004). *Fundamentals of fluid film lubrication*. CRC press.

Hartland, S. and Hartley, R. W. (1976). *Axisymmetric fluid-liquid interfaces: Tables giving the shape of sessile and pendant drops and external menisci, with examples of their use*. Elsevier Science Limited.

Janardan, N. and Panchagnula, M. V. (2014). Effect of the initial conditions on the onset of motion in sessile drops on tilted plates. *Colloids and Surfaces A: Physicochemical and Engineering Aspects*, 456:238–245.

Kierzenka, J. and Shampine, L. F. (2001). A bvp solver based on residual control and the maltab pse. *ACM Transactions on Mathematical Software (TOMS)*, 27(3):299–316.

Laplace, P. d. (1806). Théorie de l'action capillaire, supplément à la traité de mécanique céleste 4o.

Macdougall, G. and Ockrent, C. (1942). Surface energy relations in liquid/solid systems: The adhesion of liquids to solids and a new method of determining the surface tension of liquids. *Proceedings of the Royal Society of London. Series A. Mathematical and Physical Sciences*, 180(981):151–173.

Mettu, S. and Chaudhury, M. K. (2008). Motion of drops on a surface induced by thermal gradient and vibration. *Langmuir*, 24(19):10833–10837.

Musterd, M., van Steijn, V., Kleijn, C. R., and Kreutzer, M. T. (2014). Droplets on inclined plates: Local and global hysteresis of pinned capillary surfaces. *Physical Review Letters*, 113(6):066104.

O'Brien, S. B. and van den Brule, B. H. (1991). Shape of a small sessile drop and the determination of contact angle. *Journal of the Chemical Society, Faraday Transactions*, 87(10):1579–1583.

Peters, J. (2001). Total curvature of surfaces (via the divergence of the normal). *International Journal of Mathematical Education in Science and Technology*, 32(6):795–810.

Petrov, J. G., Ralston, J., Schneemilch, M., and Hayes, R. A. (2003). Dynamics of partial wetting and dewetting in well-defined systems. *The Journal of Physical Chemistry B*, 107(7):1634–1645.

Polyanin, A. D. and Manzhirov, A. V. (2006). *Handbook of mathematics for engineers and scientists*. CRC Press.

Prabhala, B. R., Panchagnula, M. V., and Vedantam, S. (2013). Three-dimensional equilibrium shapes of drops on hysteretic surfaces. *Colloid and Polymer Science*, 291:279–289.

Pressley, A. N. (2010). *Elementary differential geometry*. Springer Science & Business Media.

Ravazzoli, P. D., Cuellar, I., González, A. G., and Diez, J. A. (2019). Contact-angle-hysteresis effects on a drop sitting on an incline plane. *Physical Review E*, 99(4):043105.

Ruiz-Cabello, F. M., Rodríguez-Valverde, M., and Cabrerizo-Vilchez, M. (2011). A new method for evaluating the most stable contact angle using tilting plate experiments. *Soft Matter*, 7(21):10457–10461.

Santos, M. and White, J. (2011). Theory and simulation of angular hysteresis on planar surfaces. *Langmuir*, 27(24):14868–14875.

Tanner, L. (1979). The spreading of silicone oil drops on horizontal surfaces. *Journal of Physics D: Applied Physics*, 12(9):1473.

Tenenbaum, M. and Pollard, H. (1985). *Ordinary differential equations: an elementary textbook for students of mathematics, engineering, and the sciences*. Courier Corporation.

Tsai, P.-H., Wang, C., Wang, A.-B., Korobkin, A., Purvis, R., and Khabakhpasheva, T. (2015). Investigation of droplet oscillation on a vibrating elastic plate. In *13th Asian Symposium on Visualization*.

Voinov, O. (1976). Hydrodynamics of wetting. *Fluid Dynamics*, 11(5):714–721.

Wenzel, R. N. (1936). Resistance of solid surfaces to wetting by water. *Industrial and Engineering Chemistry*, 28(8):988–994.

Whitehill, J. D., Neild, A., and Stokes, M. H. (2012). Forced spreading behavior of droplets undergoing low frequency vibration. *Colloids and Surfaces A: Physicochemical and Engineering Aspects*, 393:144–152.

Wijshoff, H. (2018). Drop dynamics in the inkjet printing process. *Current Opinion in Colloid and Interface Science*, 36:20–27.

Ye, Z. and Mizutani, M. (2023). Apparent contact angle of curved and structured surfaces. *Colloids and Surfaces A: Physicochemical and Engineering Aspects*, 677:132337.

Young, T. (1805). Iii. an essay on the cohesion of fluids. *Philosophical transactions of the Royal Society of London*, (95):65–87.

Zabihi, F. and Eslamian, M. (2015). Substrate vibration-assisted spray coating (svasc): Significant improvement in nano-structure, uniformity, and conductivity of pedot: Pss thin films for organic solar cells. *Journal of Coatings Technology and Research*, 12:711–719.